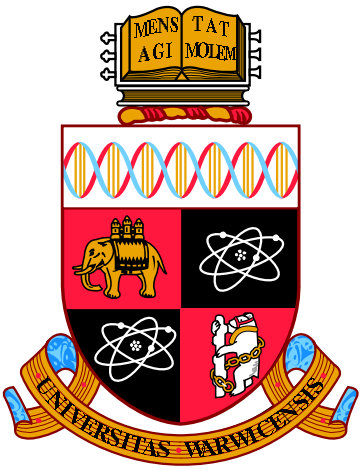

Gaussian quantum metrology for fundamental physics

by

Dominic Branford

Thesis

Submitted to the University of Warwick

for the degree of

Doctor of Philosophy

Department of Physics

November 2019

Contents

List of Figures

List of Tables

Acknowledgements

Firstly, I would like to thank Animesh Datta for his advice and guidance as my supervisor. His incisive questions have helped to refine and give focus to the works in this thesis.

I am grateful to my collaborators Christos Gagatsos and Haixing Miao for their insights and valuable discussions.

At Warwick I have been fortunate to work in the quantum information group with Tillmann Baumgratz, Magda Szczykulska, Christos Gagatsos, George Knee, Theodoros Kapourniotis, Luke Smith, Samuele Ferracin, Jamie Friel, Evangelia Bisketzi, and Francesco Albarelli who have facilitated such a stimulating workplace.

Within the wider department, I would like to thank Sam Brown, Erick Martins Ratamero, and Eduardo Mendive Tapia for welcoming me into the theory group and for their continued friendship, and Rudolf Roemer who has been ever enthusiastic.

Finally, I am indebted to the Oriel physicists: Adam Bozson, Alex Hickey, Nancy Payne, and Amit Visana; and the Sutton Oxonians: Sihong Lin, Jamie MacEwan, and Justin Weeks for their continuing support and appetite for things academic.

Declarations

This thesis is submitted to the University of Warwick in support of my application for the degree of Doctor of Philosophy. It has been composed by myself and has not been submitted in any previous application for any degree.

The work presented (including data generated and data analysis) was carried out by the author.

Parts of this thesis have been published by the author:

- Chapter 4 has been published as Branford et al. [DB4]
- Chapter 5 has been published as Branford et al. [DB3]
- Chapter 6 has been published as Gagatsos et al. [DB1]

List of Publications

[DB1] C. N. Gagatsos, D. Branford, and A. Datta, "Gaussian systems for quantum-enhanced multiple phase estimation", Physical Review A **94**, 042342 (2016).

[DB2] D. Branford, O. C. O. Dahlsten, and A. J. P. Garner, "On defining the Hamiltonian beyond quantum theory", Foundations of Physics **48**, 982–1006 (2018).

[DB3] D. Branford, H. Miao, and A. Datta, "Fundamental quantum limits of multicarrier optomechanical sensors", Physical Review Letters **121**, 110505 (2018).

[DB4] D. Branford, C. N. Gagatsos, J. Grover, A. J. Hickey, and A. Datta, "Quantum enhanced estimation of diffusion", Physical Review A **100**, 022129 (2019).

List of Abbreviations

CRB Cramér-Rao bound

CSL Continuous spontaneous localisation

CV Continuous variable

FI Fisher information

GW Gravitational wave

LO Local oscillator

MI CRB Most-informative Cramér-Rao bound

ML Maximum likelihood

MSE Mean square error

MZI Mach-Zehnder interferometer

PDE Partial differential equation

PNRD Photon number resolving detector

POVM Positive-operator value measure

QCRB Quantum Cramér-Rao bound

QFI Quantum Fisher information

SLD Symmetric logarithmic derivative

SND Spectral noise density

SNL Shot noise limit

SNR Signal-to-noise ratio

Abstract

Optical and optomechanical systems are exploited for quantum technologies to perform highly precise measurements for fundamental physics as well as biological and engineering tasks. Theoretical studies using tools from statistics and quantum information can greatly aid studies of the sensing capabilities of quantum systems and experimental designs. These allow us to quantify the amount of information about a parameter encoded in a quantum state itself and examine how that can be extracted through measurements.

In this thesis we show how mechanical squeezing and measurements beyond position can be utilised to improve the precision of wavepacket expansion measurements which can test collapse models of quantum mechanics. Particularly, that squeezing can compensate for the free-fall time which is often the most significant limiting factor in such experiments, and measurements of other quadratures can offer increased precision.

We demonstrate that the use of additional optical fields to measure the displacement of a free mass in a radiation-pressure limited interferometer cannot surpass the ultimate precision of the single-mode interferometer. This work applies to the likes of laser-interferometric gravitational wave detectors.

Finally, we venture into multi-parameter estimation: we calculate bounds for multi-mode Gaussian states used to estimate many phase shifts and optimise over the input states. In contrast to the—far less experimentally feasible—multi-mode generalisations of N00N states we see no significant improvement when using multi-mode Gaussian states for the task. Given their comparable performance in single-phase estimation this is a new limitation of Gaussian states appearing only at the multi-parameter level.

Chapter 1

Introduction

The search for increasingly precise measurements has led to the inevitable consideration of quantum mechanical systems dating back to the development of atomic clocks [1] which exploit the discrete (quantised) energy levels in atomic states. Optical interferometry similarly originates from utilisation of the wave-like nature of light for precise measurements [2]. These endeavours utilise quantum phenomena of matter and optical systems to achieve such precise measurements.

Quantum metrology is concerned with extracting the highest precision estimates possible of properties of given quantum systems or their environments. Quantum correlations have long been known to enable more precise measurement through squeezing [3] and entanglement [4]. Squeezing has been proposed to improve interferometry including laser-interferometric gravitational wave (GW) detectors [3, 5, 6], as well as dark matter searches [7], and imaging [8, 9].

Different quantum systems can extract different amounts of information from the system being probed. This thesis is concerned with the identification of the metrological power of probe states and measurements: exploring the ability to increase this through preparing the system in different states, and methods of realising such improvements through feasible measurements. Specifically systems which fit into the quantum formalism of Gaussian states and can be used to study fundamental aspects of physics, exploring metrological techniques to study collapse theories, gravitational waves, and imaging.

We demonstrate how metrological techniques introduced in Chapter 2 can be applied to Gaussian systems which are introduced in Chapter 3 and how these can be applied to a range of fundamental problems. Chapter 4 explores the measurement of diffusion in mechanical systems, which can be applied to testing collapse theories [10, 11]. Chapter 5 derives the fundamental precision of optomechanical sensors limited by radiation-pressure [12] and extends to multi-carrier systems. Chapter 6 explores the potential to realise advantages

from the simultaneous estimation of multiple phases [13] with Gaussian states.

1.1 Quantum mechanics

A quantum mechanical state is represented by a density matrix ρ which exists in a d-dimensional Hilbert space. The density matrix is a positive-semidefinite Hermitian operator which satisfies $\mathrm{Tr}(\rho) = 1$.

Pure states are the specific family of states satisfying $\mathrm{Tr}(\rho^2) = 1$, these can all be expressed as

$$\rho = |\psi\rangle \langle\psi| , \tag{1.1}$$

where $|\psi\rangle \langle\psi|$ is an idempotent operator. Mixed states can be constructed as a (non-unique) convex mixture of pure states

$$\rho = \sum_j p_j |\psi_j\rangle \langle\psi_j| , \tag{1.2}$$

with $\sum_j p_j = 1$ and $0 \leq p_j \leq 1, \forall j$.

1.1.1 Quantum dynamics

An isolated quantum system with Hamiltonian $\hat{H}$—which is a Hermitian operator—in the state ρ evolves according to the von Neumann equation [14]

$$\frac{\partial \rho}{\partial t} = -\frac{i}{\hbar}[\hat{H}, \rho], \tag{1.3}$$

which describes the density matrix equivalent of the Schrödinger equation. The von Neumann equation then has solution

$$\rho(t) = e^{-i\frac{\hat{H}(t-t')}{\hbar}} \rho(t') e^{i\frac{\hat{H}(t-t')}{\hbar}}, \tag{1.4}$$

where the $e^{-i\frac{\hat{H}(t-t')}{\hbar}}$ term is a unitary operation which preserves all the eigenvalues of the initial state ρ.

More general evolution may be described by the inclusion of a Lindblad master equation [14, 15]

$$\frac{\partial \rho}{\partial t} = -\frac{i}{\hbar}[\hat{H}, \rho] + \sum_j \gamma_j \left(2\hat{A}_j \rho \hat{A}_j - \hat{A}_j^\dagger \hat{A}_j \rho - \rho \hat{A}_j^\dagger \hat{A}_j \right), \tag{1.5}$$

where the Lindblad operators $\hat{A}_j$ determine the nature of the non-unitary evolution and γ_j the strength of each contribution. This includes dynamics such as decoherence and relaxation processes. Such evolution can then be solved through

Eq. (1.5) or mapped to a Kraus decomposition [14].

Further generalisations can be constructed such as non-Markovian dynamics [16], however the Lindblad form given in Eq. (1.5) is sufficient for the problems considered in this thesis.

1.1.2 Quantum measurements

A general quantum measurement is described by a positive-operator value measure (POVM) consisting of elements $\{\Pi_j\}$ satisfying $\sum_j \Pi_j = \mathbb{1}$ [14]. The probability of finding the outcome j from the state ρ is then

$$\mathrm{P}(j|\rho) = \mathrm{Tr}\left(\rho\Pi_j\right). \tag{1.6}$$

One particular type of POVM is a projective measurement where $\Pi_j = |\psi_j\rangle\langle\psi_j|$, and is formed from of an orthonormal basis where $\langle\psi_j|\psi_k\rangle = \delta_{jk}$ with δ_{jk} being the Kronecker delta. Closely related to measurements are observables, which are Hermitian operators, that ascribe a real value to each eigenvector of the operator.

1.2 Mathematical preliminaries

1.2.1 Woodbury matrix identity

The Woodbury matrix identity [17] allows the inverse of a finite-rank correction to a matrix to be calculated through a finite-rank correction to the inverse. In particular this allows calculation of the inverse of arbitrary-dimensional matrices which can be expressed as a finite-rank correction to a diagonal matrix. Such a case allows for exact calculations for an arbitrary number of modes in Chapters 5 and 6.

When a rank-n matrix can be decomposed as $A + B$ where A has a known inverse and B is a rank-m operator, the inverse $(A + B)^{-1}$ can be found by evaluating only rank-m inverses. One case is where A is diagonal—and so trivially invertible—and accompanied by a low-rank inverse such as a rank-1 projector. In this case the full form $A + B$ does not have an obvious inverse, but by recognising the decomposition can be inverted using a rank-1 inverse alongisde the known inverse of A.

An $n\times n$ rank-m matrix B can be decomposed as

$$B = UCV, \tag{1.7}$$

where C is an $m\times m$ matrix containing the rank-m correction, and U and V are

$n \times m$ and $m \times n$ matrices.

The inverse of $A + UCV$—a rank m correction to a rank n matrix—can then be written as

$$(A + UCV)^{-1} = A^{-1} - A^{-1}U\left(C^{-1} + VA^{-1}U\right)^{-1}VA^{-1}. \tag{1.8}$$

The Sherman-Morrison identity is then the special case where C is a scalar (1×1 matrix) and so $UCV = \boldsymbol{u}\boldsymbol{v}^T$

$$\left(A + \boldsymbol{u}\boldsymbol{v}^T\right)^{-1} = A^{-1} - \frac{1}{1 + \boldsymbol{v}^T A^{-1}\boldsymbol{u}} A^{-1}\boldsymbol{u}\boldsymbol{v}^T A^{-1}, \tag{1.9}$$

where $\boldsymbol{u}$ denotes a vector and $\boldsymbol{u}^T$ its transpose.

Chapter 2

Metrology

The need to identify unknown quantities spans many scientific endeavours. Unknown parameters of interest are not directly accessible but instead must be estimated through sampling from a distribution. Tools from statistical inference, originating with Fisher [18], can be used to bound the uncertainty of an estimator. These utilise the known form of the probability distributions which are sampled from to give a bound on the precision of any estimator.

In physics, metrological undertakings range from practical efforts in frequency estimation [4, 19], magnetic field estimation [20], to displacement estimation [21, 22], and the push for increasingly precise values for fundamental constants [23].

In quantum mechanics the states themselves cannot be directly accessed but only reconstructed through multiple measurements on many copies of the same state by way of quantum tomography [24]. Instead probability distributions are reached by the action of measurements on quantum states. To derive better schemes for parameter estimation it is necessary to explore the results of using both different quantum states and measurements.

Bounds on probability distributions can be extended to lower bound the variance of an estimate of a parameter encoded in a quantum state itself [25, 26] with bounds which holds true for all measurements. Their measurement-independent nature makes these bounds fundamental, bounding the best precision possible without changing the quantum state itself. However this comes at the cost of a looseness as no measurement necessarily attains these fundamental bounds. For single-parameter estimation the quantum Cramér-Rao bound (QCRB) of Helstrom [27] is a sufficient fundamental bound for which an appropriate measurement can always be found to reach it [28]. Quantum mechanics prohibits a simple extension of this to multi-parameter as a result of the non-commutativity of observables: the optimal observable for one parameter may erase information about other parameters from the system. Instead tighter—if more onerous to

calculate—bounds can be constructed with only partially known—and experimentally more demanding—attainability conditions discussed in Section 2.5.2.

Quantum mechanics provides opportunities to exploit quantum phenomena in the form of entanglement and squeezing to attain an increased sensitivity [29, 30]. Classically an experiment can be limited to the shot noise limit (SNL) which results from the discrete nature of probes of repetitions of the experiment; in terms of particle number N the SNL scales in variance as $1/N$. By preparing quantum-mechanically correlated probe states one can realise a precision known as the Heisenberg scaling going beyond the SNL where the Heisenberg scaling is a variance scaling as $1/N^2$ for N entangled particles as opposed to the $1/N$ SNL.

2.1 Statistics

The mean of a probability distribution $P(\boldsymbol{x})$—which describes the probability of finding the outcome vector $\boldsymbol{x}$—is given by

$$\boldsymbol{\mu} = \int \mathrm{d}\boldsymbol{x}\, P(\boldsymbol{x})\boldsymbol{x}, \tag{2.1}$$

and its covariances are

$$\mathrm{Cov}(x_j, x_k) = 2\left[\int \mathrm{d}\boldsymbol{x}\, P(\boldsymbol{x})x_j x_k - \left(\int \mathrm{d}\boldsymbol{x}\, P(\boldsymbol{x})x_j\right)\left(\int \mathrm{d}\boldsymbol{x}\, P(\boldsymbol{x})x_k\right)\right], \tag{2.2}$$

where the factor of two in this definition differs from the typical definition used. These covariances form a covariance matrix

$$\mathrm{Cov}(\boldsymbol{x}) = 2\left[\int \mathrm{d}\boldsymbol{x}\, P(\boldsymbol{x})\boldsymbol{x}\boldsymbol{x}^T - \left(\int \mathrm{d}\boldsymbol{x}\, P(\boldsymbol{x})\boldsymbol{x}\right)\left(\int \mathrm{d}\boldsymbol{x}\, P(\boldsymbol{x})\boldsymbol{x}^T\right)\right], \tag{2.3}$$

for a set of variables. This definition for the covariance matrix—while unconventional in statistics—gives us that the covariance matrix σ of a pure Gaussian quantum state has $\det\sigma = 1$.

2.1.1 Gaussian distribution

The d-dimensional Gaussian or normal distribution $\mathcal{N}(\boldsymbol{\mu}, \Sigma)$—which is solely determined by its mean $\boldsymbol{\mu}$ and covariance matrix Σ—is given by the probability distribution

$$P(\boldsymbol{x}|\boldsymbol{\mu}, \Sigma) = \frac{1}{\sqrt{\pi^d \det\Sigma}} \exp\left[-(\boldsymbol{x}-\boldsymbol{\mu})^T\Sigma^{-1}(\boldsymbol{x}-\boldsymbol{\mu})\right]. \tag{2.4}$$

It features in a range of statistical situations, most notably as the target of the central limit theorem [31, 32].

2.2 Estimators

Estimation is required to infer the true value of some unknown quantity. In general we can consider that some system has a set of outcomes $\{\boldsymbol{x}_j\}$ whose probability distribution is partially known in that it is considered fixed up to a finite set of unknown parameters $\{\phi_j\}$. These outcomes are taken to be the result of sampling from some random variable $X \sim \mathrm{P}(\boldsymbol{x}|\boldsymbol{\phi})$. A simple case would be that the system is known to follow a fixed distribution such as a binomial or Poissonian distribution but with unknown mean $\boldsymbol{\mu}$. From these samples $\{\boldsymbol{x}_i\}$ an estimator $\widetilde{\boldsymbol{\mu}}(\{\boldsymbol{x}_j\})$ can be constructed.

The performance of the estimator $\widetilde{\boldsymbol{\phi}}$ of the parameters $\boldsymbol{\phi}$ can be quantified by the application of a cost function such as the mean square error (MSE)

$$\mathrm{MSE}(\widetilde{\boldsymbol{\phi}}) = \mathrm{Tr}\left(\mathbb{E}\left[(\boldsymbol{\phi} - \widetilde{\boldsymbol{\phi}})(\boldsymbol{\phi} - \widetilde{\boldsymbol{\phi}})^T\right]\right), \tag{2.5}$$

where $\mathbb{E}$ denotes the expectation over $\mathrm{P}(\boldsymbol{x}|\boldsymbol{\phi})$, and whose closeness to zero quantifies how good the estimate is. The bias of an estimator is

$$b(\widetilde{\boldsymbol{\phi}}) = \mathbb{E}(\widetilde{\boldsymbol{\phi}}) - \boldsymbol{\phi}, \tag{2.6}$$

which quantifies the expected deviation from the true parameter value. An unbiased estimator is one which satisfies $\mathbb{E}(\widetilde{\boldsymbol{\phi}}) = \boldsymbol{\phi}$ (i.e. $b(\widetilde{\boldsymbol{\phi}}) = 0$) and can therefore be relied upon to approach the true parameter value. In general biased estimators are used, including in Bayesian analyses or through estimators, including the maximum likelihood (ML) estimator, which are only asymptotically unbiased. The ability to eventually end up at the true value—which an unbiased estimator guarantees—is desirable, however the rate at which a series of estimators converge to the true value is also significant.

The MSE of an estimator can be decomposed as

$$\mathrm{MSE}(\widetilde{\boldsymbol{\phi}}) = \mathrm{Tr}\left(\mathrm{Cov}(\widetilde{\boldsymbol{\phi}}) + b(\widetilde{\boldsymbol{\phi}})b(\widetilde{\boldsymbol{\phi}})^T\right), \tag{2.7}$$

where we see the covariance of the estimator and its bias both contributing to the error. While an unbiased estimator removes the second term, it is possible that a biased estimator possesses a smaller variance and sufficiently small bias so as to yield a lower MSE.

2.3 Classical bounds

The variance of an unbiased estimator $\widetilde{\boldsymbol{\phi}}$ which uses samples from a probability distribution $\mathrm{P}(\boldsymbol{x}|\boldsymbol{\phi})$ can be lower bounded through the Cramér-Rao bound [31–33]

$$\mathrm{Cov}(\widetilde{\boldsymbol{\phi}}) \geq \frac{1}{m} F(\boldsymbol{\phi})^{-1}, \tag{2.8}$$

where m is the number of independent repetitions and $F(\boldsymbol{\phi})$ is the Fisher information (FI) matrix defined by[1]

$$F(\boldsymbol{\phi})_{jk} = \int \mathrm{d}\boldsymbol{x}\, \mathrm{P}(\boldsymbol{x}|\boldsymbol{\phi}) \frac{\partial \ln \mathrm{P}(\boldsymbol{x}|\boldsymbol{\phi})}{\partial \phi_j} \frac{\partial \ln \mathrm{P}(\boldsymbol{x}|\boldsymbol{\phi})}{\partial \phi_k}. \tag{2.9}$$

For sufficiently regular distributions[2] Eq. (2.9) is equivalent to

$$F(\boldsymbol{\phi})_{jk} = -\int \mathrm{d}\boldsymbol{x}\, \mathrm{P}(\boldsymbol{x}|\boldsymbol{\phi}) \frac{\partial^2}{\partial \phi_j \partial \phi_k} \ln \mathrm{P}(\boldsymbol{x}|\boldsymbol{\phi}). \tag{2.10}$$

The CRB can be extended to bound biased estimators where the lower bound is additionally a function of the bias of the estimator [31, 32] however this requires an explicit knowledge of the estimator's bias.

2.3.1 Parameter estimation in Gaussian probability distributions

The Gaussian distribution introduced in Section 2.1.1 is a specific family of probability distributions determined by only their mean $\boldsymbol{\mu}$ and covariances Σ. As such the FI for a parameter encoded in a Gaussian probability distribution can be evaluated directly as a function of the first and second moments.

This FI for a Gaussian probability distribution can then be calculated with Eq. (2.10) relying on the identities [33]

$$\frac{\partial}{\partial \phi_j} \ln \det \Sigma(\boldsymbol{\phi}) = \mathrm{Tr}\left(\Sigma^{-1} \frac{\partial \Sigma}{\partial \phi_j} \right), \tag{2.11}$$

$$\frac{\partial}{\partial \phi_j} \Sigma(\boldsymbol{\phi})^{-1} = -\Sigma^{-1} \frac{\partial \Sigma}{\partial \phi_j} \Sigma^{-1}, \tag{2.12}$$

with which we have

$$\frac{\partial^2}{\partial \phi_j \partial \phi_k} \ln \mathrm{P}(\boldsymbol{x}|\boldsymbol{\mu}_{\boldsymbol{\phi}}, \Sigma_{\boldsymbol{\phi}}) = -\frac{1}{2} \frac{\partial^2}{\partial \phi_j \partial \phi_k} \det \Sigma - \frac{\partial^2}{\partial \phi_j \partial \phi_k} (\boldsymbol{x} - \boldsymbol{\mu})^T \Sigma^{-1} (\boldsymbol{x} - \boldsymbol{\mu}), \tag{2.13}$$

[1] The FI is often given in an equivalent form with the derivative of the logarithm evaluated.

[2] Namely distributions satisfying $\int \mathrm{d}\boldsymbol{x} \frac{\partial^2}{\partial \phi_j \partial \phi_k} \mathrm{P}(\boldsymbol{x}|\boldsymbol{\phi}) = 0$.

where the first term is given directly by Eq. (2.11) followed by the second derivative, while the second requires a longer expansion. With Eq. (2.11) the first term becomes

$$\frac{\partial^2}{\partial\phi_j\partial\phi_k}\det\Sigma = -\operatorname{Tr}\left(\Sigma^{-1}\frac{\partial\Sigma}{\partial\phi_j}\Sigma^{-1}\frac{\partial\Sigma}{\partial\phi_k}\right) + \operatorname{Tr}\left(\Sigma^{-1}\frac{\partial^2\Sigma}{\partial\phi_j\partial\phi_k}\right), \tag{2.14}$$

where we make use of the symmetry of Σ, and the second term becomes

$$\begin{aligned}
&\frac{\partial^2}{\partial\phi_j\partial\phi_k}(\boldsymbol{x}-\boldsymbol{\mu})^T\Sigma^{-1}(\boldsymbol{x}-\boldsymbol{\mu}) \\
&\quad= \frac{\partial}{\partial\phi_k}\left[-2\left(\frac{\partial\boldsymbol{\mu}}{\partial\phi_j}\right)^T\Sigma^{-1}(\boldsymbol{x}-\boldsymbol{\mu}) - (\boldsymbol{x}-\boldsymbol{\mu})^T\Sigma^{-1}\frac{\partial\Sigma}{\partial\phi_j}\Sigma^{-1}(\boldsymbol{x}-\boldsymbol{\mu})\right] \\
&\quad= -2\left(\frac{\partial^2\boldsymbol{\mu}}{\partial\phi_j\partial\phi_k}\right)^T\Sigma^{-1}(\boldsymbol{x}-\boldsymbol{\mu}) + 2\left(\frac{\partial\boldsymbol{\mu}}{\partial\phi_j}\right)^T\Sigma^{-1}\frac{\partial\Sigma}{\partial\phi_k}\Sigma^{-1}(\boldsymbol{x}-\boldsymbol{\mu}) \\
&\qquad+ 2\left(\frac{\partial\boldsymbol{\mu}}{\partial\phi_j}\right)^T\Sigma^{-1}\frac{\partial\boldsymbol{\mu}}{\partial\phi_k} + 2\left(\frac{\partial\boldsymbol{\mu}}{\partial\phi_k}\right)^T\Sigma^{-1}\frac{\partial\Sigma}{\partial\phi_j}\Sigma^{-1}(\boldsymbol{x}-\boldsymbol{\mu}) \\
&\qquad+ 2(\boldsymbol{x}-\boldsymbol{\mu})^T\Sigma^{-1}\frac{\partial\Sigma}{\partial\phi_k}\Sigma^{-1}\frac{\partial\Sigma}{\partial\phi_j}\Sigma^{-1}(\boldsymbol{x}-\boldsymbol{\mu}) \\
&\qquad- (\boldsymbol{x}-\boldsymbol{\mu})^T\Sigma^{-1}\frac{\partial^2\Sigma}{\partial\phi_j\partial\phi_k}\Sigma^{-1}(\boldsymbol{x}-\boldsymbol{\mu}),
\end{aligned} \tag{2.15}$$

where again we make use of the symmetry of Σ. The integrand can then be divided into powers of $\boldsymbol{x}$ and integrated with

$$\begin{aligned}
\int \mathrm{d}\boldsymbol{x}\, \mathrm{P}(\boldsymbol{x}|\boldsymbol{\mu_\phi},\Sigma_{\boldsymbol{\phi}}) &= 1, \\
\int \mathrm{d}\boldsymbol{x}\ (x_j-\mu_j)\,\mathrm{P}(\boldsymbol{x}|\boldsymbol{\mu_\phi},\Sigma_{\boldsymbol{\phi}}) &= 0, \\
\int \mathrm{d}\boldsymbol{x}\ (x_j-\mu_j)\,(x_k-\mu_k)\,\mathrm{P}(\boldsymbol{x}|\boldsymbol{\mu_\phi},\Sigma_{\boldsymbol{\phi}}) &= \frac{1}{2}\Sigma_{jk},
\end{aligned} \tag{2.16}$$

which yield

$$\begin{aligned}
-\int \mathrm{d}\boldsymbol{x}\ \frac{\partial^2}{\partial\phi_j\partial\phi_k}\left(-\frac{1}{2}\det\Sigma\right) &= -\frac{1}{2}\operatorname{Tr}\left(\Sigma^{-1}\frac{\partial\Sigma}{\partial\phi_j}\Sigma^{-1}\frac{\partial\Sigma}{\partial\phi_k}\right) \\
&\quad+ \operatorname{Tr}\left(\Sigma^{-1}\frac{\partial^2\Sigma}{\partial\phi_j\partial\phi_k}\right), \\
-\int \mathrm{d}\boldsymbol{x}\ \frac{\partial^2}{\partial\phi_j\partial\phi_k}\left[-(\boldsymbol{x}-\boldsymbol{\mu})^T\Sigma^{-1}(\boldsymbol{x}-\boldsymbol{\mu})\right] &= 2\left(\frac{\partial\boldsymbol{\mu}}{\partial\phi_j}\right)^T\Sigma^{-1}\frac{\partial\boldsymbol{\mu}}{\partial\phi_k} \\
&\quad+ \operatorname{Tr}\left(\Sigma^{-1}\frac{\partial\Sigma}{\partial\phi_k}\Sigma^{-1}\frac{\partial\Sigma}{\partial\phi_j}\right) \\
&\quad- \frac{1}{2}\operatorname{Tr}\left(\Sigma^{-1}\frac{\partial^2\Sigma}{\partial\phi_j\partial\phi_k}\right).
\end{aligned} \tag{2.17}$$

Combining Eqs. (2.10), (2.13) and (2.17) we find the FI for parameters which parameterise a Gaussian probability distribution to be [33, 34]

$$F(\boldsymbol{\phi})_{jk} = 2\left(\frac{\partial \boldsymbol{\mu}}{\partial \phi_j}\right)^T \Sigma^{-1} \frac{\partial \boldsymbol{\mu}}{\partial \phi_k} + \frac{1}{2}\,\mathrm{Tr}\left(\Sigma^{-1}\frac{\partial \Sigma}{\partial \phi_j}\Sigma^{-1}\frac{\partial \Sigma}{\partial \phi_k}\right). \tag{2.18}$$

2.3.2 Attainability of the classical bound

An efficient estimator is one whose variance approaches that of the CRB. In general the ML estimator [31–33] is asymptotically both unbiased and efficient [32, 33] and therefore approaches the CRB for a sufficiently large number of repetitions.

Estimation of the mean of the distribution is a special case for which an efficient estimator exists outside of the asymptotic limit. For $\boldsymbol{X}_j \sim \mathcal{N}(\boldsymbol{\mu}, \Sigma)$ The estimator of $\boldsymbol{\mu}$, $\widetilde{\boldsymbol{\mu}} = \frac{1}{m}\sum_{j=1}^{m} X_j$, is straightforwardly unbiased. Moreover we can calculate the covariance of the estimator $\widetilde{\boldsymbol{\mu}}$ with Eq. (2.16) to be

$$\mathrm{MSE}(\widetilde{\boldsymbol{\mu}}) = \frac{1}{m}\,\mathrm{Tr}\left(\frac{1}{2}\Sigma\right), \tag{2.19}$$

which is the inverse of Eq. (2.18) when $\phi_j = \mu_j$ (multiplied by $1/m$ for the number of repetitions), demonstrating the single-shot efficiency of $\widetilde{\boldsymbol{\mu}}$.

2.4 Quantum bounds

For a quantum-mechanical system the probability distributions are derived from the action of a measurement, described by a POVM, on a quantum state $\rho_{\boldsymbol{\phi}}$. The FI for such a problem can then be described as

$$F(\rho_{\boldsymbol{\phi}}, \boldsymbol{\Pi})_{jk} = \int \mathrm{d}\boldsymbol{x}\, \frac{1}{\mathrm{P}(\boldsymbol{x}|\rho_{\boldsymbol{\phi}}, \boldsymbol{\Pi})} \frac{\partial \mathrm{P}(\boldsymbol{x}|\rho_{\boldsymbol{\phi}}, \boldsymbol{\Pi})}{\partial \phi_j} \frac{\partial \mathrm{P}(\boldsymbol{x}|\rho_{\boldsymbol{\phi}}, \boldsymbol{\Pi})}{\partial \phi_k}, \tag{2.20}$$

where the probability is $\mathrm{P}(\boldsymbol{x}|\rho_{\boldsymbol{\phi}}, \boldsymbol{\Pi}) = \mathrm{Tr}(\rho_{\boldsymbol{\phi}}\Pi_{\boldsymbol{x}})$.

With quantum mechanics, calculating and optimising Eq. (2.20) over the initial state ρ_0 and the measurement $\boldsymbol{\Pi}$ are the typically desired tasks. The traditional route has looked to POVM-independent lower bounds which are given only as a function of $\rho_{\boldsymbol{\phi}}$ [25, 26] to give a fundamental limit. The attainability through the existence of an appropriate POVM can then be explored retrospectively.

In general the multi-parameter CRB does not afford straightforward comparison between different settings through the matrix inequality. To reduce the problem to a scalar cost-function we introduce a positive matrix G which

quantifies the relative importance of the parameters and evaluate the quantity

$$C(\rho_{\boldsymbol{\phi}}; G) = \mathrm{Tr}\left(G\,\mathrm{Cov}(\widetilde{\boldsymbol{\phi}})\right). \tag{2.21}$$

A number of CRBs can be defined for the parameters $\{\phi_j\}$ encoded in the quantum states $\rho_{\boldsymbol{\phi}}$ which lower bound the quantity $C(\rho_{\boldsymbol{\phi}}; G)$.

2.4.1 Quantum Cramér-Rao bound

In place of the derivative of the probability distributions in the FI, the symmetric logarithmic derivative (SLD) operators defined by

$$\frac{\partial \rho}{\partial \phi_j} = \frac{\mathcal{L}_j \rho + \rho \mathcal{L}_j}{2}, \tag{2.22}$$

can be used to construct a quantum Fisher information (QFI) matrix, namely an upper bound on the FI matrix which depends only on the state. For parameters $\{\phi_j\}$ encoded in a state $\rho_{\boldsymbol{\phi}}$ this QFI is

$$H(\rho_{\boldsymbol{\phi}})_{jk} = \mathrm{Tr}\left(\rho \frac{\mathcal{L}_j \mathcal{L}_k + \mathcal{L}_k \mathcal{L}_j}{2}\right), \tag{2.23}$$

which can be compared to Eq. (2.9) with the density matrix taking the place of the probability distribution and the SLDs replacing the derivatives of the likelihood. Combining Eq. (2.22) with the cyclicity of the trace it has an alternative expression

$$H(\rho_{\boldsymbol{\phi}})_{jk} = \mathrm{Tr}\left(\partial_{\phi_k} \rho \mathcal{L}_j\right). \tag{2.24}$$

The QFI is derived for the specific family of Gaussian states in Section 3.4.

The SLD in the QFI takes the place of the derivative of the probability distribution in the FI. Thus, loosely-speaking, the more rapidly changing states yield a larger SLD and so a larger QFI which corresponds to a better lower bound.

The SLD QCRB (henceforth the QCRB) provides a lower bound on the variance of an unbiased estimator for a set of parameters $\{\phi_j\}$ encoded in a quantum state $\rho_{\boldsymbol{\phi}}$ as [29, 35, 36]

$$\mathrm{Cov}(\widetilde{\boldsymbol{\phi}}) \geq \frac{1}{m} H(\rho_{\boldsymbol{\phi}})^{-1}, \tag{2.25}$$

where $H(\rho_{\boldsymbol{\phi}})$ is the QFI matrix. The SLD operator is not uniquely defined outside the span of the state $\rho_{\boldsymbol{\phi}}$, the remainder does not affect the QFI itself but has implications to the attainability of the multi-parameter QCRB which we highlight in Section 2.5.

The QFI can also be recognised as the second derivative of the fidelity or Bures distance [29, 35]

$$H(\rho_{\boldsymbol{\phi}}) = -4 \lim_{\mathrm{d}\boldsymbol{\phi}\to 0} \left\{ \frac{\partial^2}{\partial(\mathrm{d}\phi_j)\partial(\mathrm{d}\phi_k)} \mathcal{F}(\rho_{\boldsymbol{\phi}}, \rho_{\boldsymbol{\phi}+\mathrm{d}\boldsymbol{\phi}}) \right\}, \tag{2.26}$$

where the fidelity is $\mathcal{F}(\rho_1, \rho_2) = \mathrm{Tr}(\sqrt{\sqrt{\rho_1}\rho_2\sqrt{\rho_1}})$. Similarly, a loose intuition exists here in that the smaller the fidelity between states with neighbouring parameter values is, when the parameter is changed by a small amount, the state may be able to yield a better estimate of the parameter due to a more pronounced effect of the parameter on the state.

While the general solution to the SLD equation can require some effort to solve for pure states a straightforward expression is revealed as $\partial_{\phi_j} |\psi_{\boldsymbol{\phi}}\rangle \langle\psi_{\boldsymbol{\phi}}| = (\partial_{\phi_j} |\psi_{\boldsymbol{\phi}}\rangle) \langle\psi_{\boldsymbol{\phi}}| + |\psi_{\boldsymbol{\phi}}\rangle (\partial_{\phi_j} \langle\psi_{\boldsymbol{\phi}}|)$. Hence we recognise

$$\mathcal{L}_j = 2\frac{\partial}{\partial\phi_j} |\psi_{\boldsymbol{\phi}}\rangle \langle\psi_{\boldsymbol{\phi}}|, \tag{2.27}$$

and so the QFI is

$$H(|\psi_{\boldsymbol{\phi}}\rangle \langle\psi_{\boldsymbol{\phi}}|) = 4\Re\left[\langle\partial_j\psi|\partial_k\psi\rangle + \langle\psi|\partial_j\psi\rangle \langle\psi|\partial_k\psi\rangle\right], \tag{2.28}$$

where $\Re$ denotes the real part. It can easily be seen that Eq. (2.28) is identical for $|\psi_{\boldsymbol{\phi}}\rangle$ and $U|\psi_{\boldsymbol{\phi}}\rangle$ for $\partial_{\phi_j} U = 0$.

In general the parameters of interest are not fixed and it can—as we shall do in Chapter 6—be advantageous to both transform between parameter sets (e.g. from $\{\phi_1, \phi_2\}$ to $\{\phi_1+\phi_2, \phi_1-\phi_2\}$) and even to reduce the number of parameters. This can be done through identifying that for the parameters $\{\varphi_j(\boldsymbol{\phi})\}$ the QFI matrix $H(\rho_{\boldsymbol{\varphi}})$ can be found as [35]

$$H(\rho_{\boldsymbol{\varphi}}) = BH(\rho_{\boldsymbol{\phi}})B^T, \tag{2.29}$$

where

$$B_{jk} = \frac{\partial\phi_k}{\partial\varphi_j}, \tag{2.30}$$

where the B need not be a square matrix (in general the QFI matrix for a reduced set of parameters is simply the elements of the QFI matrix associated with those parameters). The same transformation between parameter sets holds for the FI of the CRB [33].

In its scalar form the QCRB is

$$C(\rho_{\boldsymbol{\phi}}; G) \geq \frac{1}{m} C^{\mathrm{S}}(\rho_{\boldsymbol{\phi}}; G), \tag{2.31}$$

where $C^{\mathrm{S}}(\rho_{\boldsymbol{\phi}}; G) = \mathrm{Tr}\left(GH^{-1}\right)$.

2.4.2 Holevo Cramér-Rao bound

The Holevo CRB is a tighter lower bound than the QCRB [26, 37–40], although they are identical in certain regimes including single-parameter estimation [39].

Unlike the QCRB the Holevo CRB exists only in the form of a scalar inequality and is not defined by an SLD-like quantity but as a minimisation over a set of operators as [38, 39]

$$C^{\mathrm{H}}(\rho_{\boldsymbol{\phi}}; G) = \min_{\{X_j\}} \left\{ \mathrm{Tr}\left(G\Re V + \|\sqrt{G}\Im V \sqrt{G}\| \right) \right\}, \tag{2.32}$$

where $\Re$ and $\Im$ denote the real and imaginary parts, V is $V_{jk} = \mathrm{Tr}\left(X_j X_k \rho_{\boldsymbol{\phi}}\right)$, and $\{X_j\}$ are Hermitian operators satisfying $\mathrm{Tr}\left(\{X_j, \mathcal{L}_k\}\rho_{\boldsymbol{\phi}}\right) = \delta_{jk}$ where $\{A, B\}$ is the anti-commutator $\{A, B\} = AB + BA$.

2.4.3 Most-informative Cramér-Rao bound

The most-informative CRB (MI CRB) provides the tightest possible bound attainable from a single copy of the state $\rho_{\boldsymbol{\phi}}$ [38]. This is written explicitly for a single-parameter as

$$C^{\mathrm{MI}}(\rho_{\boldsymbol{\phi}}; G) = \min_{\boldsymbol{\Pi}} \mathrm{Tr}\left(GF(\rho_{\boldsymbol{\phi}}, \boldsymbol{\Pi})^{-1}\right), \tag{2.33}$$

with the FI F being defined as in Eq. (2.20).

By definition the MI CRB is the best precision available from measurements on a single copy alone [28, 35]. Unlike the QCRB or Holevo CRB the MI CRB is not distributive over $\rho^{\otimes n}$. This means that with collective measurements it may be possible to obtain a better precision than the multiple uses of the single-copy MI CRB using multiple copies of the same state [39, 41–43].

2.5 Attainability of the quantum bounds

2.5.1 Single-parameter bounds

For single-parameter estimation problems there is a guaranteed POVM which can be used to attain the QCRB. Through the application of a measurement consisting of projectors onto the eigenstates of the SLD one can establish [28, 35]

$$H(\rho_\phi) = F(\rho_\phi, \boldsymbol{\Pi}_{\mathrm{SLD}}), \tag{2.34}$$

where $\mathbf{\Pi}_{\mathrm{SLD}}$ is the set of projectors onto the eigenbasis of the SLD[3]. As the QCRB is always a valid upper bound on the CRB it can therefore be written explicitly as the MI CRB [28, 29, 35] or

$$H(\rho_\phi) = \max_{\mathbf{\Pi}} F(\rho_\phi, \mathbf{\Pi}). \tag{2.35}$$

While the POVM identified in this method is not necessarily uniquely able to saturate the QCRB it is constructive in the nature that an exact POVM can be constructed from the SLD. The dependence of a parameter estimation scheme on that parameter is generally undesirable—as the scheme cannot be perfectly applied to a parameter which is only approximately known—however the QCRB can still be saturated in this manner through an adaptive strategy which updates the POVM [38, 44, 45].

2.5.2 Multi-parameter bounds

The multi-parameter QCRB does not afford the same attainability. In the simple case where all SLDs $\{\mathcal{L}_j\}$ commute the SLDs share a common eigenbasis and so projection onto the eigenstates of this common eigenbasis is sufficient.

A weaker condition

$$\mathrm{Tr}\left(\rho[\mathcal{L}_j, \mathcal{L}_k]\right) = 0, \forall j, k \tag{2.36}$$

can be identified which guarantees the QCRB to be equated to the Holevo CRB [37, 39] as $C^{\mathrm{S}}(\rho_{\boldsymbol{\phi}}; G) = C^{\mathrm{H}}(\rho_{\boldsymbol{\phi}}; G)$.

The Holevo CRB in turn can be identified as attainable for multiple parameters with the use of collective measurements which act on $\rho^{\otimes M}$ for a sufficiently large M [46–48]. In this case we are guaranteed that [37, 40]

$$C^{\mathrm{H}}(\rho_{\boldsymbol{\phi}}; G) = \lim_{M\to\infty} \left\{ M C^{\mathrm{MI}}\left(\rho_{\boldsymbol{\phi}}^{\otimes M}; G\right)\right\}, \tag{2.37}$$

and so collective measurements can be used to attain a better precision per copy.

For pure states the condition Eq. (2.36) is a stronger condition on the attainability of the QCRB [49]. The Holevo CRB can then be satisfied without the need for collective measurements [37, 49, 50]. Whence we see that Eq. (2.36) is sufficient to guarantee attainability of the QCRB without the need for collective measurements.

[3]The feasibility of performing such a measurement is variable. In Chapter 4 we identify certain regimes where this requires only phonon counting while in others a prohibitive amount of squeezing is required. In Chapter 5 we show that for displacement estimation this is simply homodyne detection.

2.6 Notation of this thesis

For the remainder of the thesis the FIs shall be denoted solely as functions of the parameter(s) which concern them or their argument omitted entirely, the probability or density matrix from which they come shall be omitted or indicated as subscript where necessary. The variance of an estimate of a single parameter ϕ will be denoted as $(\Delta\phi)^2$ and the multi-parameter lower bounds of Chapter 6 given as $\mathrm{Tr}\left(F^{-1}\right)$.

Chapter 3

Gaussian systems

Gaussian states are a frequently-used family of states which belong to the class of continuous variable (CV) states. Unlike qubits and qudits which exist within finite-dimensional Hilbert spaces CV systems belong to an infinite-dimensional Hilbert space $\mathcal{H}$. CV models are required to describe systems which have a continuous degree of freedom such as mechanical and optical systems. Even atomic systems can technically be considered as CV due to their infinite energy spectrum although the quadrature operators have a subtler meaning. As the ionisation energy is finite only a finite number can be considered accessible and so a qudit model is appropriate.

Gaussian states are some of the most common CV states due to the experimental practicality of producing them—coherent light being classical and squeezing requiring a somewhat experimentally feasible non-linearity. They also benefit from a simpler framework, relative to the full machinery required for arbitrary CV systems, with a phase space formalism discussed in this Chapter. Theoretically, open-dynamic evolution [51, 52] and calculation of properties such as entropies [53] take much more manageable forms. The QFI can similarly be calculated for Gaussian states more straightforwardly [52, 54–56] than the spectral decomposition generally required [29, 35].

A CV system consists of a number of different modes d which exist in the Hilbert space $\mathcal{H}^{\otimes d}$, each mode represents a different degree of freedom: a particle has three independent spatial dimensions, light can possess different optical frequencies and polarisations, a cavity with an optical field circulating and a mechanical oscillator at one end is a two-mode optomechanical system. Each mode j has annihilation and creation operators $\{\hat{a}_j, \hat{a}_j^\dagger\}$ which map the Fock states as

$$\hat{a}_j^\dagger |n\rangle = \sqrt{n+1}\,|n+1\rangle\,, \quad \hat{a}_j |n\rangle = \sqrt{n}\,|n-1\rangle\,, \tag{3.1}$$

which satisfy the commutation relations

$$[\hat{a}_j, \hat{a}_k] = 0, \quad [\hat{a}_j, \hat{a}_k^\dagger] = \delta_{jk}. \tag{3.2}$$

The (dimensionless) quadrature operators

$$\hat{x}_j = \frac{\hat{a}_j + \hat{a}_j^\dagger}{\sqrt{2}}, \quad \hat{p}_j = \frac{\hat{a}_j - \hat{a}_j^\dagger}{i\sqrt{2}}, \tag{3.3}$$

are Hermitian observables with a continuous spectrum. The quantised electric and magnetic field operators similarly behave as position and momentum operators [52, 57]. The quadrature operators have the non-trivial commutation relations

$$[\hat{x}_j, \hat{p}_k] = i\delta_{jk}, \tag{3.4}$$

where the non-commutativity enforces some minimal uncertainty between the two quadratures. More generally one can define—for each mode—a quadrature

$$\hat{x}_\phi = \hat{x}\cos\phi + \hat{p}\sin\phi, \tag{3.5}$$

which then has the non-trivial commutation relations

$$[\hat{x}_\phi, \hat{x}_{\phi+\pi/2}] = i\delta_{jk}. \tag{3.6}$$

The Fock states are eigenstates of the number operator

$$\hat{n}_j = \hat{a}_j^\dagger \hat{a}_j = \frac{\hat{x}_j^2 + \hat{p}_j^2 - 1}{2}, \tag{3.7}$$

which form the most orthonormal basis to describe CV states in the traditional picture, in particular for approximating CV systems as finite-dimensional states. A phase space picture—analogous to that of classical mechanics—is however more natural to use for many purposes.

These quadrature operators can be written in the more compact form

$$\hat{\boldsymbol{R}} = \begin{pmatrix} \hat{x}_1 & \hat{x}_2 & \cdots & \hat{x}_d & \hat{p}_1 & \hat{p}_2 & \cdots & \hat{p}_d \end{pmatrix}^T, \tag{3.8}$$

with which we define the matrix Ω as

$$[\hat{R}_j, \hat{R}_k] = i\Omega_{jk}, \tag{3.9}$$

such that

$$\Omega = \begin{pmatrix} \mathbb{0}_{d\times d} & \mathbb{1}_{d\times d} \\ -\mathbb{1}_{d\times d} & \mathbb{0}_{d\times d} \end{pmatrix}. \tag{3.10}$$

We can alternatively use the quadrature vector $\hat{\boldsymbol{Q}}$

$$\hat{\boldsymbol{Q}} = \begin{pmatrix} \hat{x}_1 & \hat{p}_1 & \hat{x}_2 & \hat{p}_2 & \cdots & \hat{x}_d & \hat{p}_d \end{pmatrix}^T, \tag{3.11}$$

this representation will occasionally prove more convenient to work with for certain results. In this case the associated commutators are

$$\Omega_{\hat{\boldsymbol{Q}}} = \bigoplus_{j=1}^{d} \Omega_2, \tag{3.12}$$

with $\bigoplus$ denoting the direct sum, and we denote the 2×2 single-mode matrix of commutators as

$$\Omega_2 = \begin{pmatrix} 0 & 1 \\ -1 & 0 \end{pmatrix}, \tag{3.13}$$

which is Eq. (3.10) for $d = 1$. For the $d = 1$ single-mode system the two quadrature vector representations are trivially identical.

3.1 Phase space

A phase space representation of CV states can be constructed, with states being represented by quasiprobability distributions [52, 53, 58]. These quasiprobabilities integrate to 1 but are not strictly positive distributions.

3.1.1 Displacement operator

The displacement operator is defined with complex argument as

$$\hat{D}(\alpha) = \exp\left(\alpha\hat{a}^\dagger - \alpha^*\hat{a}\right), \tag{3.14}$$

which can be equivalently written as

$$\hat{D}(\alpha) = e^{-\alpha^*\hat{a}} e^{\alpha\hat{a}^\dagger} e^{+\frac{1}{2}|\alpha|^2} = e^{\alpha\hat{a}^\dagger} e^{-\alpha^*\hat{a}} e^{-\frac{1}{2}|\alpha|^2}. \tag{3.15}$$

Its action on the mode operators is

$$\begin{aligned} \hat{D}(\alpha)^\dagger \hat{a} \hat{D}(\alpha) &= \hat{a} + \alpha, \quad \hat{D}(\alpha)^\dagger \hat{a}^\dagger \hat{D}(\alpha) = \hat{a}^\dagger - \alpha^*, \\ \hat{D}(\alpha) \hat{a} \hat{D}(\alpha)^\dagger &= \hat{a} - \alpha, \quad \hat{D}(\alpha) \hat{a}^\dagger \hat{D}(\alpha)^\dagger = \hat{a}^\dagger + \alpha^*, \end{aligned} \tag{3.16}$$

which can be rewritten as commutators

$$\begin{aligned} [\hat{D}(\alpha)^\dagger, \hat{a}] &= \alpha \hat{D}(\alpha)^\dagger, \quad [\hat{D}(\alpha)^\dagger, \hat{a}^\dagger] = -\alpha^* \hat{D}(\alpha)^\dagger, \\ [\hat{D}(\alpha), \hat{a}] &= -\alpha \hat{D}(\alpha), \quad [\hat{D}(\alpha), \hat{a}^\dagger] = \alpha^* \hat{D}(\alpha). \end{aligned} \tag{3.17}$$

Derivatives of the displacement operator can be recognised through Eq. (3.15) as

$$\begin{aligned} \frac{\partial}{\partial\alpha}\hat{D}(\alpha) &= \hat{D}(\alpha)\left(\hat{a}^\dagger + \frac{\alpha^*}{2}\right), & \frac{\partial}{\partial\alpha^*}\hat{D}(\alpha) &= -\hat{D}(\alpha)\left(\hat{a} + \frac{\alpha}{2}\right), \\ \frac{\partial}{\partial\alpha}\hat{D}(\alpha)^\dagger &= -\hat{D}(\alpha)^\dagger\left(\hat{a}^\dagger - \frac{\alpha^*}{2}\right), & \frac{\partial}{\partial\alpha^*}\hat{D}(\alpha)^\dagger &= \hat{D}(\alpha)^\dagger\left(\hat{a} - \frac{\alpha}{2}\right). \end{aligned} \tag{3.18}$$

3.1.2 Characteristic function

The s-ordered characteristic functions of a quantum state are [52, 53]

$$\chi_\rho^{(s)}(\boldsymbol{\xi}) = \mathrm{Tr}\left(\hat{D}(\boldsymbol{\xi})\rho\right) e^{\frac{s}{2}|\xi|^2}, \tag{3.19}$$

with $s \in [-1, 1]$, and $\boldsymbol{\xi}$ is a complex vector related to $\boldsymbol{R}$ by $\boldsymbol{\xi} = \frac{1}{\sqrt{2}}\begin{pmatrix}\mathbb{1} & i\mathbb{1}\end{pmatrix}\boldsymbol{R}$; through this equivalence we can also work with $\chi_\rho^{(s)}(\boldsymbol{R})$. The purity constraint $\mathrm{Tr}\,(\rho) = 1$ written in terms of the characteristic function becomes $\chi^{(s)}(0) = 1$ [52, 53]. More generally the trace of an operator $\hat{z}$ is given by [52]

$$\mathrm{Tr}\,(\hat{z}) = \chi_{\hat{z}}^{(s)}(0). \tag{3.20}$$

From these characteristic functions a family of real quasi-probability distributions can be constructed as

$$W_\rho^{(s)}(\boldsymbol{R}) = \frac{1}{(2\pi)^{2n}}\int \mathrm{d}\tilde{\boldsymbol{R}}\, \chi_\rho^{(s)}(\tilde{\boldsymbol{R}}) e^{i\tilde{\boldsymbol{R}}^T\Omega\boldsymbol{R}}. \tag{3.21}$$

The $s \in \{-1, 0, 1\}$ cases are particularly interesting as the Q-function, Wigner function and P-representation respectively.

This thesis will only utilise the Wigner function and Q-function. Henceforth we will use $W_{\hat{z}}(\boldsymbol{R})$ to refer explicitly to the Wigner function ($s = 0$) and $Q_{\hat{z}}(\boldsymbol{R})$ to refer to the Q-function ($s = -1$). In the absence of a subscript the distributions denote a quantum state. Unless otherwise specified the characteristic function χ will be taken to refer to the $s = 0$ characteristic function.

3.1.3 Wigner function

The Wigner function of an operator $\hat{z}$ is given by [52]

$$W_{\hat{z}}(\boldsymbol{x}, \boldsymbol{p}) = \left(\frac{2}{\pi}\right)^d \int \mathrm{d}\boldsymbol{y}\ \langle \boldsymbol{x} + \boldsymbol{y}|\hat{z}|\boldsymbol{x} - \boldsymbol{y}\rangle\, e^{2i\boldsymbol{y}^T\boldsymbol{p}} \tag{3.22}$$

or equivalently by [58]

$$W_{\hat{z}}(\boldsymbol{x},\boldsymbol{p}) = \left(\frac{2}{\pi}\right)^d \mathrm{Tr}\left[\hat{z}\hat{D}\left(\frac{\boldsymbol{x}+i\boldsymbol{y}}{\sqrt{2}}\right)\hat{P}\hat{D}\left(\frac{\boldsymbol{x}+i\boldsymbol{y}}{\sqrt{2}}\right)^\dagger\right], \tag{3.23}$$

where $\hat{P} = e^{i\pi\hat{n}_{\mathrm{Tot}}}$ is the parity operator with $\hat{n}_{\mathrm{Tot}} = \sum_j \hat{n}_j$ being the total excitation number, and $\hat{D}(\alpha)$ is the displacement operator defined in Eq. (3.14).

3.1.4 Q-function

The Q-function is the projection of the state onto the overcomplete basis of coherent states. The Q-function is therefore [52, 53, 58]

$$Q(\boldsymbol{\alpha}) = \frac{1}{\pi^d}\langle\alpha|\rho|\alpha\rangle, \tag{3.24}$$

which is related to the Wigner function through

$$Q_\rho(\boldsymbol{R}) = \frac{1}{(2\pi)^d}\int \mathrm{d}\boldsymbol{R}'\, W_\rho(\boldsymbol{R}')e^{-(\boldsymbol{R}-\boldsymbol{R}')^T(\boldsymbol{R}-\boldsymbol{R}')}, \tag{3.25}$$

which can be derived from Eqs. (3.19) and (3.21) along with the convolution theorem.

3.1.5 Operators and derivatives in phase space

The action of the quadrature operators on the density matrix can be mapped to phase space [52, 54, 57, 59]. Doing so is useful both for open dynamics (see Section 3.3.5) and metrology (see Section 3.4). Taking the symmetric-ordered characteristic function

$$\chi(\boldsymbol{\xi}) = \mathrm{Tr}\left(\hat{D}(\boldsymbol{\xi})\rho\right), \tag{3.26}$$

we note that we have the derivatives

$$\begin{aligned}\frac{\partial}{\partial\xi_j}\chi(\boldsymbol{\xi}) &= \mathrm{Tr}\left(\frac{\partial}{\partial\xi_j}\hat{D}(\boldsymbol{\xi})\rho\right) = \mathrm{Tr}\left(\hat{D}(\boldsymbol{\xi})\left(\hat{a}_j^\dagger + \frac{\xi_j^*}{2}\right)\rho\right),\\ \frac{\partial}{\partial\xi_j^*}\chi(\boldsymbol{\xi}) &= \mathrm{Tr}\left(\frac{\partial}{\partial\xi_j^*}\hat{D}(\boldsymbol{\xi})\rho\right) = -\mathrm{Tr}\left(\hat{D}(\boldsymbol{\xi})\left(\hat{a}_j + \frac{\xi_j}{2}\right)\rho\right),\end{aligned} \tag{3.27}$$

using Eq. (3.18).

From this we identify [57]

$$\begin{aligned}\chi_{\hat{a}_j^\dagger\hat{O}} &= \left(\frac{\partial}{\partial\xi_j} - \frac{\xi_j^*}{2}\right)\chi_{\hat{O}}, \quad \chi_{\hat{a}_j\hat{O}} = \left(-\frac{\partial}{\partial\xi_j^*} - \frac{\xi_j}{2}\right)\chi_{\hat{O}}, \\ \chi_{\hat{O}\hat{a}_j^\dagger} &= \left(\frac{\partial}{\partial\xi_j} + \frac{\xi_j^*}{2}\right)\chi_{\hat{O}}, \quad \chi_{\hat{O}\hat{a}_j} = \left(-\frac{\partial}{\partial\xi_j^*} + \frac{\xi_j}{2}\right)\chi_{\hat{O}},\end{aligned} \tag{3.28}$$

which with Eq. (3.3) and the following identities for the derivatives

$$\frac{\partial}{\partial x_j} = \frac{1}{\sqrt{2}}\left(\frac{\partial}{\partial\alpha_j} + \frac{\partial}{\partial\alpha_j^*}\right), \quad \frac{\partial}{\partial p_j} = \frac{i}{\sqrt{2}}\left(\frac{\partial}{\partial\alpha_j} - \frac{\partial}{\partial\alpha_j^*}\right), \tag{3.29}$$

allow us to rewrite

$$\chi_{\hat{R}_j\hat{O}} = \left(-i\Omega_{jk}\frac{\partial}{\partial R_k} - \frac{R_j}{2}\right)\chi_{\hat{O}}, \quad \chi_{\hat{O}\hat{R}_j} = \left(-i\Omega_{jk}\frac{\partial}{\partial R_k} + \frac{R_j}{2}\right)\chi_{\hat{O}}, \tag{3.30}$$

where summation notation is introduced. Or equivalently the anti-commutators

$$\begin{aligned}\chi_{\hat{R}_j\hat{O}+\hat{O}\hat{R}_j} &= -2i\Omega_{jk}\frac{\partial}{\partial R_k}\chi_{\hat{O}}, \\ \chi_{\hat{R}_j\hat{R}_k\hat{O}+\hat{O}\hat{R}_j\hat{R}_k} &= \left(-2\Omega_{jl}\Omega_{km}\frac{\partial^2}{\partial R_l\partial R_m} + i\Omega_{jk} + \frac{R_jR_k}{2}\right)\chi_{\hat{O}},\end{aligned} \tag{3.31}$$

the commutators

$$\begin{aligned}\chi_{\hat{R}_j\hat{O}-\hat{O}\hat{R}_j} &= -R_j\chi_{\hat{O}}, \\ \chi_{\hat{R}_j\hat{R}_k\hat{O}-\hat{O}\hat{R}_j\hat{R}_k} &= i\left[\left(R_k\Omega_{jl} + R_j\Omega_{kl}\right)\frac{\partial}{\partial R_l} + \Omega_{jk}\right]\chi_{\hat{O}},\end{aligned} \tag{3.32}$$

and

$$\chi_{\hat{R}_j\hat{O}\hat{R}_k} = \left\{-\Omega_{jl}\Omega_{km}\frac{\partial^2}{\partial R_l\partial R_m} - \frac{i}{2}\left[\left(R_k\Omega_{jl} - R_j\Omega_{kl}\right)\frac{\partial}{\partial R_l} + \Omega_{jk}\right] - \frac{R_jR_k}{4}\right\}\chi_{\hat{O}}, \tag{3.33}$$

which gives the double commutator

$$\chi_{\hat{R}_j\hat{R}_k\hat{O}+\hat{O}\hat{R}_j\hat{R}_k-2\hat{R}_k\hat{O}\hat{R}_j} = \left[i\left(R_k\Omega_{jl} - R_j\Omega_{kl}\right)\frac{\partial}{\partial R_l} + R_jR_k\right]\chi_{\hat{O}}. \tag{3.34}$$

3.2 Symplectic group

From the anti-symmetric $2n\times2n$ matrix Ω introduced in Eq. (3.10) we can define the symplectic group of $2n\times2n$ matrices $\mathcal{S} \in \mathrm{Sp}(2n,\mathbb{R})$ which satisfy [52, 53, 58]

$$\mathcal{S}\Omega\mathcal{S}^T = \Omega, \tag{3.35}$$

where the symplectic matrix $\mathcal{S}$ has inverse $\mathcal{S}^{-1} = -\Omega\mathcal{S}^T\Omega$.

These symplectic matrices preserve the commutation relations which are encoded in the matrix Ω and so provide valid transformations between quantum states. The displacement and covariance matrices under the action of these symplectic transformations are

$$\boldsymbol{d} \to \mathcal{S}\boldsymbol{d}, \quad \sigma \to \mathcal{S}\sigma\mathcal{S}^T. \tag{3.36}$$

3.2.1 Beam splitter operators

Linear optic transformations take the form

$$\hat{a}'_j = \sum_k U_{jk}\hat{a}_k, \tag{3.37}$$

where the symplectic form of this unitary is

$$\mathcal{S}_U = \begin{pmatrix} \Re U & -\Im U \\ \Im U & \Re U \end{pmatrix}. \tag{3.38}$$

The inverse symplectic transform for this family is simply $\mathcal{S}_U^{-1} = \mathcal{S}^T$. Any such operator can be decomposed in terms of beam splitters and single phase transformations [52, 60, 61].

3.2.2 Squeezing operator

Squeezing is the product of a quadratic Hamiltonian that—unlike the displacement or beam splitter operators—map creation operators to a combination of annihilation and creation operators and vice-versa. A single-mode squeezing is

$$\hat{S}(\xi) = e^{\frac{1}{2}\left[(\xi\hat{a}^\dagger)^2 - \xi^*\hat{a}^2\right]}, \tag{3.39}$$

which has symplectic form

$$\mathcal{S}(\xi) = \begin{pmatrix} \cosh|\xi| + \sinh|\xi|\cos(\arg\xi) & \sinh|\xi|\sin(\arg\xi) \\ \sinh|\xi|\sin(\arg\xi) & \cosh|\xi| - \sinh|\xi|\cos(\arg\xi) \end{pmatrix}, \tag{3.40}$$

with a product local squeezing $\mathcal{S}(\boldsymbol{\xi})$ being $\mathcal{S}(\boldsymbol{\xi}) = \bigotimes_j \mathcal{S}(\xi_j)$. The action of squeezing can be thought of as reducing the uncertainty in the state in one quadrature while increasing it in the orthogonal quadrature.

Multi-mode squeezing—which introduces entanglement between the modes—can be generated with more general squeezing operators than Eq. (3.39). These multi-mode squeezing operators are still quadratic in annihilation and creation

operators, however they can be decomposed in terms of single-mode squeezings in combination with linear optics [62].

3.3 Gaussian states

3.3.1 Phase space representations

Gaussian states can be recognised as those possessing a $2d$-dimensional Gaussian Wigner function. These Wigner functions have form

$$W_{\mathrm{G}}(\boldsymbol{R}) = \frac{1}{\pi^d \sqrt{\det \sigma}} \exp\left[-(\boldsymbol{R}-\boldsymbol{d})^T \sigma^{-1} (\boldsymbol{R}-\boldsymbol{d})\right], \tag{3.41}$$

and are described by a displacement vector $\boldsymbol{d}$ of length $2d$ and a covariance matrix σ of size $2d \times 2d$. The displacements and covariance matrix are defined (analogously to Eqs. (2.1) and (2.2)) as means and covariances of the quadrature operators over the state

$$d_j = \mathrm{Tr}\left(\rho \hat{R}_j\right), \quad \sigma_{jk} = \mathrm{Tr}\left(\rho(\hat{R}_j \hat{R}_k + \hat{R}_k \hat{R}_j)\right) - 2\,\mathrm{Tr}\left(\rho \hat{R}_j\right)\mathrm{Tr}\left(\rho \hat{R}_k\right). \tag{3.42}$$

Similarly the characteristic function for a Gaussian state with moments $\boldsymbol{d}$ and σ is

$$\chi_{\mathrm{G}}(\boldsymbol{R}) = \exp\left[\frac{1}{4}\boldsymbol{R}^T \Omega \sigma \Omega \boldsymbol{R} - i \boldsymbol{R}^T \Omega \boldsymbol{d}\right]. \tag{3.43}$$

The positivity requirement on density matrices translates to a requirement that $\sigma + i\Omega \geq 0$, with the equality indicating a pure Gaussian state [52, 53].

3.3.2 Thermal states

Thermal states are states whose covariance matrix has the form

$$\sigma_{\mathrm{th}} = \bigoplus_j \nu_j \mathbb{1}_{2\times 2}, \tag{3.44}$$

where $\nu_j = 2n_j + 1$ and n_j is the occupation number of the jth mode. The occupation number represents the increased uncertainty above vacuum or ground state fluctuations. This can be generated by the equilibrium state resulting from coupling a system to a thermal bath; such fluctuations can be considered classical in origin. In optical systems the thermal state is relevant at certain frequencies where black-body radiation is present; at sufficiently high frequencies the occupation number is negligible and vacuum is a reasonable assumption.

The thermal states afford a straightforward Fock state representation

$$\rho_{\rm th} = \bigotimes_{j=1}^{d} \frac{1}{1+n_j} \sum_{m=0}^{\infty} \left(\frac{n_j}{1+n_j} \right)^m |m\rangle \langle m| , \tag{3.45}$$

having—excepting the pure state $|0\rangle \langle 0|$ when $n = 0$—infinite rank. The larger n is, the more mixed the state is with the purity of a Gaussian state with covariance matrix $\sigma_{\rm th}$ being [52]

$$\mu = {\rm Tr}\left(\rho_{\rm G}^2\right) = \frac{1}{\sqrt{\det \sigma_{\rm th}}} = \left(\prod_j \nu_j \right)^{-1} . \tag{3.46}$$

An arbitrary Gaussian state can be constructed by taking an arbitrary thermal state and applying arbitrary displacement and (multi-mode) squeezing transformations to it.

3.3.3 Williamson decomposition

The thermal state is the result of the diagonalisation of a covariance matrix by symplectic transformations, namely the Williamson decomposition. Every covariance matrix can be diagonalised by way of a symplectic transformation to yield a diagonal form

$$\mathcal{S}\sigma\mathcal{S}^T = \nu \tag{3.47}$$

where

$$\nu = {\rm diag}(\nu_1, \cdots, \nu_d, \nu_1, \cdots, \nu_d). \tag{3.48}$$

This diagonalisation is stronger than that produced by an orthogonal diagonalisation of a real symmetric matrix which would in general yield a matrix of form

$${\rm diag}(\nu_1 e^{2r_1}, \cdots, \nu_d e^{2r_d}, \nu_1 e^{-2r_1}, \cdots, \nu_d e^{-2r_d}). \tag{3.49}$$

Equations (3.48) and (3.49) are then related by the action of single-mode squeezings.

The symplectic eigenvalues $\{\nu_j\}$ of σ are the conventional eigenvalues of $i\Omega\sigma$ [52, 53, 58]. Hence the determinant of a covariance matrix is straightforwardly derived from the symplectic eigenvalues as $\det \sigma = \prod_j \nu_j^2$.

The specific family of isothermal states have symplectic decomposition $\sigma = \nu\mathcal{S}\mathcal{S}^T$ for which we can recognise—through Eq. (3.35)—that

$$\sigma\Omega\sigma = \nu^2\Omega. \tag{3.50}$$

3.3.4 Unitary Gaussian dynamics

The unitary transformations which map Gaussian states to Gaussian states consist of displacements, linear optics, and squeezings. While these have already been defined we briefly review their action on a Gaussian state with moments $\boldsymbol{d}$ and σ. The displacement operator $\hat{D}(\boldsymbol{\alpha})$ defined in Eq. (3.14) transforms a Gaussian state as

$$\boldsymbol{d} \to \boldsymbol{d} + \sqrt{2}\begin{pmatrix} \Re\boldsymbol{\alpha} \\ \Im\boldsymbol{\alpha} \end{pmatrix}, \quad \sigma \to \sigma. \tag{3.51}$$

producing a translation only of the state. The beam splitter operator U—with symplectic form $\mathcal{S}_U$—defined in Eq. (3.37) transforms a Gaussian state as

$$\boldsymbol{d} \to \begin{pmatrix} \Re U & -\Im U \\ \Im U & \Re U \end{pmatrix}\boldsymbol{d}, \quad \sigma \to \begin{pmatrix} \Re U & \Im U \\ -\Im U & \Re U \end{pmatrix}\sigma\begin{pmatrix} \Re U^T & -\Im U^T \\ \Im U^T & \Re U^T \end{pmatrix}. \tag{3.52}$$

The squeezing operator $\hat{S}(\boldsymbol{\xi})$ (with symplectic form $\mathcal{S}_{\boldsymbol{\xi}}$) defined in Eq. (3.39) transforms a Gaussian state as

$$\boldsymbol{d} \to \mathcal{S}_{\boldsymbol{\xi}}\boldsymbol{d}, \quad \sigma \to \mathcal{S}_{\boldsymbol{\xi}}\sigma\mathcal{S}_{\boldsymbol{\xi}}^T. \tag{3.53}$$

where $\mathcal{S}_{\boldsymbol{\xi}}$ is a general multi-mode squeezing. In the specific case that $\mathcal{S}_{\boldsymbol{\xi}}$ is a set of single-mode squeezings of the $\hat{x}_j$ quadrature (the squeezing in the Bloch-Messiah decomposition [62]) this is

$$\begin{aligned} \boldsymbol{d} &\to \left[\bigoplus_j \begin{pmatrix} e^{-2|\xi|} & 0 \\ 0 & e^{2|\xi|} \end{pmatrix}\right]\boldsymbol{d}, \\ \sigma &\to \left[\bigoplus_j \begin{pmatrix} e^{-2|\xi|} & 0 \\ 0 & e^{2|\xi|} \end{pmatrix}\right]\sigma\left[\bigoplus_j \begin{pmatrix} e^{-2|\xi|} & 0 \\ 0 & e^{2|\xi|} \end{pmatrix}\right]. \end{aligned} \tag{3.54}$$

3.3.5 Gaussian open dynamics

Displacements, beam splitters, and squeezings described in Sections 3.1.1, 3.2.1 and 3.2.2 cover the unitary transformations which map Gaussian states to Gaussian states. More generally one can consider evolution in the presence of Lindbladian terms, under a master equation as outlined in Eq. (1.5).

An arbitrary Lindblad operator will drive a Gaussian state to non-Gaussian state. Dephasing—through a Lindblad operator $\hat{n}$ for example—has this effect on all but the thermal states. The Lindblad operator $\hat{n}$ induces a rotation around the origin of the phase space, which fluctuates according to time and the decoherence strength. Considering the coherent states the steady state is both rotationally symmetric around the origin yet the Wigner function has a local

minimum at the origin and therefore cannot be Gaussian.

We can instead consider the special case where the Lindblad operators are linear combinations of the quadrature operators $\hat{L}_j = \boldsymbol{l}_j^T \hat{\boldsymbol{R}}$ and the Hamiltonian is quadratic in the quadrature operators

$$\frac{\partial \rho}{\partial t} = -i[\frac{1}{2}\hat{\boldsymbol{R}}^T B \hat{\boldsymbol{R}} + \boldsymbol{c}^T \hat{\boldsymbol{R}}, \rho] + \frac{1}{2}\sum_j \left(\hat{L}_j^\dagger \hat{L}_j \rho + \rho \hat{L}_j^\dagger \hat{L}_j - 2\hat{L}_j \rho \hat{L}_j^\dagger\right), \quad (3.55)$$

where B is symmetric. This can be translated into phase space via the characteristic function using Eqs. (3.31) and (3.34) [52, 59]

$$\frac{\partial \chi_\rho}{\partial t} = \left[\boldsymbol{R}^T B \Omega \boldsymbol{\nabla} + i\boldsymbol{c}^T \boldsymbol{R} + \frac{1}{2}\boldsymbol{R}^T \Re\Upsilon \boldsymbol{R} - \boldsymbol{R}^T \Im\Upsilon \Omega \boldsymbol{\nabla}\right] \chi_\rho, \quad (3.56)$$

where $\Upsilon = \sum_j \boldsymbol{l}\boldsymbol{l}^\dagger$. This is in general a first-order partial differential equation (PDE), the Fourier transform of the Fokker-Planck equation [63]

$$\frac{\partial \chi_\rho}{\partial t} = \left[\boldsymbol{R}^T A \boldsymbol{\nabla} + i\boldsymbol{c}^T \boldsymbol{R} + \frac{1}{2}\boldsymbol{R}^T D \boldsymbol{R}\right] \chi_\rho, \quad (3.57)$$

where

$$A = B\Omega - \Im\Upsilon, \quad D = \Re\Upsilon. \quad (3.58)$$

For a Gaussian state characteristic function defined in Eq. (3.43) this PDE becomes

$$-i\boldsymbol{R}^T \Omega \frac{\partial \boldsymbol{d}}{\partial t} + \frac{1}{4}\boldsymbol{R}^T \Omega \frac{\partial \sigma}{\partial t} \Omega \boldsymbol{R} = \boldsymbol{R}^T A \left(\frac{1}{2}\Omega\sigma\Omega\boldsymbol{R} - i\Omega\boldsymbol{d}\right) + i\boldsymbol{c}^T \boldsymbol{R} + \frac{1}{2}\boldsymbol{R}^T D \boldsymbol{R}, \quad (3.59)$$

where we divide by the non-zero characteristic function. Equation (3.59) can then be divided into the terms linear and quadratic in $\boldsymbol{R}$ giving [63]

$$\begin{aligned} \frac{\partial \boldsymbol{d}}{\partial t} &= -\Omega A \Omega \boldsymbol{d} - \Omega \boldsymbol{c}, \\ \frac{\partial \sigma}{\partial t} &= -\Omega A \Omega \sigma - \sigma \Omega A \Omega + 2\Omega D \Omega, \end{aligned} \quad (3.60)$$

which give the evolution directly of the displacement vector and covariance matrix.

3.4 Metrology with Gaussian states

3.4.1 Gaussian quantum Fisher information

We saw in Section 2.3.1 that specific results for the FI exist for a Gaussian probability distribution in terms of its mean and covariances [33, 34]. The same is true of the QFI in relation to Gaussian quantum states [52, 54–56, 64–68].

Expressions for the QFI can be found both through explicitly solving the SLD equation (Eq. (2.22)) specifically for a family of Gaussian states [52, 54, 55, 66–68] and results for the fidelity between two Gaussian states [69–71] from which the QFI can be extracted [56, 64, 65].

We shall here follow the SLD-based argument [52, 54, 55, 66–68] to derive expressions for the QFI by solving for the SLD operator. Taking the trace of the product of Eq. (2.22) with the displacement operator we have

$$\frac{\partial}{\partial\phi_j}\chi_\rho = \mathrm{Tr}\left(\hat{D}(\xi)\frac{\mathcal{L}_j\rho + \rho\mathcal{L}_j}{2}\right), \tag{3.61}$$

immediately bring the left-hand side into phase space. Given a Gaussian state can be expressed as the exponent of a Hamiltonian which is quadratic in the quadrature operators [52], a reasonable ansatz for $\{\mathcal{L}_j\}$ is

$$\mathcal{L}_j = L^{(j_0)} + L_k^{(j_1)}\hat{R}_k + L_{kl}^{(j_2)}\hat{R}_k\hat{R}_l. \tag{3.62}$$

With the ansatz of Eq. (3.62) we write Eq. (3.61) as

$$\begin{aligned}\frac{\partial}{\partial\phi_j}\chi_\rho = L^{(j_0)}\chi_\rho &+ L_k^{(j_1)}\,\mathrm{Tr}\left(\hat{D}(\xi)\frac{\hat{R}_k\rho + \rho\hat{R}_k}{2}\right)\\ &+ L_{kl}^{(j_2)}\,\mathrm{Tr}\left(\hat{D}(\xi)\frac{\hat{R}_k\hat{R}_l\rho + \rho\hat{R}_k\hat{R}_l}{2}\right),\end{aligned} \tag{3.63}$$

where the traces can be rewritten—bringing the equation wholly into phase space quantities—with the aid of Eq. (3.31). This gives

$$\begin{aligned}\frac{\partial}{\partial\phi_j}\chi_\rho = L^{(j_0)}\chi_\rho &- iL_k^{(j_1)}\Omega_{kl}\frac{\partial}{\partial R_l}\chi_\rho\\ &+ L_{kl}^{(j_2)}\left(-\Omega_{km}\Omega_{ln}\frac{\partial^2}{\partial R_m\partial R_n} + \frac{i}{2}\Omega_{kl} + \frac{R_kR_l}{4}\right)\chi_\rho,\end{aligned} \tag{3.64}$$

which we can then connect with the characteristic function of a Gaussian state

(Eq. (3.43)) which has derivatives

$$\begin{aligned}\frac{\partial}{\partial R_j}\chi_{\mathrm{G}} &= \left(\frac{1}{2}\Omega\sigma\Omega\boldsymbol{R} - i\Omega\boldsymbol{d}\right)_j \chi_{\mathrm{G}},\\ \frac{\partial^2}{\partial R_j \partial R_k}\chi_{\mathrm{G}} &= \left[\frac{1}{2}\left(\Omega\sigma\Omega\right)_{jk} + \left(\frac{1}{2}\Omega\sigma\Omega\boldsymbol{R} - i\Omega\boldsymbol{d}\right)_j \left(\frac{1}{2}\Omega\sigma\Omega\boldsymbol{R} - i\Omega\boldsymbol{d}\right)_k\right]\chi_{\mathrm{G}}.\end{aligned} \tag{3.65}$$

Meanwhile the derivative with respect to the parameter ϕ_j gives

$$\frac{\partial}{\partial \phi_j}\chi_{\mathrm{G}} = \left(\frac{1}{4}\boldsymbol{R}^T\Omega\frac{\partial\sigma}{\partial\phi_j}\Omega\boldsymbol{R} - i\frac{\partial\boldsymbol{d}^T}{\partial\phi_j}\Omega\boldsymbol{R}\right)\chi_{\mathrm{G}}. \tag{3.66}$$

Inserting Eqs. (3.65) and (3.66) into Eq. (3.64) we can separately identify three equations

$$0 = L^{(j_0)} + \boldsymbol{L}^{(j_1)}\cdot\boldsymbol{d} + \mathrm{Tr}\left[L^{(j_2)}\left(\frac{1}{2}\sigma + i\Omega + \boldsymbol{d}\boldsymbol{d}^T\right)\right], \tag{3.67}$$

$$i\frac{\partial\boldsymbol{d}}{\partial\phi_j}\Omega\boldsymbol{R} = \frac{i}{2}\boldsymbol{L}^{(j_1)}\sigma\Omega\boldsymbol{R} + \frac{i}{2}\boldsymbol{d}^T\left[L^{(j_2)} + (L^{(j_2)})^T\right]\sigma\Omega\boldsymbol{R}, \tag{3.68}$$

$$\boldsymbol{R}^T\Omega\frac{\partial\sigma}{\partial\phi_j}\Omega\boldsymbol{R} = \boldsymbol{R}^T L^{(j_2)}\boldsymbol{R} + \boldsymbol{R}^T\Omega\sigma L^{(j_2)}\sigma\Omega\boldsymbol{R}, \tag{3.69}$$

for the parts constant, linear, and quadratic in $\boldsymbol{R}$. We note immediately that we require $\mathrm{Tr}\left(L^{(j_2)}\Omega\right) = 0$ to solve for the imaginary part of Eq. (3.67), $L^{(j_2)}$ can be required to be symmetric in order to achieve this[1]. The remaining terms can be rewritten as

$$\frac{\partial\sigma}{\partial\phi_j} = \Omega L^{(j_2)}\Omega + \sigma L^{(j_2)}\sigma, \tag{3.70}$$

$$\boldsymbol{L}^{(j_1)} = 2\sigma^{-1}\frac{\partial\boldsymbol{d}}{\partial\phi_j} - 2L^{(j_2)}\boldsymbol{d}, \tag{3.71}$$

$$L^{(j_0)} = -\left(\boldsymbol{L}^{(j_1)}\right)^T\boldsymbol{d} - \boldsymbol{d}^T L^{(j_2)}\boldsymbol{d} - \frac{1}{2}\mathrm{Tr}\left(L^{(j_2)}\sigma\right), \tag{3.72}$$

where we see that once $L^{(j_2)}$ is identified from Eq. (3.70) the remaining terms can be solved for immediately.

Identifying $\mathcal{A}_\sigma(L^{(j_2)}) = \sigma L^{(j_2)}\sigma + \Omega L^{(j_2)}\Omega$ we have $L^{(j_2)} = \mathcal{A}_\sigma^{-1}(\partial_{\phi_j}\sigma)$ where it exists [52, 54]. Using the Williamson decomposition—introduced in Section 3.3.3—of the covariance matrix $\sigma = \mathcal{S}\nu\mathcal{S}^T$ we have

$$\mathcal{A}_\sigma(L^{(j_2)}) = \mathcal{S}\mathcal{A}_\nu(\mathcal{S}^T L^{(j_2)}\mathcal{S})\mathcal{S}^T, \tag{3.73}$$

where we can now recognise $\mathcal{A}_\nu(M)$ has eigenmatrices $X^{j_{(kl)}}$. These eigenmatrices

[1] $L^{(j_2)} = (L^{(j_2)})^T$ is also required to enforce hermiticity of the overall SLD operator

have elements

$$X_{mn}^{j(kl)} = \begin{cases} \mathfrak{a}_{11}^{(j)} & m = k \text{ and } n = l, \\ \mathfrak{a}_{21}^{(j)} & m = k + d \text{ and } n = l, \\ \mathfrak{a}_{12}^{(j)} & m = k \text{ and } n = l + d, \\ \mathfrak{a}_{22}^{(j)} & m = k + d \text{ and } n = l + d, \end{cases} \tag{3.74}$$

with eigenvalues $\nu_k\nu_l - 1$ for $j \in \{0, 2\}$ and $\nu_k\nu_l + 1$ for $j \in \{1, 3\}$ where $\{\mathfrak{a}^{(j)}\}$ are

$$\mathfrak{a}^{(0)} = \mathbb{1}_{2\times 2}, \quad \mathfrak{a}^{(1)} = \sigma_x, \quad \mathfrak{a}^{(2)} = \Omega_2, \quad \mathfrak{a}^{(3)} = \sigma_z, \tag{3.75}$$

with σ_x and σ_z being the Pauli matrices. We therefore recognise that $\mathcal{A}_\sigma$ is an invertible map as long as all the symplectic eigenvalues are strictly greater than 1, or that no modes are in a pure state. The SLD need only be defined on the support of the states $\{\rho_{\boldsymbol{\phi}}\}$ which does not necessitate $\mathcal{A}_\sigma$ to be completely invertible to evaluate the QFI, we shall address this separately.

Having identified the SLD we can then turn to the QFI calculation using Eqs. (2.24) and (3.20) [52]

$$\begin{aligned} \mathrm{Tr}\left(\partial_{\phi_j}\rho\mathcal{L}_k\right) = &\left[L^{(j_0)} + \boldsymbol{L}^{(j_1)} \cdot \left(i\Omega\boldsymbol{\nabla} + \frac{\boldsymbol{R}}{2}\right)\right. \\ &\left. + \left(i\Omega\boldsymbol{\nabla} + \frac{\boldsymbol{R}}{2}\right)^T L^{(j_2)} \left(i\Omega\boldsymbol{\nabla} + \frac{\boldsymbol{R}}{2}\right)\right] \\ &\left(\frac{1}{4}\boldsymbol{R}^T\Omega\frac{\partial\sigma}{\partial\phi_j}\Omega\boldsymbol{R} - i\frac{\partial\boldsymbol{d}^T}{\partial\phi_j}\Omega\boldsymbol{R}\right)\chi_{\mathrm{G}}\Big|_{\boldsymbol{R}=0} \\ = &\boldsymbol{L}^{(j_1)} \cdot \frac{\partial\boldsymbol{d}}{\partial\phi_k} + \frac{1}{2}\,\mathrm{Tr}\left(L^{(j_2)}\frac{\partial\sigma}{\partial\phi_k}\right) + 2\boldsymbol{d}^T L^{(j_2)}\frac{\partial\boldsymbol{d}}{\partial\phi_k}, \end{aligned} \tag{3.76}$$

where $\nabla_j = \partial/\partial R_j$. In terms of $\mathcal{A}_\sigma^{-1}(\partial_{\phi_j}\sigma)$ using Eq. (3.71)

$$\mathrm{Tr}\left(\partial_{\phi_j}\rho\mathcal{L}_k\right) = 2\frac{\partial\boldsymbol{d}^T}{\partial\phi_j}\sigma^{-1}\frac{\partial\boldsymbol{d}}{\partial\phi_k} + \frac{1}{2}\,\mathrm{Tr}\left[\mathcal{A}_\sigma^{-1}(\partial_{\phi_j}\sigma)\partial_{\phi_k}\sigma\right]. \tag{3.77}$$

Rewriting the second term in a vectorised form this simplifies to

$$H_{jk}(\boldsymbol{\phi}) = 2\frac{\partial\boldsymbol{d}^T}{\partial\phi_j}\sigma^{-1}\frac{\partial\boldsymbol{d}}{\partial\phi_k} + \frac{1}{2}(\partial_{\phi_j}\sigma|(\sigma\otimes\sigma - \Omega\otimes\Omega)^{-1}|\partial_{\phi_k}\sigma), \tag{3.78}$$

where $|AXB^T) = A\otimes B|X)$ and $(A|B) = \mathrm{Tr}\left(A^T B\right)$. We identified earlier that the inverse of $\mathcal{A}_\sigma$ need not exist when the covariance matrix has symplectic eigenvalues equal to 1, this is only a problem when $\partial_{\phi_j}\sigma \neq 0$—if the parameter is encoded only in the displacement then the first term of Eq. (3.78) holds for any

Gaussian state. For states which have at least one symplectic eigenvalue equal to 1 then there are subtleties which must be considered [52, 72]. For this thesis Eq. (3.78) is sufficient for Chapters 4 and 5, in Chapter 6 however we consider pure Gaussian states and so we address the specific case where $\nu_j = 1, \forall j$ next.

Instead we can verify independently the solution for pure states [54, 64, 68]. This can be done through the fidelity of pure states which is the overlap between Wigner functions [64]. The same SLD approach using Eqs. (3.70) to (3.72) can also be used [54] (Monras [54] solves the more general case of Gaussian states with constant and identical Williamson eigenvalues). Equation (3.70) has a simpler solution for pure states which—with Williamson eigenvalues all 1—are themselves symplectic matrices satisfying $\sigma\Omega\sigma = \Omega$ (Eq. (3.50) with $\nu = 1$) and so $L^{(j_2)}$ has a solution [54, 68]

$$L^{(j_2)} = -\frac{1}{2}\frac{\partial}{\partial\phi_j}\sigma^{-1}, \tag{3.79}$$

which gives us a simpler form for the QFI

$$H_{jk} = 2\frac{\partial \boldsymbol{d}^T}{\partial\phi_j}\sigma^{-1}\frac{\partial \boldsymbol{d}}{\partial\phi_k} + \frac{1}{4}\operatorname{Tr}\left[\sigma^{-1}(\partial_{\phi_j}\sigma)\sigma^{-1}(\partial_{\phi_k}\sigma)\right]. \tag{3.80}$$

3.4.2 Attainability of the bound

For single-parameter estimation the eigenstates of the SLD operator prove a sufficient POVM to attain the QCRB. With Gaussian systems the SLD is quadratic in the quadrature operators. The eigenvectors of the SLD operator—at most—are therefore squeezed, displaced Fock states [54, 73].

3.4.3 Homodyne detection

Homodyne detection is the direct measurement of a given quadrature. In optical fields this is performed by the interference of each mode of a state with a strong local oscillator (LO) [52, 58, 74, 75]. In the limit that the LO is sufficiently powerful the statistics of the interfered light give that of the quadrature $\hat{x}_\phi$.

When performed on a Gaussian state its statistics are Gaussian in distribution being the marginal distributions [52, 53]. The mean and covariance of this distribution can be extracted by simply eliminating elements of the mean and covariances associated with the modes orthogonal to those being measured. Thus the FI of the resultant normal distribution can therefore be calculated through Eq. (2.18).

3.4.4 Heterodyne detection

Heterodyne detection involves the simultaneous measurement of orthogonal quadratures [58, 74, 75]. The variance of any one quadrature obtained by heterodyne detection is necessarily larger than that obtained by homodyne measurement of the same quadrature. However heterodyne samples from the joint probabilities of that quadrature and the orthogonal quadrature while homodyne provides no information on the orthogonal quadrature.

Heterodyne detection therefore amounts to measurement of the Q-function [74, 75]. The Q-function can be calculated from a Wigner function by Eq. (3.25) which gives that

$$\boldsymbol{d}_{\mathrm{Het}} = \boldsymbol{d}, \quad \sigma_{\mathrm{Het}} = \sigma + \mathbb{1}, \tag{3.81}$$

from which the FI can be calculated with Eq. (2.18).

Chapter 4

Detecting localisation effects

Quantum mechanics allows for the existence of superposition states: pure states whose measurement statistics are deterministic in a certain basis yet not in another. The existence of such states in small systems can be seen through the existence of qubits [76], spatial superpositions across macroscopic distances [77] and in interferometry of massive objects [78]. Yet despite the success of these experimental efforts quantum superpositions are absent from the macroscopic world.

Collapse models [10, 11, 79] which drive quantum systems into classical states through instantaneous measurement or continuous decoherence have been proposed, originating with Karolyhazy [80], and are best known today through Ghirardi et al. [81] and the continuous spontaneous localisation (CSL) model which followed [82, 83]. The Diósi-Penrose model [84–87]—predated by the similar Karolyhazy [80]—was introduced to potentially account for gravitational effects in quantum mechanics [88]. The same decoherence process has been theorised to arrive from interaction with matter including dark matter candidates [89–92].

Such collapse models can be witnessed in a large range of systems. Analyses have explored mechanical cantilevers [93, 94], ground-based GW detectors [95], LISA Pathfinder [95–97], X-ray emissions [98], trapped ions [99], and neutron stars [100, 101]; these typically focus on bounding possible parameters of the CSL model. Future ventures which have been proposed include the preparation of spatial or mechanical superposition states [102–107] and the space-based MAQRO mission [108, 109]. Quantum mechanical space-based experiments such as MAQRO were the focus of a recent ESA study [110].

By preparing a nanoparticle in a low energy state the effects of decoherence in the position basis—a localisation effect—can be seen through the momentum diffusion it gives rise to, this scheme is illustrated in Fig. 4.1. This can be seen in both traps [111, 112] and in free-fall [108, 109]; MAQRO aims to explore

the latter, employing the significantly longer free-fall times accessible in the microgravity of space to yield a superior sensitivity to these collapse effects through measuring the particle's wavepacket expansion rate.

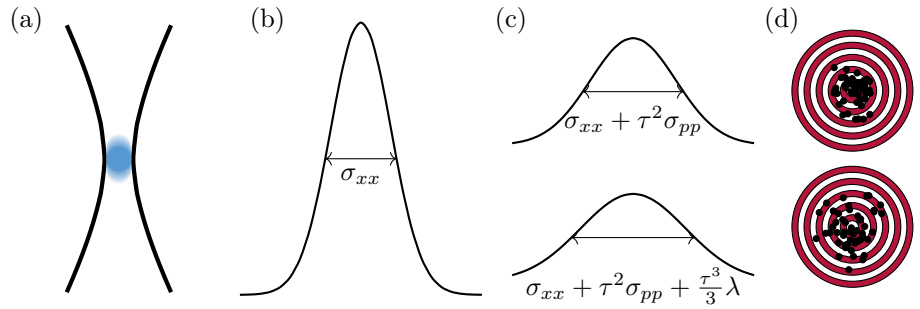

Figure 4.1: A simple wavepacket expansion experiment: (a) A particle is trapped and cooled; (b) the particle is released and has some initial wavepacket; (c) over time the wavepacket expands as the particle moves freely, this expansion is increased by any localisation term; (d) measuring the position repeatedly builds up statistics to enable estimation of any localisation strength (2-d representation for illustrative purposes).

This fits in with ventures exploring quantum enhancements and limits of estimation of noise parameters such as loss [73, 113], decoherence [41, 114], random displacements [115], and stochastic processes [116]. Experimental work towards the quantum control of such optomechanical systems include the control of nanoparticles [117, 118] and development of mechanical squeezing [118–120].

In this chapter results first published as Branford et al. [DB4] are presented which demonstrate the potential enhancements of quantum squeezing and advanced measurements.

4.1 Mechanical system

The mechanical system is described by the dimensionful operators $\hat{X}$ and $\hat{P}$ for which the dimensionless variants are

$$\hat{x} = \sqrt{\frac{m\omega}{\hbar}}\hat{X}, \quad \hat{p} = \frac{1}{\sqrt{\hbar m\omega}}\hat{P}, \tag{4.1}$$

where m is the particle mass and ω the trapping potential frequency. The nanoparticle of mass m is initially placed in a harmonic potential $m\omega^2\hat{X}^2/2$ where it is then cooled (and potentially squeezed) to a (squeezed) thermal state

with dimensionless moments

$$\boldsymbol{d} = \begin{pmatrix} \langle x(0) \rangle \\ \langle p(0) \rangle \end{pmatrix}, \quad \sigma = \nu \begin{pmatrix} \cosh 2r + \sinh 2r \cos 2\phi & \sinh 2r \sin 2\phi \\ \sinh 2r \sin 2\phi & \cosh 2r - \sinh 2r \cos 2\phi \end{pmatrix}, \tag{4.2}$$

which describes the initial state of the particle in the experiment.

4.1.1 Master equation solution

At a time $t = 0$ the trapping potential is turned off and the nanoparticle's state evolves according to a Lindbladian master equation [108, 109]

$$\frac{\partial \rho}{\partial t} = -\frac{i}{\hbar}[\frac{\hat{P}^2}{2m}, \rho] - \Lambda[\hat{X}, [\hat{X}, \rho]], \tag{4.3}$$

which can be rewritten in terms of $\hat{x}$ and $\hat{p}$ as

$$\frac{\partial \rho}{\partial \tau} = -\frac{i}{2}[\hat{p}^2, \rho] - \frac{\lambda}{4}[\hat{x}, [\hat{x}, \rho]], \tag{4.4}$$

where

$$\tau = \omega t, \quad \lambda = \Lambda/\Lambda_0, \quad \Lambda_0 = m\omega^2/(4\hbar). \tag{4.5}$$

Representative values for MAQRO are given in Table 4.1, for MAQRO the $\tau \gg 1$ and $\lambda \ll 1$ limits are most relevant.

Parameter	Symbol	Value
Representative localisation legnth	Λ	10^{10}–$10^{20}\,\mathrm{m^{-2}s^{-1}}$
Mass	m	10^8–$10^{10}\,\mathrm{u}$
Free-fall time	t	$100\,\mathrm{s}$
Trapping frequency	ω	$10^5\,\mathrm{rads^{-1}}$
Thermal occupation number	n_{th}	0.3
Thermal variance	$\nu = 2n_{\mathrm{th}} + 1$	1.6
Limiting localisation[1]	$\Lambda_0 = \frac{m\omega^2}{4\hbar}$	$1.6 \times 10^{26}\,\mathrm{m^{-2}s^{-1}}$
Experimental timescale	$\tau = \omega t$	6.3×10^7

[1] Using $m = 10^8\,\mathrm{u}$

Table 4.1: Representative parameter values for MAQRO [109].

Equation (4.4) takes the form of Eq. (3.55) and so can be solved, for Gaussian input, by Eq. (3.60). For Eq. (4.4) we have

$$B = \begin{pmatrix} 0 & 0 \\ 0 & 1 \end{pmatrix}, \quad \boldsymbol{l} = \begin{pmatrix} \sqrt{\frac{i\lambda}{2}} \\ 0 \end{pmatrix}, \tag{4.6}$$

and so by Eq. (3.58)

$$A = \begin{pmatrix} 0 & 0 \\ -1 & 0 \end{pmatrix}, \quad D = \begin{pmatrix} 0 & 0 \\ 0 & -\frac{\lambda}{2} \end{pmatrix}, \tag{4.7}$$

from which we have—using Eq. (3.60)—equations of motion for the moments

$$\frac{\partial \boldsymbol{d}}{\partial \tau} = \begin{pmatrix} 0 & 1 \\ 0 & 0 \end{pmatrix} \boldsymbol{d}, \tag{4.8}$$

$$\frac{\partial \sigma}{\partial \tau} = \begin{pmatrix} 0 & 1 \\ 0 & 0 \end{pmatrix} \sigma + \sigma \begin{pmatrix} 0 & 1 \\ 0 & 0 \end{pmatrix} + \begin{pmatrix} 0 & 0 \\ 0 & \lambda \end{pmatrix}. \tag{4.9}$$

Equations (4.8) and (4.9) then have relatively straightforward solutions

$$\begin{aligned} \boldsymbol{d}(\tau) &= \begin{pmatrix} \langle x(0)\rangle + \tau\langle p(0)\rangle \\ \langle p(0)\rangle \end{pmatrix}, \\ \sigma(\tau) &= \begin{pmatrix} \sigma_{xx}(0) + 2\tau\sigma_{xp}(0) + \tau^2\sigma_{pp}(0) + \frac{\tau^3}{3}\lambda & \sigma_{xp}(0) + \tau\sigma_{pp}(0) + \frac{\tau^2}{2}\lambda \\ \sigma_{xp}(0) + \tau\sigma_{pp}(0) + \frac{\tau^2}{2}\lambda & \sigma_{pp}(0) + \tau\lambda \end{pmatrix}, \end{aligned} \tag{4.10}$$

where $\sigma_j(0)$ denote the initial covariances defined by Eq. (4.2). Equation (4.10) demonstrates that the diffusion process has no effect on the displacements, which remain constant unless there is some average non-zero momentum of the initial state in which case the wavepacket moves according to that.

4.2 Fundamental limits

From Eq. (4.10) we have the necessary ingredients to evaluate the QFI using Eq. (3.78), wherefrom only the second term is required as $\partial_\Lambda \boldsymbol{d}(\tau) = 0$. The QFI then gives the QCRB

$$(\Delta\Lambda)^2 \geq \frac{\Lambda_0^2 \left[\left(\nu^2 + \tau\nu\lambda Z + \frac{\tau^4}{12}\lambda^2\right)^2 - 1\right]}{\frac{\tau^4}{12}\left(\nu^2 + \tau\nu\lambda Z + \frac{\tau^4}{12}\lambda^2\right) + \frac{\tau^4}{12}\left(1 - 2\nu^2\right) + \frac{\tau^2}{4}\nu^2 Z^2}, \tag{4.11}$$

where

$$Z = \left(1 + \frac{\tau^2}{3}\right)\cosh 2r + \left[\left(1 - \frac{\tau^2}{3}\right)\cos 2\phi + \tau \sin 2\phi\right]\sinh 2r. \tag{4.12}$$

Before tuning parameters of Eq. (4.11)—such as squeezing angle ϕ in Section 4.2.1—we look at the behaviour to highest order in Λ which is

$$(\Delta\Lambda)^2 \gtrsim \Lambda^2, \tag{4.13}$$

for which the signal-to-noise ratio (SNR) of 1 is available from a single experiment, with repetitions able to increase the statistical significance to actually identify a non-zero Λ for the purposes of collapse models. The SNR is defined as $(\Delta\Lambda)^2/\Lambda^2$ which gives a measure of fractional error, around 1 a non-zero measurement has limited statistical significance but through repetitions to reduce the uncertainty this can be reduced to render a non-zero detection statistically significant.

In the opposite limit $\Lambda \to 0$ this is

$$(\Delta\Lambda)^2 \gtrsim \Lambda_0^2 \left[\frac{\nu^2+1}{\frac{\tau^2}{4}\left(\frac{\nu^2}{\nu^2-1}Z^2 - \frac{\tau^2}{3}\right)} \right], \tag{4.14}$$

which is constant with Λ and so the CRB is constant; this sets an order of magnitude limit in terms of the minimum Λ which a given experiment can resolve, below this the SNR grows as $1/\Lambda$ and even smaller values of Λ begin to require a prohibitive number of repetitions to resolve.

4.2.1 Optimal squeezing angle

We now turn to exploring how tuning the quadrature which is squeezed affects the precision. The lower bound of Eq. (4.11) has form $B(Z(\phi))$ and so by the chain rule

$$\frac{\partial B}{\partial \phi} = \frac{\partial B}{\partial Z}\frac{\partial Z}{\partial \phi}, \tag{4.15}$$

which has potential roots for $\frac{\partial B}{\partial Z} = 0$, or $\frac{\partial Z}{\partial \phi} = 0$. The former $\frac{\partial B}{\partial Z} = 0$, has solutions

$$\begin{aligned} Z_\pm = &\frac{144(1-\nu^4) + 24\lambda^2\tau^4(1-2\nu^2) + \lambda^4\tau^8}{288\lambda\nu^3\tau} \\ &\pm \frac{\left|12(1-\nu^2) + \lambda^2\tau^4\right| \sqrt{[12(1+\nu^2) + \lambda^2\tau^4]^2 - 48\lambda^2\nu^2\tau^4}}{288\lambda\nu^3\tau}. \end{aligned} \tag{4.16}$$

The root Z_- is negative and so is not possible as Eq. (4.12) is positive for $r \geq 0$. The other root Z_+ is not necessarily negative but its second derivative $\left.\frac{\partial^2 B}{\partial Z^2}\right|_{Z=Z_+}$ is negative, indicating a maximum of B only. Instead the roots of $\frac{\partial Z}{\partial \phi} = 0$ are

$$\phi_\pm = \arctan\left(\frac{-3+\tau^2 \pm \sqrt{9+3\tau^2+\tau^4}}{3\tau}\right), \tag{4.17}$$

which can be rewritten

$$\phi_\pm = \arctan\left(\frac{\frac{3\tau-\sqrt{9+3\tau^2+\tau^4}}{3-\tau^2} \pm 1}{1 \mp \frac{3\tau-\sqrt{9+3\tau^2+\tau^4}}{3-\tau^2}}\right), \tag{4.18}$$

which given the arctangent identity

$$\arctan\left(\frac{\alpha \pm \beta}{1 \mp \alpha\beta}\right) = \arctan\alpha \pm \arctan\beta \tag{4.19}$$

yields

$$|\phi_+ - \phi_-| = \pi/2. \tag{4.20}$$

For $\phi_\pm$ we have

$$Z(\phi_\pm) = \left[\left(1 + \frac{\tau^2}{3}\right)\cosh 2r \pm \frac{\sqrt{9 + 3\tau^2 + \tau^4}}{3}\sinh 2r\right], \tag{4.21}$$

B is then minimised by

$$(\Delta\Lambda)^2 \geq \min\left\{\frac{\Lambda_0^2\left[\left(\nu^2 + \tau\nu\lambda Z_+ + \frac{\tau^4}{12}\lambda^2\right)^2 - 1\right]}{\frac{\tau^4}{12}\left(\nu^2 + \tau\nu\lambda Z_+ + \frac{\tau^4}{12}\lambda^2\right) + \frac{\tau^4}{12}(1 - 2\nu^2) + \frac{1}{4}\nu^2\tau^2 Z_+^2}, \right.$$
$$\left.\frac{\Lambda_0^2\left[\left(\nu^2 + \tau\nu\lambda Z_- + \frac{\tau^4}{12}\lambda^2\right)^2 - 1\right]}{\frac{\tau^4}{12}\left(\nu^2 + \tau\nu\lambda Z_- + \frac{\tau^4}{12}\lambda^2\right) + \frac{\tau^4}{12}(1 - 2\nu^2) + \frac{\tau^2}{4}\nu^2 Z_-^2}\right\}, \tag{4.22}$$

where $Z_\pm$ are given by Eq. (4.21). These expressions have form $\frac{a\pm b}{c\pm d}$ with $a > b$ and $c > d$ for which

$$\frac{a+b}{c+d} > \frac{a-b}{c-d} \Leftrightarrow bc > ad \tag{4.23}$$

and so ϕ_- yields a superior precision for

$$\lambda\tau\left[\frac{\tau^2}{12}\left(\frac{\lambda^2\tau^4}{12} + 1\right)^2 - \nu^4\left(\frac{\tau^4}{9} + \frac{7\tau^2}{12} + 1\right) - \frac{\tau^2}{3}\nu^4\cosh^2 2r - \frac{\tau^2}{6}\nu^2\left(\frac{\lambda^2\tau^4}{12} - 1\right)\right]$$
$$+ \nu\left(1 + \frac{\tau^2}{3}\right)\cosh 2r\left[-\nu^4 - \frac{\tau^4}{3}\nu^2\lambda^2 + \left(\frac{\lambda^2\tau^4}{12} + 1\right)^2\right] > 0. \tag{4.24}$$

4.3 Homodyne measurements

As suggested, and illustrated in Fig. 4.1, position measurements will yield information about the localisation rate Λ. Position is one of the family of quadrature operators $\hat{x}(\theta) = \hat{x}\cos\theta + \hat{p}\sin\theta$, whose measurement we can consider through homodyne detection introduced in Section 3.4.3. The moments of the

marginal of the Wigner function are

$$\begin{aligned} w &= [\langle x\rangle + \langle p\rangle\tau]\cos\theta + \langle p\rangle \sin\theta, \\ \Sigma &= \nu\Big[\left[(1+\tau^2)\cos^2\theta + \tau\sin 2\theta + \sin^2\theta\right]\cosh 2r \\ &\quad + \left\{\left[(1-\tau^2)\cos^2\theta - \tau\sin 2\theta - \sin^2\theta\right]\cos 2\phi \right. \\ &\quad \left. + \left[2\tau\cos^2\theta + \sin 2\theta\right]\sin 2\phi\right\}\sinh 2r \\ &\quad + \lambda\left(\frac{\tau^3}{3}\cos^2\theta + \frac{\tau^2}{2}\sin 2\theta + \tau\sin^2\theta\right)\Big], \end{aligned} \tag{4.25}$$

with $\theta = 0$ corresponding to measurement of position and $\theta = \pi/2$ corresponding to measurement of momentum. As with the state itself the mean w has no dependence on Λ, any dependence is limited to the variance Σ. The CRB associated with homodyne detection can then be calculated from Eq. (2.18) yielding

$$\begin{aligned} (\Delta\Lambda)^2 \geq 2\Lambda_0^2\Bigg[\lambda + \nu\Bigg(&\frac{\tau^2\cos^2\theta + \tau\sin 2\theta + 1}{\frac{\tau^3}{3}\cos^2\theta + \frac{\tau^2}{2}\sin 2\theta + \tau\sin^2\theta}\cosh 2r \\ &- \frac{\left(\tau^2\cos^2\theta + \tau\sin 2\theta - \cos 2\theta\right)\cos 2\phi}{\frac{\tau^3}{3}\cos^2\theta + \frac{\tau^2}{2}\sin 2\theta + \tau\sin^2\theta}\sinh 2r \\ &+ \frac{\left(2\tau\cos^2\theta + \sin 2\theta\right)\sin 2\phi}{\frac{\tau^3}{3}\cos^2\theta + \frac{\tau^2}{2}\sin 2\theta + \tau\sin^2\theta}\sinh 2r\Bigg)\Bigg]^2, \end{aligned} \tag{4.26}$$

which clearly shows the same two limits as Eqs. (4.13) and (4.14)—as the first or second term inside the square dominate—of constant SNR and constant CRB. In the absence of squeezing Eq. (4.26) reduces to

$$(\Delta\Lambda)^2 \geq 2\Lambda_0^2\left[\lambda + \nu\frac{\tau^2\cos^2\theta + \tau\sin 2\theta + 1}{\frac{\tau^3}{3}\cos^2\theta + \frac{\tau^2}{2}\sin 2\theta + \tau\sin^2\theta}\right]^2. \tag{4.27}$$

To highest order in Λ Eq. (4.26) becomes

$$(\Delta\Lambda)^2 \gtrsim 2\Lambda^2, \tag{4.28}$$

falling a factor of 2 short of Eq. (4.13). In the opposite limit $\Lambda \to 0$ Eq. (4.26)

becomes

$$(\Delta\Lambda)^2 \gtrsim 2\Lambda_0^2\nu^2\Bigg(\frac{\tau^2\cos^2\theta+\tau\sin 2\theta+1}{\frac{\tau^3}{3}\cos^2\theta+\frac{\tau^2}{2}\sin 2\theta+\tau\sin^2\theta}\cosh 2r \\ -\frac{\left(\tau^2\cos^2\theta+\tau\sin 2\theta-\cos 2\theta\right)\cos 2\phi}{\frac{\tau^3}{3}\cos^2\theta+\frac{\tau^2}{2}\sin 2\theta+\tau\sin^2\theta}\sinh 2r \\ +\frac{\left(2\tau\cos^2\theta+\sin 2\theta\right)\sin 2\phi}{\frac{\tau^3}{3}\cos^2\theta+\frac{\tau^2}{2}\sin 2\theta+\tau\sin^2\theta}\sinh 2r\Bigg)^2, \tag{4.29}$$

setting the minimum order of magnitude Λ any homodyne detection scheme is sensitive to.

4.3.1 Optimal squeezing angle

First we consider which quadrature is optimal to squeeze in order to maximise the precision. The only dependence on ϕ of Eq. (4.26) is in the numerator of the coefficient of $\sinh 2r$. As the other terms inside the square are all positive we clearly need to minimise the coefficient of $\sinh 2r$ in order to minimise the whole quantity which is

$$\underset{\phi}{\operatorname{argmin}}\left\{-\left(\tau^2\cos^2\theta+\tau\sin 2\theta-\cos 2\theta\right)\cos 2\phi+\left(2\tau\cos^2\theta+\sin 2\theta\right)\sin 2\phi\right\}. \tag{4.30}$$

Through differentiation we find Eq. (4.30) to yield

$$\phi=-\arctan\left(\frac{1}{\tau+\tan\theta}\right) \mod \pi, \tag{4.31}$$

where the modulus is given to keep $\phi\in[0,\pi]$. For $\tau\gg 1$, Eq. (4.31) approaches $\phi\approx 0$ which is squeezing of the momentum quadrature. With the squeezing angle given in Eq. (4.31), Eq. (4.26) reduces to

$$(\Delta\Lambda)^2 \geq 2\Lambda_0^2\left[\lambda+\nu e^{-2r}\left(\frac{\tau^2\cos^2\theta+\tau\sin 2\theta+1}{\frac{\tau^3}{3}\cos^2\theta+\frac{\tau^2}{2}\sin 2\theta+\tau\sin^2\theta}\right)\right]^2, \tag{4.32}$$

allowing for squeezing to compensate for increased centre of motion energy, going below the zero-phonon limit of $\nu=1$. Indeed other than ν being replaced by νe^{-2r}, Eq. (4.32) matches Eq. (4.27). For $\tau\gg 1$ Eq. (4.32) behaves as

$$(\Delta\Lambda)^2 \gtrsim 2\Lambda_0^2\left[\lambda+\nu e^{-2r}\frac{k(\theta)}{\tau}\right]^2, \tag{4.33}$$

showing that—as the precision is constant for constant $e^{2r}\tau$—squeezing can also be used to compensate for shorter free-fall times with 10 dB of squeezing at a free-fall time t being equivalent to a free-fall time of $10t$.

4.3.2 Position and momentum measurements

The two most obvious limiting cases of homodyne are when position or momentum is measured directly: these are both straightforward limits of Eq. (4.26). When measuring position the CRB—the $\theta = 0$ limit of Eq. (4.26)—is

$$(\Delta\Lambda)^2 \geq 2\Lambda_0^2 \left[\lambda + \nu \left(\frac{\left[1+\tau^2\right]\cosh 2r + \left\{\left[1-\tau^2\right]\cos 2\phi + 2\tau \sin 2\phi\right\}\sinh 2r}{\tau^3/3} \right)\right]^2, \tag{4.34}$$

in the $\tau \gg 1$ limits this becomes

$$(\Delta\Lambda)^2 \gtrsim 2\Lambda_0^2 \left[\lambda + \nu \frac{\cosh 2r - \sinh 2r \cos 2\phi}{\tau/3}\right]^2, \tag{4.35}$$

showing momentum to be the best quadrature to squeeze.

More generally the optimal squeezing angle for the bound Eq. (4.34) is

$$\phi = -\arctan\left(\frac{1}{\tau}\right) \mod \pi, \tag{4.36}$$

which tends to momentum squeezing for $\tau \gg 1$ and position squeezing for $\tau \ll 1$ with a precision

$$(\Delta\Lambda)^2 \geq 2\Lambda_0^2 \left[\lambda + 3\nu \frac{e^{-2r}}{\tau}\right]^2. \tag{4.37}$$

Directly measuring momentum the CRB—the $\theta = \pi/2$ limit of Eq. (4.26)—is

$$(\Delta\Lambda)^2 \geq 2\Lambda_0^2 \left[\lambda + \nu \frac{\cosh 2r - \sinh 2r \cos 2\phi}{\tau}\right]^2, \tag{4.38}$$

where the bound is trivially minimised by $\phi = 0$ (which can also be seen by inserting $\theta = \pi/2$ to Eq. (4.31)) yielding

$$(\Delta\Lambda)^2 \geq 2\Lambda_0^2 \left[\lambda + \nu \frac{e^{-2r}}{\tau}\right]^2, \tag{4.39}$$

which shows a factor of 9 improvement in precision for sufficiently small Λ relative to measurement of the position quadrature.

4.3.3 Optimal homodyne quadrature

In general we can look at the value of θ which maximises the attainable precision. Plotting Eq. (4.27) against θ for the parameters of Table 4.1, Fig. 4.2 shows there to be some dependence on θ, with $\theta = \pi/2$ (momentum measurement) offering an improvement. The optimality of $\theta = \pi/2$ is not obvious from Fig. 4.2

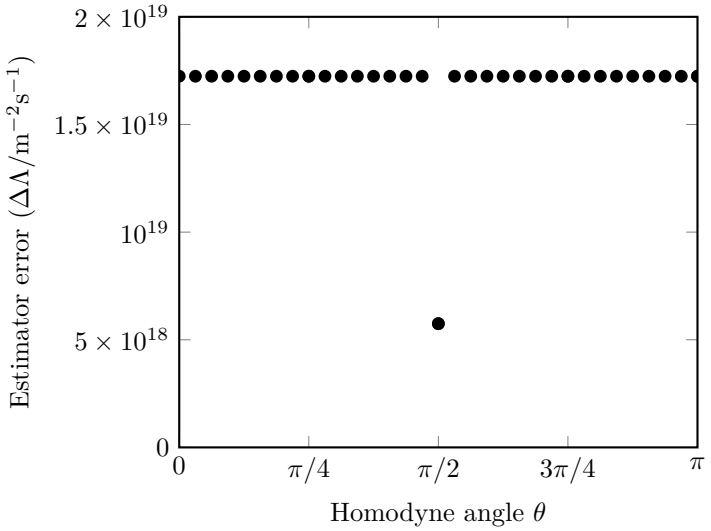

Figure 4.2: Homodyne precision for varying quadratures with $\Lambda = 10^{10}$, $r = 0$, and values otherwise as Table 4.1. Data points at $\theta \in \{0, \pi/32, \pi/16, \cdots, \pi\}$.

as the $\theta/2$ feature is clearly very sharp, instead we can proceed to exactly solve for the value of θ which maximises Eq. (4.32).

From Eq. (4.32)—similarly to the optimisation of squeezing angle from Eq. (4.30)—we need only minimise the second term in the square of Eq. (4.32). Thence we find the optimal θ to measure to be

$$\theta_{\mathrm{opt}} = -\arctan\left(\frac{3 + 2\tau^2 + \sqrt{9 + 3\tau^2 + \tau^4}}{3\tau}\right) \mod \pi, \tag{4.40}$$

for which the CRB then becomes

$$(\Delta\Lambda)^2 \geq 2\Lambda_0^2 \left[\lambda + \nu e^{-2r} \frac{3 + \tau^2 - \sqrt{9 + 3\tau^2 + \tau^4}}{\tau^3/2}\right]^2, \tag{4.41}$$

where the second term now scales better than Eqs. (4.37) and (4.39) for large τ, tending to

$$(\Delta\Lambda)^2 \geq 2\Lambda_0^2 \left[\lambda + \nu \frac{3e^{-2r}}{\tau^3}\right]^2, \tag{4.42}$$

rather than $1/\tau$ of Eqs. (4.37) and (4.39). While for small τ tending to

$$(\Delta\Lambda)^2 \geq 2\Lambda_0^2 \left[\lambda + \nu\frac{e^{-2r}}{\tau}\right]^2, \tag{4.43}$$

now in line with the $1/\tau$ of Eqs. (4.37) and (4.39).

Returning to Fig. 4.2, Eq. (4.41) shows significant improvements on even momentum, suggesting an even narrower feature upon which $\theta = \pi/2$ is just a point on the shoulder, with much greater improvements available. Figure 4.3 demonstrates how deep but also how narrow the improvement of Eq. (4.41) is compared to Eqs. (4.37) and (4.39). The relative difference between position, momentum, and the optimal quadrature can be seen for MAQRO values over a range of Λ values in Fig. 4.8.

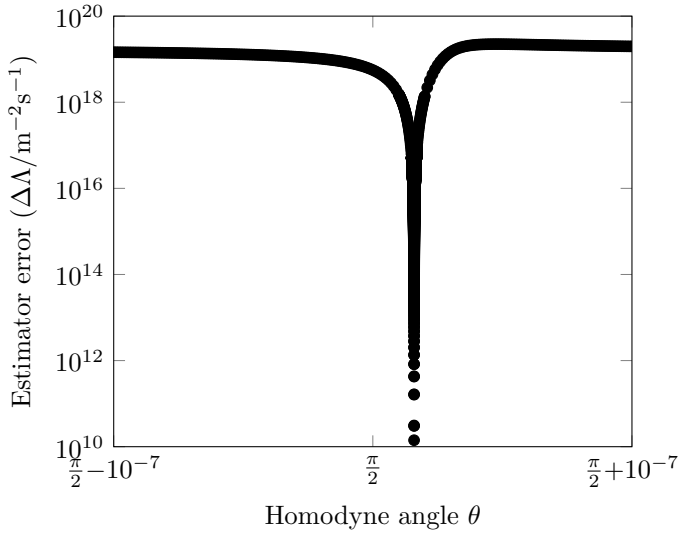

Figure 4.3: Homodyne precision with varying θ around the optimal quadrature identified in Eq. (4.40) $\Lambda = 10^{10}$, $r = 0$, and values otherwise as Table 4.1.

While Fig. 4.3 is perhaps discouraging given the sharpness of the feature we can also estimate how this changes by evaluating the second derivative of Eq. (4.27) at θ_{opt} shows that the dip is less narrow around the bottom as τ increases. Reduced free-fall times are inevitable on lab-based experiments where such general quadrature measurements will be easier to realise, while for certain purposes it may be possible to reduce τ and thus the associated sensitivity while still achieving the desired task as Section 4.6.1 suggests for a test of CSL.

The homodyne angle θ_{opt} presents somewhat counter-intuitively given the diffusion process initially encodes the parameter into the variance of the momentum operator. Nor is the measured quadrature that which is most squeezed (as per

Eq. (4.10)) but somewhere in between, this is also true in laser-interferometric GW detectors which measure displacements [121, 122] (see also Chapter 5 for related analysis).

4.3.4 Optimality of homodyne detection

We can evaluate the general performance of this homodyne detection scheme by considering the ratio $\mathcal{R}_{\text{Hom}} = F_{\text{Hom}}(\Lambda)/H(\Lambda)$. For simplicity we take the case $\nu = 1$ corresponding to preparation of the nanoparticle in the ground state, consequently the ratio is

$$\mathcal{R}_{\text{Hom}} = \frac{\frac{\tau^4}{72}\left\{\left[\lambda\tau\left(1+\frac{\tau^2}{3}+\frac{\tau^3}{12}\lambda\right)+1\right]^2-1\right\}}{\left(1+\frac{\tau^2}{3}+\frac{\tau^3}{6}\lambda-\frac{\sqrt{9+3\tau^2+\tau^4}}{3}\right)^2\left[\left(1+\frac{\tau^2}{3}+\frac{\tau^3}{12}\lambda\right)^2-\frac{1}{2}\left(1+\frac{\tau^2}{3}\right)\left(1+\frac{\tau^2}{3}+\frac{\tau^3}{6}\lambda\right)\right]}, \tag{4.44}$$

which is plotted in Fig. 4.4. Figure 4.4 shows homodyne attaining the QCRB

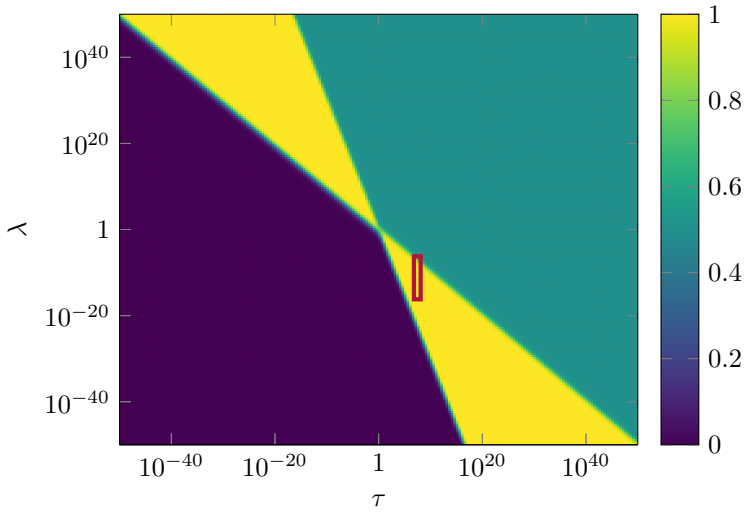

Figure 4.4: Ratio of Fisher information for measurement of the optimal quadrature against quantum Fisher information ($F_{\text{Hom}}(\Lambda)/H(\Lambda)$), plotted for $\nu = 1$ and $r = 0$. λ and τ are dimensionless quantities defined in Eq. (4.5) and are representative of the collapse rate, and experimental timescale. The red box denotes representative values for MAQRO.

for $\lambda\tau \gtrsim 1$ and $\lambda\tau^3 \lesssim 1$, and $\lambda\tau \lesssim 1$ and $\lambda\tau^3 \gtrsim 1$. For $\lambda\tau \gtrsim 1$ and $\lambda\tau^3 \gtrsim 1$ homodyne falls short by a mere factor of 2, while for $\lambda\tau \lesssim 1$ and $\lambda\tau^3 \lesssim 1$ homodyne falls significantly short of the QCRB.

4.4 Heterodyne detection

Heterodyne detection, introduced in Section 3.4.4 can also be considered. The statistics of heterodyne detection performed on a single-mode state are two-dimensional Gaussian distributions with moments related to Eq. (4.10) by Eq. (3.81). Once again the mean plays no role, having no parameter dependence, but the covariance matrix of the heterodyne statistics is

$$\Sigma(\tau) = \begin{pmatrix} 1+\sigma_{xx}(0)+2\tau\sigma_{xp}(0)+\tau^2\sigma_{pp}(0)+\frac{\tau^3}{3}\lambda & \sigma_{xp}(0)+\tau\sigma_{pp}(0)+\frac{\tau^2}{2}\lambda \\ \sigma_{xp}(0)+\tau\sigma_{pp}(0)+\frac{\tau^2}{2}\lambda & 1+\sigma_{pp}(0)+\lambda\tau \end{pmatrix}, \tag{4.45}$$

and the FI is then calculable by Eq. (2.18). This yields a CRB from heterodyne measurements of

$$(\Delta\Lambda)^2 \geq \Lambda_0^2|\Sigma(\tau)|^2\left\{\frac{\tau^4}{12}|\Sigma(\tau)| + \frac{\tau^2}{2}\left(1+\sigma_{xx}(0)+\tau\sigma_{xp}(0)+\frac{\tau^2}{3}\sigma_{pp}(0)\right)^2 + \frac{\tau^4}{6}\left[\left(1+\frac{\tau^2}{3}+\sigma_{xx}(0)\right)(1-\sigma_{pp}(0))+\sigma_{xp}(0)^2\right]\right\}^{-1}, \tag{4.46}$$

without mechanical squeezing ($r = 0$) this is

$$(\Delta\Lambda)^2 \geq \Lambda_0^2|\Sigma(\tau)|^2\left\{\frac{\tau^4}{12}|\Sigma(\tau)| + \frac{\tau^2}{2}\left[1+\nu\left(1+\frac{\tau^2}{3}\right)\right]^2 + \frac{\tau^4}{6}\left[\left(1+\frac{\tau^2}{3}+\nu\right)(1-\nu)\right]\right\}^{-1}, \tag{4.47}$$

where $|\Sigma(\tau)|$ becomes $\nu\tau^2 + (1+\nu)^2 + \tau\lambda(1+\nu)\left(1+\frac{\tau^2}{3}\right) + \frac{\tau^4}{12}\lambda^2$. In contrast to homodyne detection this tends to the QCRB for the highest order in Λ of $(\Delta\Lambda)^2 \gtrsim \Lambda^2$.

4.4.1 Relative performance of heterodyne

We can, in the same manner as homodyne, evaluate the general performance of this heterodyne detection scheme by considering the ratio $\mathcal{R}_{\text{Het}} = F_{\text{Het}}(\Lambda)/H(\Lambda)$. For simplicity we take the case $\nu = 1$ corresponding to preparation of the nanoparticle in the ground state, consequently the ratio is

$$\mathcal{R}_{\text{Het}} = \frac{\frac{1}{16}\left\{\left[\lambda\tau\left(1+\frac{\tau^2}{3}+\lambda\frac{\tau^3}{12}\right)+1\right]^2-1\right\}\left[\left(1+\frac{\tau^2}{3}+\lambda\frac{\tau^3}{12}\right)^2+\left(1+\frac{\tau^2}{6}\right)^2\right]}{(1+\frac{\tau}{2}\lambda)^2\left(1+\frac{\tau^2}{4}+\frac{\lambda\tau^3}{24}\right)^2\left[\left(1+\frac{\tau^2}{3}+\frac{\lambda\tau^3}{12}\right)^2-\frac{1}{2}\left(1+\frac{\tau^2}{3}\right)\left(1+\frac{\tau^2}{3}+\frac{\lambda\tau^3}{6}\right)\right]}. \tag{4.48}$$

which is plotted in Fig. 4.5. Figure 4.5 shows heterodyne detection attaining the QCRB for $\lambda\tau \gtrsim 1$ while falling significantly short for $\lambda\tau \lesssim 1$.

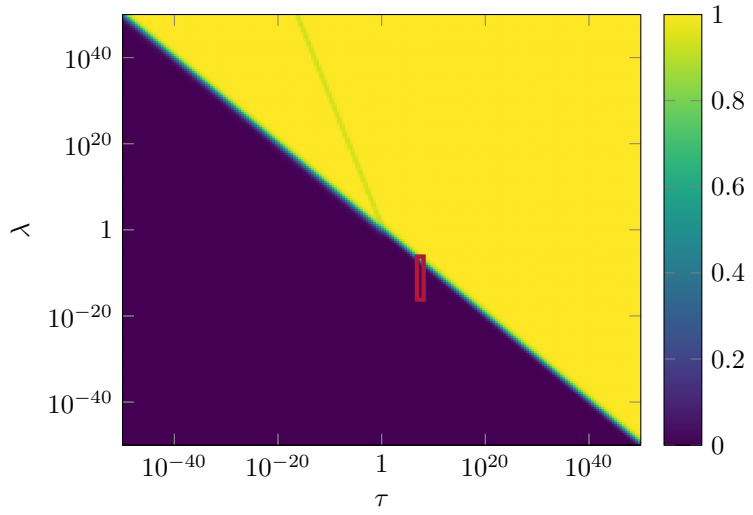

Figure 4.5: Ratio of Fisher information for heterodyne detection against quantum Fisher information ($F_{\text{Het}}(\Lambda)/H(\Lambda)$), plotted for $\nu = 1$ and $r = 0$. λ and τ are dimensionless quantities defined in Eq. (4.5) and are representative of the collapse rate, and experimental timescale. The red box denotes representative values for MAQRO.

As we can see from comparing Figs. 4.4 and 4.5 or by looking at the $\lambda \to \infty$ limit heterodyne detection has a factor of 2 advantage in certain regimes. While these cases can easily be identified, in the small λ and small τ both fall significantly short of the QCRB. If both fall significantly short of the QCRB we cannot use Figs. 4.4 and 4.5 to compare the relative performance of heterodyne and homodyne. Hence we plot the ratio $\mathcal{R}_{\text{Het/Hom}} = F_{\text{Het}}(\Lambda)/F_{\text{Hom}}(\Lambda)$ given for $r = 0$ and $\nu = 1$ by

$$\mathcal{R}_{\text{Het/Hom}} = \frac{9}{2\tau^4} \frac{\left[\left(1+\frac{\tau^2}{3}+\lambda\frac{\tau^3}{12}\right)^2 + \left(1+\frac{\tau^2}{6}\right)^2\right]\left(1+\frac{\tau^2}{3}+\frac{\tau^3}{6}\lambda - \frac{\sqrt{9+3\tau^2+\tau^4}}{3}\right)^2}{(1+\frac{\tau}{2}\lambda)^2\left(1+\frac{\tau^2}{4}+\frac{\lambda\tau^3}{24}\right)^2}, \tag{4.49}$$

in Fig. 4.6 to make the comparison across the full regime.

From Fig. 4.6 we see that outside of $\tau \gtrsim 1$ and $\lambda\tau \lesssim 1$ heterodyne and homodyne detection schemes perform comparably with each other, for $\lambda\tau \gtrsim 1$ this is equally well, with both being within a factor of 2 while for $\lambda\tau \lesssim 1$ and $\tau \lesssim 1$ this is equally badly. For $\lambda\tau \lesssim 1$ and $\tau \gtrsim 1$ though homodyne detection performs significantly better, while—through comparison of Figs. 4.4 and 4.5—this could be expected for $\lambda\tau \lesssim 1$ and $\lambda\tau^3 \gtrsim 1$, for $\tau \gtrsim 1$ and $\lambda\tau^3 \lesssim 1$ this is in spite of both falling completely short of the QCRB.

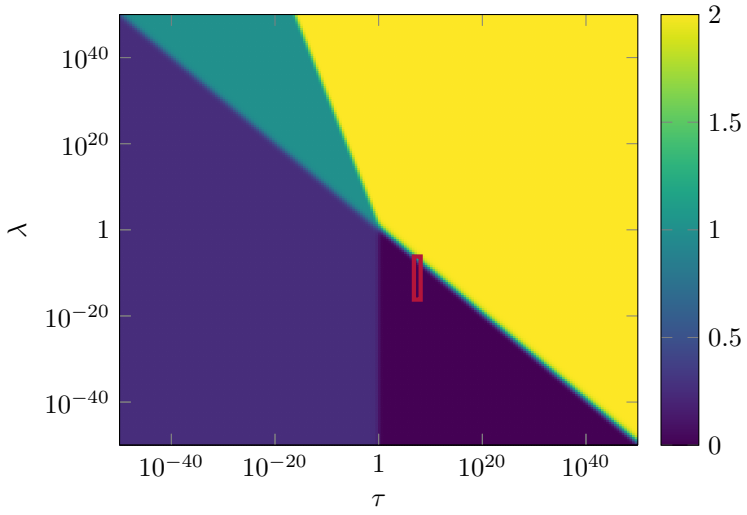

Figure 4.6: Ratio of Fisher information for heterodyne detection against Fisher information for measurement of the optimal quadrature ($F_{\mathrm{Het}}(\Lambda)/F_{\mathrm{Hom}}(\Lambda)$), plotted for $\nu = 1$ and $r = 0$. λ and τ are dimensionless quantities defined in Eq. (4.5) and are representative of the collapse rate, and experimental timescale. The red box denotes representative values for MAQRO.

4.5 Optimal measurement

The SLD operator for a family of Gaussian states identified by Eqs. (3.62) and (3.70) to (3.72) is a quadratic function of the quadrature operators $\hat{x}$ and $\hat{p}$; such an operator can be related—through squeezings and displacements—to the number operator. Then—through Eq. (2.34)—we can identify a set of squeezings and displacements which, when followed by measurements in the Fock basis, attain the QCRB [52, 54]. The Fock states of a mechanical system are then phonons which can, although currently with high noise, be measured experimentally [123, 124].

If we assume that $\langle x(0)\rangle = 0$ and $\langle p(0)\rangle = 0$ can be achieved then we need only solve Eq. (3.70) for $L^{(2)}$, as $\boldsymbol{L}^{(1)} = 0$ and $L^{(0)}$ has a contribution proportional to the identity operator. For the state covariance matrix given in Eq. (4.10), Eq. (3.70) is

$$\begin{aligned}
\frac{\tau^3}{\Lambda_0} &= L_{11}^{(2)}\sigma_{xx}(\tau)^2 + 2L_{12}^{(2)}\sigma_{xx}(\tau)\sigma_{xp}(\tau) + L_{22}^{(2)}\left(\sigma_{xp}(\tau)^2 - 1\right), \\
\frac{\tau^2}{2\Lambda_0} &= L_{11}^{(2)}\sigma_{xx}(\tau)\sigma_{xp}(\tau) + L_{12}^{(2)}\left(\sigma_{xx}(\tau)\sigma_{pp}(\tau) + \sigma_{xp}(\tau)^2 + 1\right) + L_{22}^{(2)}\sigma_{xp}(\tau)\sigma_{pp}(\tau), \\
\frac{\tau}{\Lambda_0} &= L_{11}^{(2)}\left(\sigma_{xp}(\tau)^2 - 1\right) + 2L_{12}^{(2)}\sigma_{xp}(\tau)\sigma_{pp}(\tau) + L_{22}^{(2)}\sigma_{pp}(\tau)^2,
\end{aligned} \tag{4.50}$$

which has solution

$$L^{(2)} = \frac{\tau}{\Lambda_0(|\sigma(\tau)|^2 - 1)} \begin{pmatrix} L^{(2)}_{xx} & L^{(2)}_{xp} \\ L^{(2)}_{xp} & L^{(2)}_{pp} \end{pmatrix}, \tag{4.51}$$

where

$$\begin{aligned} L^{(2)}_{xx} &= 1 + \sigma_{xp}(\tau)^2 - \tau\sigma_{xp}(\tau)\sigma_{pp}(\tau) + \frac{\tau^2}{3}\sigma_{pp}(\tau)^2, \\ L^{(2)}_{xp} &= \sigma_{xx}(\tau)\sigma_{xp}(\tau) - \frac{\tau}{2}\left(1 - \sigma_{xp}(\tau)^2 - \sigma_{xx}(\tau)\sigma_{pp}(\tau)\right) - \frac{\tau^2}{3}\sigma_{xp}(\tau)\sigma_{pp}(\tau), \\ L^{(2)}_{pp} &= \sigma_{xx}(\tau)^2 - \tau\sigma_{xx}(\tau)\sigma_{xp}(\tau) + \frac{\tau^2}{3}\left(1 + \sigma_{pp}(\tau)^2\right). \end{aligned} \tag{4.52}$$

From Eq. (4.51) we then need to find its symplectic diagonalisation in order to identify the necessary squeezing. $L^{(2)}$ is diagonalised by a rotation matrix after which it requires some squeezing $|z|$ to make $L^{(2)}$ proportional to the $\mathbb{1}_{2\times 2}$, this can be achieved with a single complex squeezing z. The magnitude of this squeezing e^{2z} is then given by $e^{2z} = e^{\frac{1}{2}|\ln D_1 - \ln D_2|}$, where D_i are the eigenvalues of $L^{(2)}$ (the symplectic eigenvalue is $\sqrt{D_1 D_2}$).

The eigenvalues of $L^{(2)}$ are

$$\alpha \pm \sqrt{\alpha^2 - \tau^2\left(\sigma_{xx}(\tau) - \tau\sigma_{xp}(\tau) + \frac{\tau^2}{3}\sigma_{pp}(\tau)\right)^2 - \frac{\tau^4}{12}\left(|\sigma(\tau)| - 1\right)^2}, \tag{4.53}$$

with

$$\alpha = \frac{\tau}{2}\left[\left(1 + \frac{\tau^2}{3}\right)\left(1 + \sigma_{xp}(\tau)^2\right) + \sigma_{xx}(\tau)^2 - \sigma_{xp}(\tau)(\sigma_{xx}(\tau) + \sigma_{pp}(\tau))\tau + \frac{\tau^2}{3}\sigma_{pp}(\tau)^2\right]. \tag{4.54}$$

Whence we can calculate the required squeezing to attain the QCRB with phonon counting to be

$$e^{2z} = \sqrt{\frac{1 + \sqrt{1 - \frac{1}{\alpha^2}\left[\tau^2\left(\sigma_{xx}(\tau) - \tau\sigma_{xp}(\tau) + \frac{\tau^2}{3}\sigma_{pp}(\tau)\right)^2 + \frac{\tau^4}{12}\left(|\sigma(\tau)| - 1\right)^2\right]}}{1 - \sqrt{1 - \frac{1}{\alpha^2}\left[\tau^2\left(\sigma_{xx}(\tau) - \tau\sigma_{xp}(\tau) + \frac{\tau^2}{3}\sigma_{pp}(\tau)\right)^2 + \frac{\tau^4}{12}\left(|\sigma(\tau)| - 1\right)^2\right]}}}. \tag{4.55}$$

In the same manner as for homodyne and heterodyne, we can explore the necessary squeezing in the limit that $\nu = 1$ and $r = 0$, which is plotted in Fig. 4.7. Figure 4.7 suggests that negligible squeezing is required for $\tau \lesssim 1$ and so phonon counting alone attains or at least comes close to the QCRB. By contrast for $\tau \gtrsim 1$ the squeezing rapidly becomes demanding and prohibitive.

As the squeezing identified in Eq. (4.55) does not affect the precision of the

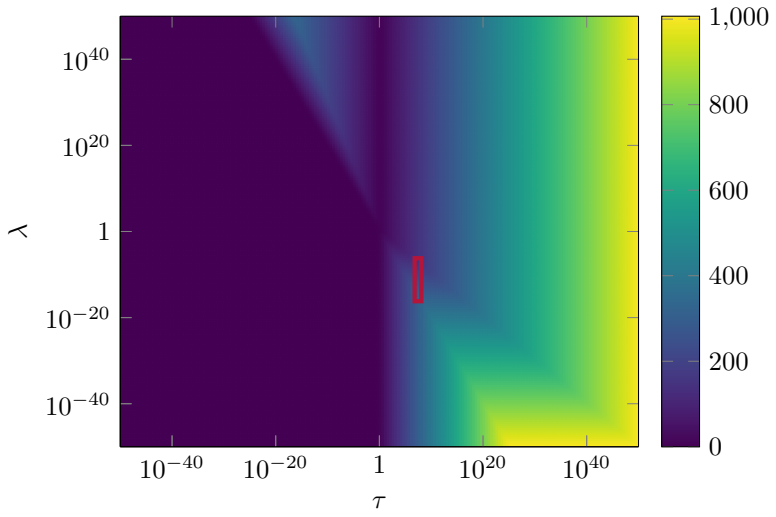

Figure 4.7: Squeezing (in dB) required to enable phonon counting to attain the quantum Cramér-Rao bound. λ and τ are dimensionless quantities defined in Eq. (4.5) and are representative of the collapse rate, and experimental timescale. The red box denotes representative values for MAQRO.

state (i.e. it does not change the QFI of the state, only the FI due to the effective change of measurement) it is not guaranteed that this applying this squeezing and phonon counting is necessarily better than applying the same squeezing to the initial system and utilising an inferior measurement. Furthermore the squeezing magnitude required is parameter-dependent as can be seen from Eq. (4.55) and the squeezing angle may also bear parameter-dependence, requiring an adaptive measurement scheme to be used to gain the full benefits of this squeezed Fock state measurement.

4.6 MAQRO

Finally we turn to the specific MAQRO parameter regime, given by Table 4.1. Figure 4.8 illustrates that the improvements from momentum measurement seen in Eq. (4.38) are present for most of the relevant Λ regime. Similarly we see the order of magnitude improvement in precision can be realised with 10 dB of mechanical squeezing. Moreover the QCRB displays a constant SNR throughout the relevant range $\Lambda \sim 10^{10}$–$10^{20}\,\mathrm{m^{-2}s^{-1}}$. This increased precision over measuring the position can be realised by homodyne measurement along the appropriate quadrature. By contrast to attain the QCRB by phonon counting the necessary squeezing is 79 dB for $\Lambda = 10^{10}\,\mathrm{m^{-2}s^{-1}}$, where the improvement relative to position measurements is many more than 8 orders of magnitude,

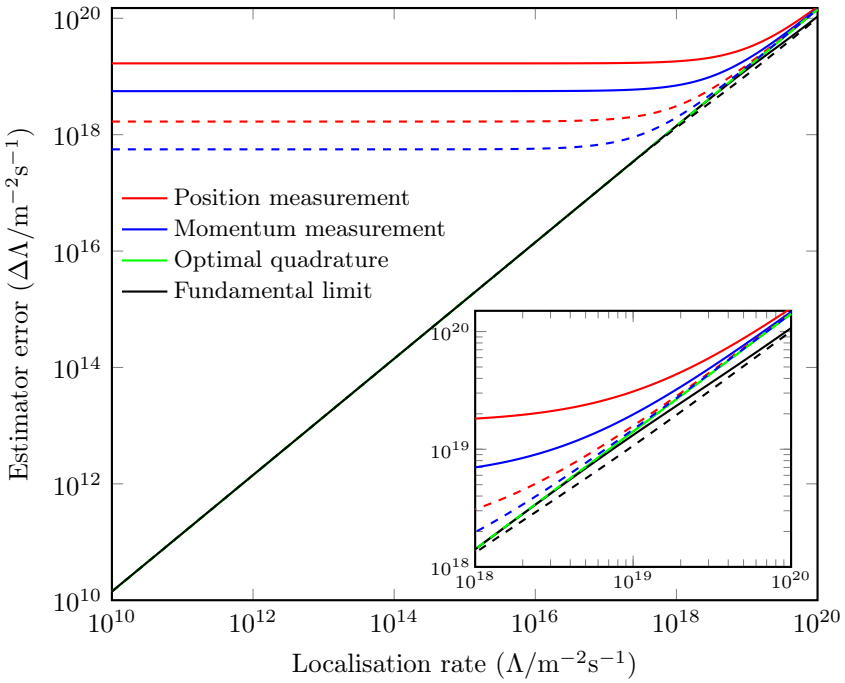

Figure 4.8: Precision of estimating momentum diffusion from wavepacket expansion for MAQRO parameters (Tab. 4.1). Dashed lines denote a squeezing of 10 dB. The optimal and fundamental limit lines overlap until around $\Lambda \sim 10^{20}\,\mathrm{m}^{-2}\mathrm{s}^{-1}$. Three years data collection with $t = 100\,\mathrm{s}$ yields $N \sim 10^6$ repetitions.

which is far beyond existing mechanical squeezings reported [118–120]. This squeezing grows to 158 dB for $\Lambda = 10^{20}\,\mathrm{m}^{-2}\mathrm{s}^{-1}$ where the improvement relative to position measurements becomes a mere factor of 2 in variance.

4.6.1 MAQRO as a test of continuous spontaneous localisation

While Fig. 4.8 demonstrates the potential improvements in absolute precision for estimating the diffusion strength Λ in one case, this does not necessarily translate to a significant increase in scientific results. Among the family of collapse models CSL is the most popularly studied [11, 79] and tested [93–101]. In CSL two quantities determine the macroscopic diffusion rate Λ, representing a characteristic timescale with λ^{CSL} (the single-particle collapse rate) and a characteristic length r_{C} which allows small superpositions to be shielded from the full collapse rate.

For a freely-moving, solid sphere of mass m and radius r_{s} the macroscopic collapse rate Λ is given by [109, 125]

$$\Lambda = \frac{3}{2}\frac{\lambda^{\mathrm{CSL}}}{r_{\mathrm{C}}^2}\left(\frac{m}{m_0}\right)^2\left(\frac{r_{\mathrm{C}}}{r_{\mathrm{s}}}\right)^4\left[1-2\left(\frac{r_{\mathrm{C}}}{r_{\mathrm{s}}}\right)^2+\left(1+2\left(\frac{r_{\mathrm{C}}}{r_{\mathrm{s}}}\right)^2\right)e^{-\left(\frac{r_{\mathrm{s}}}{r_{\mathrm{C}}}\right)^2}\right], \tag{4.56}$$

where m_0 is a reference (nucleon) mass. Equation (4.56) then gives us a way of bounding errors in λ^{CSL} for a given r_{C} from the bounds on $\Delta\Lambda$ using

$$\Delta\lambda^{\mathrm{CSL}} = \frac{2}{3}r_{\mathrm{C}}^2\left(\frac{m_0}{m}\right)^2\left(\frac{r_{\mathrm{s}}}{r_{\mathrm{C}}}\right)^4\left[1-2\left(\frac{r_{\mathrm{C}}}{r_{\mathrm{s}}}\right)^2+\left(1+2\left(\frac{r_{\mathrm{C}}}{r_{\mathrm{s}}}\right)^2\right)e^{-\left(\frac{r_{\mathrm{s}}}{r_{\mathrm{C}}}\right)^2}\right]^{-1}\Delta\Lambda. \tag{4.57}$$

To describe the minimal discernable λ^{CSL} for measurement of a mechanical quadrature we take the limit of the single-shot CRB $\lambda_0^{\mathrm{CSL}} = \lim_{\lambda^{\mathrm{CSL}}\to 0}\Delta\lambda^{\mathrm{CSL}}$ which gives the uncertainty in λ^{CSL} when $\lambda^{\mathrm{CSL}} = 0$ without allowing for repetitions. After M independent repetitions the bound becomes $\Delta\lambda^{\mathrm{CSL}} \geq \sqrt{\frac{1}{M}}\lambda_0^{\mathrm{CSL}}$. For $M \gg 1$ this is approximately the same as when $\lambda^{\mathrm{CSL}} = \lambda_0^{\mathrm{CSL}}/\sqrt{M}$ as at such a value of λ^{CSL}, $\Delta\lambda^{\mathrm{CSL}}$ is bounded as $\Delta\lambda^{\mathrm{CSL}} \geq \sqrt{\frac{1}{\nu}}\left(\sqrt{\frac{1}{\nu}}+1\right)\lambda_0^{\mathrm{CSL}} \approx \sqrt{\frac{1}{\nu}}\lambda_0^{\mathrm{CSL}}$. Allowing for some statistical significance we therefore take $\lambda_{\mathrm{min}}^{\mathrm{CSL}} \sim \frac{2}{\sqrt{\nu}}\lambda_0^{\mathrm{CSL}}$ as the minimum detectable collapse rate.

For a 100 nm radius sphere of mass 5.5×10^9 u with parameters otherwise as Table 4.1 we can evaluate $\lambda_{\mathrm{min}}^{\mathrm{CSL}}$ from Eq. (4.26) for position, momentum, and the θ_{opt} quadratures. We can complement these by plotting a physical lower bound on λ^{CSL} below which CSL would not collapse macroscopic superpositions, which we base on the lower bound introduced by Toroš et al. [79] in which a

graphene disc of radius 0.01 mm localises within 10 ms.

Figure 4.9 shows the resolvable position and momentum bounds, suggesting that crucial ground for $r_C \lesssim 10^{-7}$ m could be covered with the addition of squeezing. Moreover while X-ray data provides a tighter bound for $r_C \lesssim 10^{-8}$ m, the bounds illustrated in Fig. 4.9 would cover valuable ground omitted by previous tests realised to date [95, 97, 98] for $10^{-8}\,\text{m} \lesssim r_C \lesssim 10^{-5}\,\text{m}$ though of course other proposals which are also yet to be implemented would be competitive with our own suggestions of momentum measurement and squeezing [97, 126].

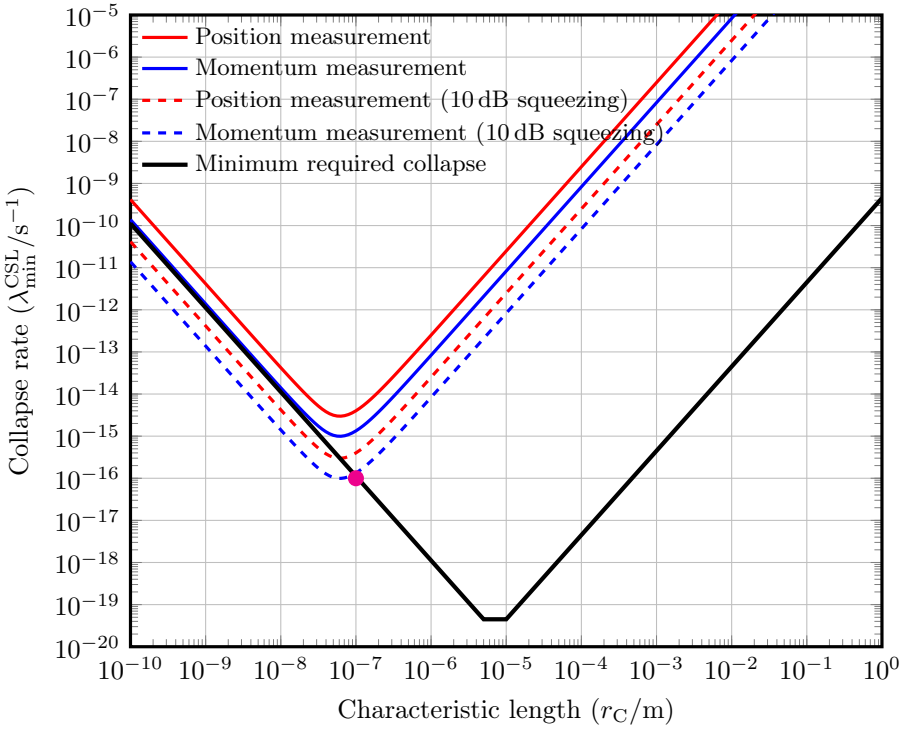

Figure 4.9: Bounds plotted for a $r_s = 100$ nm sphere of mass 5.5×10^9 u with values otherwise as Table 4.1, allowing for 10^6 repetitions. The minimum required collapse rate given is based on the criteria of Toroš et al. [79]. The magenta dot represents the values originally proposed by Ghirardi et al. [81].

Allowing for measurement of the quadrature θ_{opt} has more substantial implications, Fig. 4.10 shows that the potentially-resolvable collapse rate lies well below that of the lower bound considered by Toroš et al. [79]. Weaker constraints on CSL could be considered [127] and modifications to CSL [128] which could nonetheless demand further testing. However it is worth noting that—if a suitable measurement can be realised—the QCRB would theoretically be sensitive to even smaller collapse rates than the optimal quadrature and therefore rule

out a further portion of the range illustrated in Fig. 4.10.

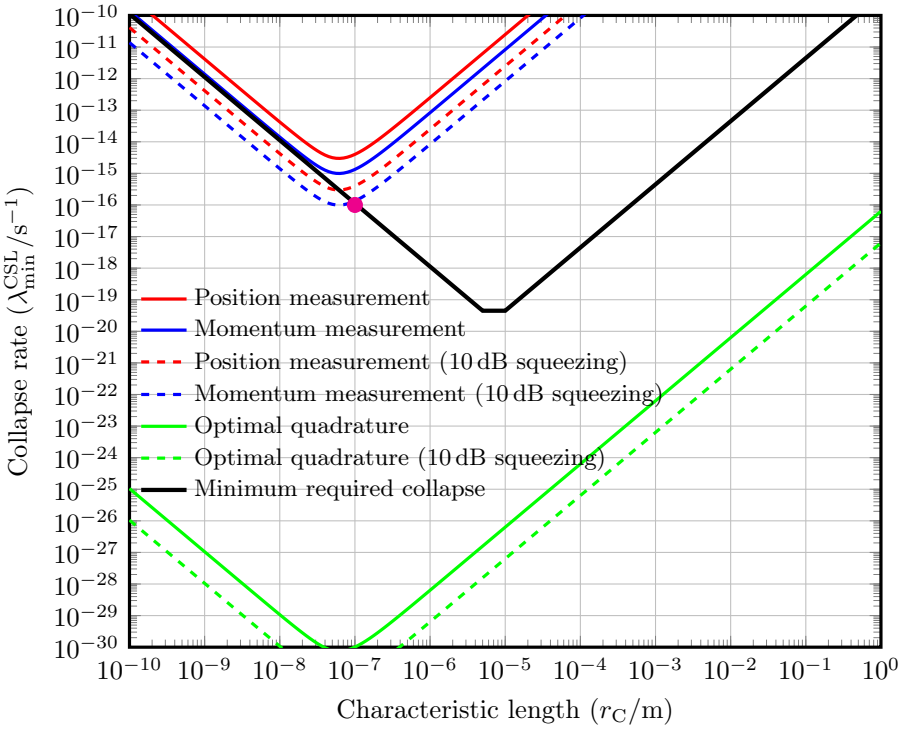

Figure 4.10: Bounds plotted for a $r_{\mathrm{s}} = 100\,\mathrm{nm}$ sphere of mass $5.5 \times 10^9\,\mathrm{u}$ with values otherwise as Table 4.1, allowing for 10^6 repetitions. The minimum required collapse rate given is based on the criteria of Toroš et al. [79]. The magenta dot represents the values originally proposed by Ghirardi et al. [81].

4.7 Conclusions

Our analysis looks specifically at the mechanical system involved and identifies how it can be prepared with appropriate squeezing or cooling, showing in particular a significant improvement in the minimum diffusion rates which can be measured through squeezing. We then explored measurements on the mechanical system and the precision which can be reached through their statistics, showing substantial enhancements exist over observing the final position after a given free expansion.

The measurements considered are in terms of the mechanical mode only, in practice some external (likely optical) field with a given coupling will be required to realise these measurements. Further study into ways to implement these measurements would be desirable to access the full potential shown by the

QCRB and illustrated in Figs. 4.8 to 4.10.

This work could potentially be extended to multi-mode systems, three-dimensional aspects such as rotational degrees of freedom have recently been suggested to offer increased sensitivity [97, 126]. This could also allow for the introduction of multi-parameter aspects; a symmetry-broken diffusion may be expected from other—less fundamental—noise sources.

MAQRO remains an ambitious proposal [109] which has a number of technical issues to overcome [109, 110]. These include the free-fall time, with 100 s likely to be too demanding due to the required pressures [110] which we saw in Eqs. (4.32) and (4.33) can be compensated for by introducing mechanical squeezing. Similarly the proposed cooling to 0.3 phonons falls beyond state-of-the-art which is around 100 phonons [129, 130]. While it is expected that states of fewer phonon may be realised soon [129, 131, 132], Eqs. (4.32) and (4.33) also show that squeezing can compensate for higher energy thermal states, unlike further cooling however squeezing continues to help for $n_{\mathrm{th}} \lesssim 1$ while at this point cooling shows diminishing returns due to the finite uncertainty of the ground state.

Notwithstanding the potential application to MAQRO, which we have focused on, our general analysis may prove valuable to other experiments. For example in smaller table-top setups [133, 134] while τ may be reduced leading to a lesser sensitivity from quadrature measurements, higher precisions could be achieved by reaching the QCRB through phonon counting alone (see Fig. 4.7).

Chapter 5

Optomechanical displacement estimation

Estimating miniscule displacements is central to a range of physical problems from microscopy for probing biological systems, vibrations in the earth for seismology, and the detection of gravitational waves. Optical interferometry affords some of the most precise methods to resolve these displacements [9, 22, 135].

Advanced LIGO [21] has achieved extraordinary precision in order to claim the first direct detection of GWs [136]. With the addition of the Virgo detector [137] a neutron star merger was observed [138], the origin of which was sufficiently localised for optical observations to complement the GW detection [139].

These detections were achieved by reaching displacement sensitivities of $\sim 10^{-24}\,\sqrt{\text{Hz}}^{-1}$ [21, 140]. Across the GW frequencies 10^1–10^4 Hz at which these detectors operate the primary noise is quantum in origin. This standard quantum limit consists of the effects of both shot noise (dominating at high frequencies) and radiation-pressure noise (dominating at low frequencies). Such radiation-pressure noise plays a role in a wide range of optomechanical systems [141–143].

Quantum-mechanical effects can also be used to offer potential improvements both in terms of input states and measurements. Inputting squeezed light can improve the precision of such devices [3, 6, 121, 144, 145] which has been demonstrated in both the GEO 600 [146, 147] and LIGO [148] detectors. Back-action evading measurements, which remove the radiation-pressure noise, have been developed for GW detectors [121, 140, 149] although optical loss can prevent these measurements from reducing to the SNL [DB3, 121]. This is supported by a wider effort to develop back-action evading measurements [150–152] which pervade a range of similar devices.

The SNL of a Mach-Zehnder interferometer has been well-studied in terms of the fundamental limits [30, 144] and radiation-pressure effects have been considered for laser-interferometric GW interferometers [12, 121, 140]. However the role of radiation-pressure in the fundamental limits has only recently attracted interest [122].

When the same interferometers are driven with multiple carrier frequencies the radiation pressure derives from the interaction of each carrier mode with a single mechanical mode [140]. This interaction gives rise to a multi-mode squeezing [153].

This has potential advantages when applied in interferometers for control purposes [154, 155]. Introducing a second carrier, which does not enter the arm cavities, can reduce the backaction effects in the main carrier [140, 156]. In combination with the signal-recycling mirror [157–159] which uses the optical spring effect to enhance sensitivity [158], multiple carriers can both stabilise instabilities found in the single-mode optical spring and enable the sensitivity curves to be shaped through control of power and detunings [160, 161].

In this chapter results first published as Branford et al. [DB3] are presented which demonstrate the fundamental limits of an optomechanical interferometer driven with an arbitrary number of modes of arbitrary optical powers. This analysis extends to the role of both optical loss and externally input squeezing.

5.1 Sensor model

We will consider, for reference, an interferometer as illustrated in Fig. 5.1. This chapter applies generally to all systems with input-output relations following Eq. (5.4) however the exact context of these results may vary in different optomechanical systems. Coherent laser light at frequencies ω_j with intensities I_j is input to one arm of the interferometer, while vacuum or squeezed vacuum is input to the other arm. Light of each frequency then disturbs the motion of the mirrors and the mirrors in turn cause coupling between the different carrier modes.

Parameter	Symbol	Value
Optical power	I	$840\,\mathrm{kW}$
Test mass	m	$40\,\mathrm{kg}$
Arm cavity length	L	$4\,\mathrm{km}$
Arm cavity half-bandwidth	γ	$2\pi \times 500\,\mathrm{s}^{-1}$
Carrier frequency	ω	$2\pi \times 2.82 \times 10^{14}\,\mathrm{s}^{-1}$

Table 5.1: Representative parameter values for Advanced LIGO [21, 149]

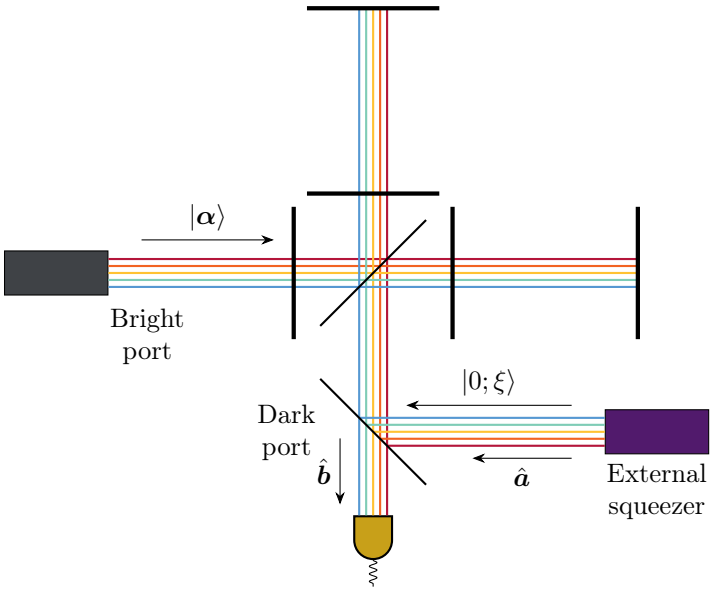

Figure 5.1: A multi-carrier interferometer with external squeezing

5.1.1 Two-photon formalism

Before moving to the mathematical description we briefly motivate the two-photon formalism [162, 163] in which input-output relations are typically phrased.

Light reflected from a mirror displaced at x from an equilibrium point acquires an additional phase $2\omega_0 x/c$. For a mirror moving at a constant frequency $x(t) = x_0 \cos \Omega t$ (such that its motion is unaffected by the reflected light). The resultant field is then of form $E_0(t)e^{ix_0 \cos \Omega t}$, which for $x_0 \ll 1$ can be approximated as [149]

$$E(t) = \epsilon \left[e^{i\omega_0 t} + i\frac{x_0}{2} \left(e^{i(\omega_0+\Omega)t} + e^{i(\omega_0-\Omega)t} \right) \right], \tag{5.1}$$

which introduces light in the sideband frequencies $\omega_0 \pm \Omega$ from what was originally monochromatic light. It is the light at these frequencies $\omega_0 \pm \Omega$ which, if detectable, provides a method to detect that the mirror was moving at a frequency Ω.

In such low-power regimes the system can easily be modelled as linear, with photons being converted from frequency ω_0 to one of the sidebands. Here one can easily model the interferometer and recreate the shot-noise limit with a linear system as done in Demkowicz-Dobrzański et al. [144] for the GEO 600 GW detector. However at higher optical powers, radiation-pressure disturbs the mirrors motion and the simple model no longer holds.

Instead the sideband modes become entangled or squeezed and so the simple picture where the $\omega_0 + \Omega$ and $\omega_0 - \Omega$ modes can be treated separately as the picture

of two one-mode states is no longer relevant [121, 149, 162, 164]. With single-mode squeezing the creation operator is transformed into a combination of the creation and annihilation operators as $\hat{S}^\dagger(\xi)\hat{a}\hat{S}(\xi) = \cosh|\xi|\hat{a} + e^{i\arg\xi}\sinh|\xi|\hat{a}^\dagger$, while two mode squeezing yields $\hat{S}_2^\dagger(\xi)\hat{a}\hat{S}_2(\xi) = \cosh|\xi|\hat{a} + e^{i\arg\xi}\sinh|\xi|\hat{b}^\dagger$ [58]. With two-mode queezing one can work with the larger two-mode picture, describing the evolution of the operators $\{\hat{a}_{\omega+\Omega}, \hat{a}^\dagger_{\omega+\Omega}, \hat{a}_{\omega-\Omega}, \hat{a}^\dagger_{\omega-\Omega}\}$ within the same domain. The two-photon formalism [162, 163] with the operators

$$\hat{a}_1^{(\omega)}(\Omega) = \frac{\hat{a}_{\omega+\Omega} + \hat{a}^\dagger_{\omega-\Omega}}{\sqrt{2}}, \text{ and } \hat{a}_2^{(\omega)}(\Omega) = \frac{\hat{a}_{\omega+\Omega} - \hat{a}^\dagger_{\omega-\Omega}}{i\sqrt{2}}, \tag{5.2}$$

is frequently utilised instead [121, 164], where these operators generally prove a more natural basis to describe optomechanical systems [121, 140, 149, 157–159, 164] as the action of $\hat{a}_{1,2}$ on a system introduces correlations between the $\omega + \Omega$ and $\omega - \Omega$ modes.

5.1.2 Input-output relations

The input dark modes are transformed into the outgoing fields by a linear input-output relation of the form

$$\hat{\boldsymbol{b}}(\Omega) = \mathcal{M}(\Omega)\hat{\boldsymbol{a}}(\Omega) + h(\Omega)\boldsymbol{\mathcal{V}}(\Omega), \tag{5.3}$$

where $\mathcal{M}(\Omega)$ is a complex matrix describing a Bogoliubov transformation between the incoming and outgoing fields, and $h(\Omega)\boldsymbol{\mathcal{V}}(\Omega)$ is a displacement vector, where Ω is the frequency of the mechanical mode.

Input-output relations of this form are typically given in terms of the two-photon operators [162, 163] given in Eq. (5.2), rather than in terms of the annihilation/creation operators for the frequency mode operators[1]. With d carrier modes we introduce d pairs of such operators $\{\hat{a}_1^{(1)}, \cdots, \hat{a}_1^{(d)}, \hat{a}_2^{(1)}, \cdots, \hat{a}_2^{(d)}\}$, where the (j) superscript denotes the frequency mode ω_j.

The family of sensors of interest to us are concerned with estimating the displacement $h(\Omega)$, with $\mathcal{M}$ and $\mathcal{V}$ consisting of the 2×2 and 2×1 blocks [140, 160]

$$\mathcal{M}_{jk} = e^{i(\beta_j+\beta_k)}\begin{pmatrix} \delta_{jk} & 0 \\ -\chi\sqrt{\kappa_j\kappa_k} & \delta_{jk} \end{pmatrix}, \quad \mathcal{V}_j = \frac{e^{i\beta_j}}{h_{\mathrm{SQL}}}\begin{pmatrix} 0 \\ \chi\sqrt{2\kappa_j} \end{pmatrix}, \tag{5.4}$$

where δ_{ij} is the Kronecker delta, κ_j is a positive variable (e.g. proportional to

[1] In Section 5.1.5 we essentially undo this translation and revert to writing the full state out in terms of the frequency-mode operators using quadrature operators derived from the two-photon operators which we see are a linear transformation of the quadratures of the frequency-mode operators.

the intensity as in Eq. (5.8)), β_j a phase shift, h_{SQL} a proportionality constant of sensitivity, and $\chi = \pm 1$. Specific forms for these parameters for the tuned interferometer (e.g. Fig. 5.1) are given in Section 5.1.3.

In the case of the interferometer illustrated in Fig. 5.1, κ_j is proportional to the intensity of light in each mode (this is derived for a simple interferometer is Section 5.1.3) while χ represents the sign of the mechanical response which is discussed in more detail in Section 5.1.8.

The diagonal terms in $\mathcal{M}$ merely correspond to light entering the interferometer being reflected, while it is the off-diagonal $\sqrt{\kappa_j \kappa_k}$ terms which advance this from a simpler setup equivalent to d non-interacting interferometers. The off-diagonal terms correspond to a multi-mode squeezing, with light from the j-th mode driving motion of the mirror whose motion then induces a squeezing in the k-th mode and vice versa to induce a highly multi-mode squeezing across all the carrier modes.

5.1.3 Derivation for the tuned interferometer

The form of the input-output relations given in Eq. (5.4)—in particular the off-diagonal $\sqrt{\kappa_j \kappa_k}$ terms—can be readily derived by considering the tuned Michelson interferometer in the manner of Miao and Chen [165]. To first-order in the test mass displacements $\hat{x}_A$ and $\hat{x}_B$ cause the input optical fields $\hat{a}_{1,2}^{(j)}$ to transform to the output optical fields $\hat{b}_{1,2}^{(j)}$ as

$$\begin{aligned} \hat{b}_1^{(j)}(t) &= \hat{a}_1^{(j)}(t - 2L/c), \\ \hat{b}_2^{(j)}(t) &= \hat{a}_2^{(j)}(t - 2L/c) + \sqrt{\frac{2I_j}{\hbar\omega_j}} \frac{\omega_j}{c} \hat{x}_d(t - L/c), \end{aligned} \tag{5.5}$$

where $\hat{x}_d = \hat{x}_A - \hat{x}_B$. The differential mode of the mirrors motion is driven by the light entering the bright port and the GW tidal force—caused by a wave with signal $h(t)$—which has an equation of motion

$$m \frac{\partial^2}{\partial t^2} \hat{x}_d(t) = \sum_j 4 \sqrt{\frac{2\hbar\omega_j I_j}{c^2}} \hat{a}_1^{(j)}(t - \tau) + mL \frac{\partial^2}{\partial t^2} h(t). \tag{5.6}$$

Equations (5.5) and (5.6) can be solved most easily in the frequency domain, where Eq. (5.5) becomes

$$\begin{aligned} \hat{b}_1^{(j)}(\Omega) &= e^{2i\Omega\tau} \hat{a}_1^{(j)}(\Omega), \\ \hat{b}_2^{(j)}(\Omega) &= e^{2i\Omega\tau} \hat{a}_2^{(j)}(\Omega) - \frac{e^{i\Omega\tau}}{m\Omega^2} \sqrt{\frac{2I_j}{\hbar\omega_j}} \frac{\omega_j}{c} \left[\sum_i 4 e^{i\Omega\tau} \sqrt{\frac{2\hbar\omega_i I_i}{c^2}} \hat{a}_1^{(i)}(\Omega) - mL\Omega^2 h(\Omega) \right], \end{aligned} \tag{5.7}$$

which we can recognise as giving us the form of Eq. (5.4) with

$$\chi = 1, \quad \kappa_j = \frac{2\sqrt{2}I_j\omega_j}{mc^2\Omega^2}, \quad \beta_j = \Omega\tau, \quad h_{\mathrm{SQL}} = \sqrt{\frac{4\hbar}{mL^2\Omega^2}}. \tag{5.8}$$

5.1.4 Interferometer modifications

The input-output operations described in Eq. (5.4) are not limited in scope to the simple description of the tuned interferometer for which they are derived in Section 5.1.3 but hold for a wider set of sensors. Two of the major interferometer modifications proposed in current literature are the signal-recycling mirror [140, 157–159] and the quantum speed meter [140, 149, 166]. Both modifications can be captured to some extent through the same relations in Eq. (5.4) with appropriate redefinition of κ_j and χ relative to Eq. (5.8).

The quantum speed meter has the same form as Eq. (5.4) [140, 149, 166] and results given here can be applied directly with only the appropriate definitions of β_j, χ, κ_j, and h_{SQL}. The signal-recycling mirror however induces more complicated input-output relations [157–159], however at low frequencies where the radiation-pressure dominates Eq. (5.4) can be used as a suitable approximation for the evolution of the light [167].

5.1.5 Gaussian state description

The two-photon operators

$$\hat{a}_1^{(j)} = \frac{\hat{a}_{\omega_j+\Omega} + \hat{a}^\dagger_{\omega_j-\Omega}}{\sqrt{2}}, \quad \hat{a}_2^{(j)} = \frac{\hat{a}_{\omega_j+\Omega} - \hat{a}^\dagger_{\omega_j-\Omega}}{i\sqrt{2}}, \tag{5.9}$$

are not themselves Hermitian observables, instead we can construct position and momentum quadrature operators for the optical fields

$$\begin{aligned}
\hat{x}_1^{(j)} &= \frac{\hat{a}_1^{(j)} + (\hat{a}_1^{(j)})^\dagger}{\sqrt{2}} = \frac{\hat{a}_{+(j)} + \hat{a}^\dagger_{-(j)} + \hat{a}^\dagger_{+(j)} + \hat{a}_{-(j)}}{2} = \frac{\hat{x}_{+(j)} + \hat{x}_{-(j)}}{\sqrt{2}}, \\
\hat{x}_2^{(j)} &= \frac{\hat{a}_2^{(j)} + (\hat{a}_2^{(j)})^\dagger}{\sqrt{2}} = \frac{\hat{a}_{+(j)} - \hat{a}^\dagger_{-(j)} - \hat{a}^\dagger_{+(j)} + \hat{a}_{-(j)}}{2i} = \frac{\hat{p}_{+(j)} + \hat{p}_{-(j)}}{\sqrt{2}}, \\
\hat{p}_1^{(j)} &= \frac{\hat{a}_1^{(j)} - (\hat{a}_1^{(j)})^\dagger}{i\sqrt{2}} = \frac{\hat{a}_{+(j)} + \hat{a}^\dagger_{-(j)} - \hat{a}^\dagger_{+(j)} - \hat{a}_{-(j)}}{2i} = \frac{\hat{p}_{+(j)} - \hat{p}_{-(j)}}{\sqrt{2}}, \\
\hat{p}_2^{(j)} &= \frac{\hat{a}_2^{(j)} - (\hat{a}_2^{(j)})^\dagger}{i\sqrt{2}} = \frac{-\hat{a}_{+(j)} + \hat{a}^\dagger_{-(j)} - \hat{a}^\dagger_{+(j)} + \hat{a}_{-(j)}}{2} = \frac{-\hat{x}_{+(j)} + \hat{x}_{-(j)}}{\sqrt{2}},
\end{aligned} \tag{5.10}$$

where $\hat{a}_{\pm(j)}$ is adopted as shorthand for $\hat{a}_{\omega_j\pm\Omega}$.

These $\{\hat{x}_{+(j)}, \hat{x}_{-(j)}, \hat{p}_{+(j)}, \hat{p}_{-(j)}\}$ operators are then obtainable by an orthogonal transformation of the quadrature operators of the individual modes. To

construct the Gaussian state from the input-output operations Eq. (5.4) we will use these $\hat{x}_{\pm(j)}$ and $\hat{p}_{\pm(j)}$ operators as the basis of our phase space and therefore (in contrast to definitions in Chapter 3) we have the quadrature operator vector of length $4d$

$$\hat{\boldsymbol{R}} = \begin{pmatrix} \hat{x}_1^{(1)} & \hat{x}_2^{(1)} & \hat{x}_1^{(2)} & \cdots & \hat{p}_1^{(1)} & \hat{p}_2^{(1)} & \cdots & \hat{p}_2^{(d)} \end{pmatrix}, \tag{5.11}$$

and our non-zero commutators are

$$[\hat{x}_1^{(j)}(\Omega_A), \hat{x}_2^{(k)}(\Omega_B)] = [\hat{p}_1^{(j)}(\Omega_A), \hat{p}_2^{(k)}(\Omega_B)] = i\delta_{jk}\delta(\Omega_A - \Omega_B). \tag{5.12}$$

In contrast to the usual description the position and momentum operators of these two-photon operators commute as $[\hat{x}_m^{(j)}(\Omega_A), \hat{p}_n^{(k)}(\Omega_B)] = 0$. Instead it is the $\hat{x}_1^{(j)}$ and $\hat{x}_2^{(j)}$ ($\hat{p}_1^{(j)}$ and $\hat{p}_2^{(j)}$) pairs which have non-zero commuatators.

The input-output relations of Eq. (5.4) can be broken down into form

$$\hat{\boldsymbol{b}} = BMB\hat{\boldsymbol{a}} + hB\boldsymbol{V}, \tag{5.13}$$

with $M \in \mathbb{R}^{2d\times 2d}$, $\boldsymbol{V} \in \mathbb{R}^{2d}$, and $B = \mathrm{diag}(e^{i\beta_1}, e^{i\beta_1}, e^{i\beta_2}, e^{i\beta_2}, \cdots, e^{i\beta_d}, e^{i\beta_d})$. For an initial covariance matrix with form $\sigma = \sigma_0 \oplus \sigma_0$ the evolved state is then given by

$$\begin{aligned} \boldsymbol{d} &= \sqrt{2}\mathcal{S}_B \begin{pmatrix} \Re[h]\boldsymbol{V} \\ \Im[h]\boldsymbol{V} \end{pmatrix}, \\ \sigma &= \mathcal{S}_B \begin{pmatrix} M(\Re[B]\sigma_0\Re[B] + \Im[B]\sigma_0\Im[B])M^T & 0 \\ 0 & M(\Re[B]\sigma_0\Re[B] + \Im[B]\sigma_0\Im[B])M^T \end{pmatrix} \mathcal{S}_B^T, \end{aligned} \tag{5.14}$$

where $\mathcal{S}_B$ is the symplectic form of the unitary B according to Eq. (3.38).

5.1.6 Loss model

Optical loss—in the form of light leaking into a loss mode and being replaced with vacuum (or even thermal states)—can be modelled by mixing the outgoing modes $\hat{\boldsymbol{b}}$ with a family of loss (unmeasurable) modes $\hat{\boldsymbol{n}}'$ at a beam splitter with transmittivity η according to $\hat{\boldsymbol{b}} \to \sqrt{\eta}\hat{\boldsymbol{c}} + \sqrt{1-\eta}\hat{\boldsymbol{n}}$,. The final loss modes $\hat{\boldsymbol{n}}$—which will contain some of the signal—are considered inaccessible to the measurement. These modes can be traced out under a partial trace to reflect the state in the $\hat{\boldsymbol{c}}$ modes averaged over the possible state of the $\hat{\boldsymbol{n}}$ modes [14]. For a Gaussian system the moments of the reduced state are simply given by the submatrices of the full moments consisting only of modes which are associated with the modes of the reduced system [52, 53].

The moments therefore evolve as

$$\boldsymbol{d} \to \sqrt{\eta}\boldsymbol{d}, \quad \sigma \to \eta\sigma + (1-\eta)\sigma_{\text{Loss}}, \tag{5.15}$$

where σ_{Loss} will for this chapter be considered as pure vacuum $\sigma_{\text{Loss}} = \mathbb{1}$ although—as long as it is Gaussian—other covariance matrices are possible with thermal states also likely to be of interest.

5.1.7 Input squeezing

Through the use of externally squeezed light incident on the dark port the precision of such sensors can be improved [3, 121, 146], a feat which has already been demonstrated in current GW detectors [146–148]. With multi-mode systems one feasible generalisation is the introduction of parallel squeezing for the sidebands of each carrier frequency, each with an indepdent squeezing $\xi_j = r_j e^{i\phi_j}$ in the $\hat{x}_1^{(j)}$ and $\hat{x}_2^{(k)}$ modes[2]. Thus the input covariance matrix for this set of squeezings $\{\xi_j\}$ is

$$\sigma_0 = \bigoplus_{i=1}^{d} \begin{pmatrix} \cosh 2r_i + \sinh 2r_i \cos 2\phi_i & \sinh 2r_i \sin 2\phi_i \\ \sinh 2r_i \sin 2\phi_i & \cosh 2r_i - \sinh 2r_i \cos 2\phi_i \end{pmatrix}. \tag{5.16}$$

5.1.8 Negative responses

The signal-recycling mirror, at sufficiently low frequencies, has a negative response which necessitates the χ included in Eq. (5.4). Such a phenomenon is even seen in the tuned interferometer due to the pendulumn behaviour of the free mass [165], however this is usually around $\Omega_p \sim 1\,\text{Hz}$ [21] and therefore is below the GW frequency range of interest. This is also necessary in approximating the detuned interferometer introduced in Section 5.1.4 where the resonance occurs closer to relevant frequencies.

The negative response $\chi = -1$ can be simulated on the normal interferometer by a phase shift $U_D = \begin{pmatrix} 1 & 0 \\ 0 & -1 \end{pmatrix}$ prepending a system satisfying $\chi = 1$. This could be achieved by optical elements placed before the sensor (and therefore also acting on the output) and so we can model all sensors as evolving under

$$\mathcal{M}_{jk} = e^{i(\beta_j+\beta_k)} \begin{pmatrix} \delta_{jk} & 0 \\ -\sqrt{\kappa_j\kappa_k} & \delta_{jk} \end{pmatrix}, \quad \mathcal{V}_j = \frac{e^{i\beta_j}}{h_{\text{SQL}}} \begin{pmatrix} 0 \\ \sqrt{2\kappa_j} \end{pmatrix}, \tag{5.17}$$

prepended by U_D. We can then recognise that U_D maps a single-mode squeezed

[2] As we argue later the $\hat{\boldsymbol{p}}$ modes are dropped we omit squeezing of those modes, however in general a second set of squeezings of those modes could be considered

state as

$$\begin{aligned}\mathcal{S}_D \begin{pmatrix} \cosh 2r + \sinh 2r \cos 2\phi & \sinh 2r \sin 2\phi \\ \sinh 2r \sin 2\phi & \cosh 2r - \sinh 2r \cos 2\phi \end{pmatrix} \mathcal{S}_D^T \\ = \begin{pmatrix} \cosh 2r + \sinh 2r \cos 2\phi & -\sinh 2r \sin 2\phi \\ -\sinh 2r \sin 2\phi & \cosh 2r - \sinh 2r \cos 2\phi \end{pmatrix},\end{aligned} \tag{5.18}$$

and so a squeezing angle ϕ with the $\chi = -1$ sensor is equivalent to the squeezing angle $-\phi$ with the $\chi = 1$ sensor. Similarly homodyne angles—which we introduce in Section 5.2.2—are transformed by U_D and the homodyne angle θ with the $\chi = -1$ sensor is equivalent to the homodyne angle $-\theta$ with the $\chi = 1$ sensor. Given these simple translations we will henceforth consider only $\chi = 1$.

5.2 Displacement estimation

The case of displacement estimation is a special case of parameter estimation in Gaussian states where $\partial_j \sigma = 0$. This allows certain simplifications from the more general problem of parameter estimation in Gaussian states considered in Section 3.4.

In this chapter we are concerned with the detection of signals $h(t)$—or more precisely $h(\Omega)$. The frequency amplitudes $h(\Omega)$ are complex quantities satisfying $h(\Omega) = h(-\Omega)^*$ being the Fourier transform of a real signal $h(t)$. The primary quantity of interest is the sensitivity to the gravitational field $|h(\Omega)|$ with the phase encoding the offset between different frequency modes in the time domain.

5.2.1 Fundamental limits

With parameters encoded only the first term in Eq. (3.78) is required and so the QFI matrix we are concerned with is

$$H_{jk} = 2\partial_j \boldsymbol{d}^T \sigma^{-1} \partial_k \boldsymbol{d}. \tag{5.19}$$

Moreover for this chapter we are interested only in the estimation of a single parameter which gives us a scalar QFI [54, 56, 64]

$$H = 2\partial \boldsymbol{d}^T \sigma^{-1} \partial \boldsymbol{d}. \tag{5.20}$$

Evaluating the QFI for the Gaussian state described by Eq. (5.14) we can write the state as

$$\boldsymbol{d} = \sqrt{2}\mathcal{S}_B \begin{pmatrix} \Re[h]\boldsymbol{V} \\ \Im[h]\boldsymbol{V} \end{pmatrix}, \quad \sigma = \mathcal{S}_B \begin{pmatrix} \sigma_0 & 0 \\ 0 & \sigma_0 \end{pmatrix} \mathcal{S}_B^T, \tag{5.21}$$

due to $\mathcal{S}_B\mathcal{S}_B^T = \mathbb{1}$ the QFI reduces to

$$H(|h|) = 4\left[(\partial_{|h|}\Re h)^2 + (\partial_{|h|}\Im h)^2\right]\boldsymbol{V}^T\sigma_0^{-1}\boldsymbol{V}, \tag{5.22}$$

noting that $\Re h = |h|\cos(\arg h)$ and $\Im h = |h|\sin(\arg h)$ we have

$$H(|h|) = 4\boldsymbol{V}^T\sigma_0^{-1}\boldsymbol{V}. \tag{5.23}$$

The QCRB is therefore independent of the argument of the GW frequency amplitudes $\arg h$.

This result extends to the case where the state is mixed with a multi-mode thermal state [DB3] which is the case for the loss model we consider in Section 5.1.6.

Henceforth we will consider the parameter to be real and omit the $\hat{\boldsymbol{p}}$ modes for simplicity. As such we require

$$M_{jk} = \begin{pmatrix} \delta_{jk} & 0 \\ -\sqrt{\kappa_j\kappa_k} & \delta_{jk} \end{pmatrix}, \quad V_j = \frac{1}{h_{\mathrm{SQL}}}\begin{pmatrix} 0 \\ \sqrt{2\kappa_j} \end{pmatrix}, \tag{5.24}$$

to evolve the moments through the interferometer.

5.2.2 Homodyne limits

The statistics of homodyne detection can be extracted in the manner of Section 3.4.3. We will consider homodyne detection local to each carrier mode such that a rotation θ_j between the $\hat{x}_j^{(1)}$ and $\hat{x}_j^{(2)}$ modes

$$\mathcal{S}_{\mathrm{Hom.}}(\boldsymbol{\theta}) = \begin{pmatrix} \cos\theta_1 & -\sin\theta_1 & \cdots & 0 & 0 \\ \sin\theta_1 & \cos\theta_1 & \cdots & 0 & 0 \\ \vdots & \vdots & \ddots & \vdots & \vdots \\ 0 & 0 & \cdots & \cos\theta_d & -\sin\theta_d \\ 0 & 0 & \cdots & \sin\theta_d & \cos\theta_d \end{pmatrix}, \tag{5.25}$$

followed by measurement of the $\{\hat{x}_2^{(j)}\}$ quadratures. The probability distributions which result from these measurements on a Gaussian state are then Gaussian with moments $\boldsymbol{w}$ and Σ from which the FI can be evaluated with Eq. (2.18).

5.2.3 Attainability of the fundamental limits through homodyne detection

For the purposes of this section we revert to the standard and abstract $\{\hat{x}_j, \hat{p}_j\}$ operators of an arbitrary Gaussian state.

The SLD in the case of displacement estimation—with $\partial_\phi \sigma = 0$—is

$$\mathcal{L}_{\boldsymbol{d}_\phi} = 2\frac{\partial \boldsymbol{d}_{\boldsymbol{\phi}}^T}{\partial \phi}\sigma^{-1}(\boldsymbol{R} - \boldsymbol{d}_{\boldsymbol{\phi}}), \tag{5.26}$$

as each quadrature operator acts only on a single mode we can rewrite the SLD to explicitly recognise the mode upon which each operator acts. As such the SLD operator has form

$$\mathcal{L}_{\boldsymbol{d}_\phi} = \sum_{j=1}^{d} \mathbb{1}^{\otimes(j-1)} \otimes (l_1^{(x)}\hat{x}_j + l_j^{(p)}\hat{p}_j) \otimes \mathbb{1}^{\otimes(d-j)} \tag{5.27}$$

from which we can conclude that the optimal basis to measure in is separable between the modes. Therefore the local homodyne measurements we will apply in Section 5.4 will—on sufficient optimisation over the local homodyne angles—be sufficient to saturate the QCRB for all of the cases considered in this chapter.

In the case of a displacement parameter $\boldsymbol{d}_\phi = \phi \boldsymbol{d}_1 + \boldsymbol{d}_2$ where $\partial_\phi \boldsymbol{d}_1 = \partial_\phi \boldsymbol{d}_2 = 0$ the SLD operator is parameter-independent excepting the constant in the coefficient of the $\mathbb{1}^{\otimes d}$ term. As any valid basis is an eigenbasis of the identity the necessary homodyne angles will be parameter-independent. This is the case for the displacement given by Eq. (5.39) which we focus on in this chapter.

5.2.4 Relation to spectral noise densities

In studies of optomechanical systems the precision is often expressed in terms of spectral noise densities (SNDs) [116, 121, 140]. We review how the SND can be related to the CRB for frequency amplitudes which this chapter focuses on.

A signal $h(t)$ which is encoded within a measured signal $y(t) = h(t) + w(t)$ is limited by the unknown component $w(t)$. This sensitivity can be described by the single-sided SND [168, 169]

$$S(\Omega) = 2\int_{-\infty}^{\infty} \mathrm{d}\tau\, C_w(\tau)\cos(\Omega\tau), \tag{5.28}$$

where $C_w(\tau)$ is the autocorrelation function

$$C_w(\tau) = \lim_{T\to\infty} \frac{1}{2T}\int_{-T}^{T} \mathrm{d}t\, [w(t) - \bar{w}][w(t+\tau) - \bar{w}], \tag{5.29}$$

where $\bar{w}$ is the time-average of w. When $w(t)$ is a white Gaussian noise process

satisfying $C_w(\tau) = \upsilon\delta(\tau)$, this is simply

$$S(\Omega) = 2\upsilon. \tag{5.30}$$

Considering the same signal $y(t) = h(t) + w(t)$ the precision of an estimator $\widetilde{g}$ of a parameter of the signal $h(t)$ is [33]

$$(\Delta g)^2 \geq \frac{\upsilon}{\mathbb{E}\left[\left(\frac{\partial h(t)}{\partial g}\right)^2\right]}. \tag{5.31}$$

In this case the parameters of interest which match the SND of the signal described above are the amplitudes of the frequency modes $|h(\Omega)|$. The dependence of $h(t)$ on the frequency amplitudes $|h(\Omega)|$ is then

$$\begin{aligned}\frac{\partial h(t)}{\partial |h(\Omega)|} &= \frac{\partial}{\partial |h(\Omega)|}\int_{-\infty}^{\infty} \mathrm{d}\Omega'\, h(\Omega')e^{i\Omega' t} \\ &= \int_{-\infty}^{\infty} \mathrm{d}\Omega' \left[\delta(\Omega-\Omega')e^{i\arg(h(\Omega'))} + \delta(\Omega+\Omega')e^{i\arg(h(\Omega'))}\right] e^{i\Omega' t} \\ &= 2\cos\left[\Omega t + \arg(h(\Omega))\right],\end{aligned} \tag{5.32}$$

where the Ω' and $-\Omega'$ frequencies both appear as $h(-\Omega) = h(\Omega)^*$. The expectation of the square of $(\partial_{|h(\Omega)|}h(t))^2$ is then simply 2 giving a CRB of

$$(\Delta|h(\Omega)|)^2 \geq \frac{\upsilon}{2}, \tag{5.33}$$

yielding a proportionality constant of 4 between these two methods of calculating sensitivities given by Eqs. (5.30) and (5.33).

5.3 Fundamental limits

5.3.1 Quantum state

We now combine the elements of Section 5.1 to evaluate the full state of interest. Evolving the—potentially squeezed—input covariance matrix Eq. (5.16) through

the interferometer according to Eq. (5.24) the covariance matrix becomes

$$\sigma_{jk} = \delta_{jk} \begin{pmatrix} \cosh 2r_j + \sinh 2r_j \cos 2\phi_j & \sinh 2r_j \sin 2\phi_j \\ \sinh 2r_j \sin 2\phi_j & \cosh 2r_j - \sinh 2r_j \cos 2\phi_j \end{pmatrix} - \sqrt{\kappa_j \kappa_k} \begin{pmatrix} 0 & \cosh 2r_j + \sinh 2r_j \cos 2\phi_j \\ \cosh 2r_k + \sinh 2r_k \cos 2\phi_k & \sinh 2r_j \sin 2\phi_j + \sinh 2r_k \sin 2\phi_k - K_{\mathrm{Tot}} \end{pmatrix}, \tag{5.34}$$

where

$$K_{\mathrm{Tot}} = \sum_{j=1}^{d} \kappa_j \left(\cosh 2r_j + \sinh 2r_j \cos 2\phi_j \right). \tag{5.35}$$

If we switch to the $\begin{pmatrix} \hat{\boldsymbol{x}}_1 & \hat{\boldsymbol{x}}_2 \end{pmatrix}$ quadrature operator ordering Eq. (5.34) can be rewritten in a more compact form

$$\sigma = \begin{pmatrix} Q & S - QL \\ S - LQ & R - SL - LS + K_{\mathrm{Tot}} L \end{pmatrix}, \tag{5.36}$$

where

$$\begin{aligned} Q_{jk} &= \delta_{jk} \left(\cosh 2r_j + \sinh 2r_j \cos 2\phi_j \right), \\ R_{jk} &= \delta_{jk} \left(\cosh 2r_j - \sinh 2r_j \cos 2\phi_j \right), \\ S_{jk} &= \delta_{jk} \sinh 2r_j \sin 2\phi_j, \\ L_{jk} &= (\boldsymbol{k}\boldsymbol{k}^T)_j k = \sqrt{\kappa_j \kappa_k}. \end{aligned} \tag{5.37}$$

Extending this to include loss from mixing with vacuum leaves the covariance matrix as

$$\sigma = \begin{pmatrix} (1-\eta)\mathbb{1} + \eta Q & \eta \left(S - QL \right) \\ \eta \left(S - LQ \right) & (1-\eta)\mathbb{1} + \eta \left(R - SL - LS + K_{\mathrm{Tot}} L \right) \end{pmatrix}, \tag{5.38}$$

which gives us the σ required for the QFI.

The displacements meanwhile—in the same quadrature operator ordering—are simply attenuated to

$$\boldsymbol{d} = \sqrt{\eta} \frac{2h}{h_{\mathrm{SQL}}} \begin{pmatrix} 0 \\ \vdots \\ 0 \\ \sqrt{\kappa_1} \\ \vdots \\ \sqrt{\kappa_d} \end{pmatrix}, \tag{5.39}$$

which gives us all the necessary elements for the QFI calculation.

5.3.2 Quantum Cramér-Rao bound

The relevant QFI expression here is Eq. (5.20), where the moments are Eqs. (5.38) and (5.39). Due to the form of $\boldsymbol{d}$ given in Eq. (5.39) our QFI is

$$H(h) = \frac{8\eta}{h_{\mathrm{SQL}}^2} \sum_{j,k=1}^{d} \sqrt{\kappa_j \kappa_k} \left(\sigma^{-1}\right)_{d+j,d+k}, \tag{5.40}$$

from which we recognise only the lower right quarter of σ^{-1} is required.

The covariance matrix σ has a block matrix form as seen in Eq. (5.38) and for a block matrix we have

$$\begin{pmatrix} A & B \\ C & D \end{pmatrix}^{-1} = \begin{pmatrix} \left(A - BD^{-1}C\right)^{-1} & -\left(A - BD^{-1}C\right)^{-1} BD^{-1} \\ -D^{-1}C\left(A - BD^{-1}C\right)^{-1} & D^{-1} + D^{-1}C\left(A - BD^{-1}C\right)^{-1} BD^{-1} \end{pmatrix}, \tag{5.41}$$

where we need only the $D^{-1} + D^{-1}C\left(A - BD^{-1}C\right)^{-1} BD^{-1}$ term. In order to handle the $\left(A - BD^{-1}C\right)^{-1}$ inversion we can employ the Woodbury matrix identity Eq. (1.8) to reduce this inverse to an inverse of 2×2 and diagonal matrices. Identifying the block matrices A, B, C, and D in Eq. (5.41) with Eq. (5.38) the relevant inverses are given—using Eq. (1.8)—by

$$D^{-1} = T^{-1} - \frac{\eta}{\alpha} T^{-1} \begin{pmatrix} \boldsymbol{k} & S\boldsymbol{k} \end{pmatrix} \begin{pmatrix} K_{\mathrm{Tot}} - \eta\langle ST^{-1}S\rangle & -1 + \eta\langle T^{-1}S\rangle \\ -1 + \eta\langle T^{-1}S\rangle & -\eta\langle T^{-1}\rangle \end{pmatrix} \begin{pmatrix} \boldsymbol{k}^T \\ \boldsymbol{k}^T S \end{pmatrix} T^{-1}, \tag{5.42}$$

where we introduce the definitions $\langle Z\rangle = \mathrm{Tr}(LZ)$, and define $T = (1-\eta)\mathbb{1} + \eta R$ and $\alpha = 1 + \eta\left[K_{\mathrm{Tot}}\langle T^{-1}\rangle - 2\langle ST^{-1}S\rangle + \eta\left(\langle ST^{-1}\rangle^2 - \langle T^{-1}\rangle\langle ST^{-1}S\rangle\right)\right]$. As well as

$$\left(A - BD^{-1}C\right)^{-1} = W^{-1} - W^{-1}\begin{pmatrix} ST^{-1}\boldsymbol{k} & U\boldsymbol{k} \end{pmatrix} G^{-1} \begin{pmatrix} \boldsymbol{k}^T T^{-1} S \\ \boldsymbol{k}^T U \end{pmatrix} W^{-1}, \tag{5.43}$$

where $U = \left(Q - \eta ST^{-1}S\right)$, $W = (1-\eta)\mathbb{1} + \eta Q - \eta^2 ST^{-1}S$, and

$$G = \begin{pmatrix} \frac{\langle T^{-1}\rangle}{\eta^2} + \langle T^{-1}SW^{-1}ST^{-1}\rangle & \frac{1-\eta\langle ST^{-1}\rangle}{\eta^2} + \langle T^{-1}SW^{-1}U\rangle \\ \frac{1-\eta\langle ST^{-1}\rangle}{\eta^2} + \langle T^{-1}SW^{-1}U\rangle & \frac{-\langle Q\rangle + \eta\langle ST^{-1}S\rangle}{\eta} + \langle UW^{-1}U\rangle \end{pmatrix}. \tag{5.44}$$

The QFI then has form

$$H(h) = \frac{\frac{8\eta}{h_{\mathrm{SQL}}^2}\left[(1-\eta)\langle\Gamma\rangle + \eta\langle Q\Gamma\rangle\right]}{\left[1 - (1-\eta)\eta\langle S\Gamma\rangle\right]^2 + (1-\eta)\eta\left[\eta\langle\Gamma\rangle + (1-\eta)\langle Q\Gamma\rangle\right]\left[(1-\eta)\langle\Gamma\rangle + \eta\langle Q\Gamma\rangle\right]}, \tag{5.45}$$

where

$$\Gamma = T^{-1}W^{-1} = \left\{\left[(1-\eta)^2+\eta^2\right]\mathbb{1} + \eta(1-\eta)\left(Q+R\right)\right\}^{-1}. \tag{5.46}$$

Inverting QFI we find the QCRB

$$(\Delta h)^2 \geq \frac{h_{\mathrm{SQL}}^2}{8}\left\{\frac{\left[1-(1-\eta)\eta\langle S\Gamma\rangle\right]^2}{\eta\left[(1-\eta)\langle\Gamma\rangle+\eta\langle Q\Gamma\rangle\right]} + (1-\eta)\left[\eta\langle\Gamma\rangle+(1-\eta)\langle Q\Gamma\rangle\right]\right\}, \tag{5.47}$$

which has form $c/\sum_j a_j\kappa_j$ only for $\eta = 1$.

5.4 Homodyne detection

Homodyne detection covers both measurement of the signal quadrature—a scheme in active use [121, 149, 170, 171] in current GW detectors—and the more general frequency-dependent homodyne [121, 140, 149] which measures an arbitrary quadrature. In our model the signal quadrature homodyne can be given as a limiting case of frequency-dependent homodyne—with trivial frequency dependence—which simply requires homodyne on the $\{\hat{x}_2^{(j)}\}$ quadratures.

5.4.1 Homodyne statistics

The homodyne detection scheme we will consider requires a local rotation of each carrier mode followed by measurement of the $\hat{x}_2^{(j)}$ modes. This yields Gaussian statistics with moments

$$\boldsymbol{w} = \frac{2h}{h_{\mathrm{SQL}}}\begin{pmatrix}\sqrt{\kappa_1}\cos\theta_1\\ \sqrt{\kappa_2}\cos\theta_2\\ \vdots\\ \sqrt{\kappa_d}\cos\theta_d\end{pmatrix}, \tag{5.48}$$

and

$$\begin{aligned}\Sigma = (1-\eta)\mathbb{1} + \eta(&YQY + YSX + XSY + XRX\\ &- (XS+YQ)\,LX - XL\,(SX+QY) + K_{\mathrm{Tot}}XLX),\end{aligned} \tag{5.49}$$

where $X_{ij} = \delta_{ij}\cos\theta_i$, and $Y_{ij} = \delta_{ij}\sin\theta_i$.

5.4.2 Homodyne Fisher information

For the FI we have an analogous expression to the QFI given by Eq. (2.18) which in our case is

$$F(h) = \frac{8\eta}{h_{\mathrm{SQL}}^2} = \langle X^2 \Sigma^{-1} \rangle, \tag{5.50}$$

where Σ^{-1} can be calculated with Eq. (1.8) to be

$$\begin{aligned}\Sigma^{-1} = E^{-1} &\\ &+ E^{-1} \begin{pmatrix} X\boldsymbol{k} & (XS + YQ)\,\boldsymbol{k} \end{pmatrix} \\ &\quad \begin{pmatrix} -\langle X^2 Y^{-1} \rangle & \frac{1}{\eta} - \langle XY^{-1}\,(XS+YQ) \rangle \\ \frac{1}{\eta} - \langle XY^{-1}\,(XS+YQ) \rangle & \frac{(1-\eta)}{\eta}\langle QY^{-1} \rangle + \langle X^2 Y^{-1} \rangle \end{pmatrix}^{-1} \\ &\quad\quad \begin{pmatrix} \boldsymbol{k}^T X \\ \boldsymbol{k}^T\,(SX + QY) \end{pmatrix} E^{-1},\end{aligned} \tag{5.51}$$

where $E = (1-\eta)\mathbb{1} + \eta\left(Y^2 Q + 2YXS + X^2 R\right)$. The FI is therefore

$$\begin{aligned} F(h) &= \frac{8\eta}{h_{\mathrm{SQL}}^2} \langle X^2 \Sigma^{-1} \rangle \\ &= \frac{\frac{8\eta}{h_{\mathrm{SQL}}^2}\langle X^2 Y^{-1} \rangle}{\left[1 - \eta \langle XY^{-1}(XS+YQ) \rangle\right]^2 + \eta \langle X^2 Y^{-1} \rangle \left[(1-\eta)\langle QY^{-1} \rangle + \eta \langle X^2 Y^{-1} \rangle\right]}. \end{aligned} \tag{5.52}$$

This produces a CRB

$$\begin{aligned}(\Delta h)^2 \geq \frac{h_{\mathrm{SQL}}^2}{8} \Bigg\{ &\frac{\left[1 - \eta\left(\langle X^2 E^{-1} S \rangle + \langle YXE^{-1} Q \rangle\right)\right]^2}{\eta \langle X^2 E^{-1} \rangle} \\ &+ (1-\eta)\langle QE^{-1} \rangle + \eta \langle X^2 E^{-1} \rangle \Bigg\},\end{aligned} \tag{5.53}$$

which—generally—no longer takes a $1/x$ form for $\eta = 1$ unlike Eq. (5.47).

5.4.3 Signal quadrature Fisher information

The signal-quadrature measurement is the specific homodyne detection where $\theta_j = 0, \forall j$ which constitutes $X = \mathbb{1}$ and $Y = \mathbb{0}$, and reduces E to T. For these measurements the CRB is

$$(\Delta h)^2 \geq \frac{h_{\mathrm{SQL}}^2}{8} \left[\frac{\left(1 - \eta \langle ST^{-1} \rangle\right)^2}{\eta \langle T^{-1} \rangle} + \eta \langle T^{-1} \rangle + (1-\eta)\langle QT^{-1} \rangle \right]. \tag{5.54}$$

5.5 Optimal configurations

The bounds identified in Eqs. (5.47), (5.53) and (5.54) all take the form

$$(\Delta h)^2 \geq \frac{h_{\mathrm{SQL}}^2}{8} B(\kappa_1, \cdots, \kappa_d) = \frac{h_{\mathrm{SQL}}^2}{8} \left[\frac{\left(1 - \sum_j c_1^{(j)} \kappa_j\right)^2}{\sum_j c_2^{(j)} \kappa_j} + \sum_j c_3^{(j)} \kappa_j \right], \tag{5.55}$$

for any given input squeezing configuration, with $c_2^{(j)} > 0$ and $c_3^{(j)} \geq 0$. The equality $c_3^{(j)} = 0$ is a special case, only holding if $\eta = 1$ (and never for signal quadrature measurements) which we consider explicitly in Section 5.6.2.

Minimising the bound $B(\boldsymbol{\kappa})$ does not simply require maximisation of (any one of) κ_j as a result of the $c_3^{(j)}\kappa_j$ terms which diverge with large κ_j. Similarly the bound diverges at the opposite extreme when all $\{\kappa_j\}$ are vanishing as no light is input to extract the signal. Instead there is in general some optimal finite κ_j (e.g. some optimal intensity before which the radiation-pressure term overcomes the shot noise) which will give the best precision.

The gradient and Hessian of $B(\boldsymbol{\kappa})$ are

$$\frac{\partial B}{\partial \kappa_j} = -c_2^{(j)} \left(\frac{1 - \sum_l c_1^{(l)} \kappa_l}{\sum_l c_2^{(l)} \kappa_l} \right)^2 - 2c_1^{(j)} \left(\frac{1 - \sum_l c_1^{(l)} \kappa_l}{\sum_l c_2^{(l)} \kappa_l} \right) + c_3^{(j)}, \tag{5.56}$$

$$\frac{\partial^2 B}{\partial \kappa_j \partial \kappa_k} = \frac{2}{\sum_l c_2^{(l)} \kappa_l} \left[c_1^{(j)} + c_2^{(j)} \left(\frac{1 - \sum_l c_1^{(l)} \kappa_l}{\sum_l c_2^{(l)} \kappa_l} \right) \right] \left[c_1^{(k)} + c_2^{(k)} \left(\frac{1 - \sum_l c_1^{(l)} \kappa_l}{\sum_l c_2^{(l)} \kappa_l} \right) \right], \tag{5.57}$$

with the Hessian being positive semi-definite for $\sum_l c_2^{(l)} \kappa_l > 0$, identifying B as convex.

The solutions to Eq. (5.56) are

$$\frac{1 - \sum_l c_1^{(l)} \kappa_l}{\sum_l c_2^{(l)} \kappa_l} = -\frac{c_1^{(j)}}{c_2^{(j)}} \pm \sqrt{\left(\frac{c_1^{(j)}}{c_2^{(j)}} \right)^2 + \frac{c_3^{(j)}}{c_2^{(j)}}}, \tag{5.58}$$

where the positive solutions are valid for $\sum_l c_1^{(l)} \kappa_l < 1$ and the negative solutions otherwise.

We can recognise that $\partial_{\kappa_j} B = 0$ and $\partial_{\kappa_k} B = 0$ cannot hold simultaneously

unless

$$-\frac{c_1^{(j)}}{c_2^{(j)}}+\sqrt{\left(\frac{c_1^{(j)}}{c_2^{(j)}}\right)^2+\frac{c_3^{(j)}}{c_2^{(j)}}}=-\frac{c_1^{(k)}}{c_2^{(k)}}+\sqrt{\left(\frac{c_1^{(k)}}{c_2^{(k)}}\right)^2+\frac{c_3^{(k)}}{c_2^{(k)}}}, \tag{5.59}$$

or

$$-\frac{c_1^{(j)}}{c_2^{(j)}}-\sqrt{\left(\frac{c_1^{(j)}}{c_2^{(j)}}\right)^2+\frac{c_3^{(j)}}{c_2^{(j)}}}=-\frac{c_1^{(k)}}{c_2^{(k)}}-\sqrt{\left(\frac{c_1^{(k)}}{c_2^{(k)}}\right)^2+\frac{c_3^{(k)}}{c_2^{(k)}}}, \tag{5.60}$$

according to the value of $\sum_l c_1^{(l)}\kappa_l$.

Each κ_j lies in the domain $[0,\infty]$. We can immediately see from Eq. (5.55) that if $\kappa_j=0,\forall j$ then B diverges to infinity. At the same time if any one of κ_j diverges as $\kappa_j\to\infty$ then B again diverges to infinity.

Let us first consider the case where the conditions given in Eqs. (5.59) and (5.60) do not hold for any pair j and k. In this case the solution to $\partial_{\kappa_j}B=0$ is (discarding the negative solution)

$$\kappa_j=\frac{1}{\sqrt{\left(c_1^{(j)}\right)^2+c_2^{(j)}c_3^{(j)}}}, \tag{5.61}$$

as $\partial_{\kappa_k}B\neq 0,\forall k\neq j$ the remaining κ_k must be zero (as $\kappa_k\to\infty$ causes B to diverge and so cannot be a minimum). As such there are a set of possible minima

$$\left\{-2\frac{c_1^{(i)}}{c_2^{(i)}}+2\sqrt{\left(\frac{c_1^{(i)}}{c_2^{(i)}}\right)^2+\frac{c_3^{(i)}}{c_2^{(i)}}}\;\middle|\; i\in\{1,\cdots,d\}\right\}, \tag{5.62}$$

from which the minima of B is the minima of this set, where only the carrier l given by

$$l=\underset{j}{\operatorname{argmin}}\left\{-2\frac{c_1^{(j)}}{c_2^{(j)}}+2\sqrt{\left(\frac{c_1^{(j)}}{c_2^{(j)}}\right)^2+\frac{c_3^{(j)}}{c_2^{(j)}}}\right\} \tag{5.63}$$

is used.

When the solutions to $\partial_{\kappa_j}B=0$ and $\partial_{\kappa_k}B=0$ are compatible with one another—satisfying Eq. (5.59) or Eq. (5.60)—then a family of potential solutions exist satisfying

$$\frac{1-\sum_{k\in\mathcal{K}_j^{\pm}}c_1^{(k)}\kappa_k}{\sum_{k\in\mathcal{K}_j^{\pm}}c_2^{(k)}\kappa_k}=-\frac{c_1^{(j)}}{c_2^{(j)}}\pm\sqrt{\left(\frac{c_1^{(j)}}{c_2^{(j)}}\right)^2+\frac{c_3^{(j)}}{c_2^{(j)}}}, \tag{5.64}$$

where the summation is only over $\mathcal{K}_j^{\pm}$ as all other κ_l cannot satisfy ∂_{κ_l} and thus minimise $B(\boldsymbol{\kappa})$ by being zero. For $k \in \mathcal{K}_j^{\pm}$ we have

$$\begin{aligned} 1 - \sum_{k\in\mathcal{K}_j^{\pm}} c_1^{(k)}\kappa_k &= \left[-\frac{c_1^{(j)}}{c_2^{(j)}} \pm \sqrt{\left(\frac{c_1^{(j)}}{c_2^{(j)}}\right)^2 + \frac{c_3^{(j)}}{c_2^{(j)}}}\right] \sum_{k\in\mathcal{K}_j^{\pm}} c_2^{(k)}\kappa_k \\ &= \sum_{k\in\mathcal{K}_j^{\pm}} \left[-c_1^{(k)} \pm \sqrt{\left(c_1^{(k)}\right)^2 + c_2^{(k)}c_3^{(k)}}\right]\kappa_k, \end{aligned} \tag{5.65}$$

where we use the equality Eq. (5.59) or Eq. (5.60) which holds of all $k \in \mathcal{K}_j^{\pm}$. Rearranging we therefore require

$$\sum_{k\in\mathcal{K}_j^{\pm}} \sqrt{\left(c_1^{(k)}\right)^2 + c_2^{(k)}c_3^{(k)}}\kappa_k = \pm 1. \tag{5.66}$$

from which we see the negative solution is not possible with $\kappa_k \in [0, \infty]$.

Whenever Eq. (5.66) is satisfied and $\kappa_k = 0, \forall k \notin \mathcal{K}_j^{\pm}$ we therefore have the constant $B(\boldsymbol{\kappa})$ (as under Eq. (5.66) and all other κ_k equal to zero $\partial_{\kappa_k} B = 0$) which takes value

$$l = \underset{j}{\operatorname{argmin}} \left\{ -2\frac{c_1^{(j)}}{c_2^{(j)}} + 2\sqrt{\left(\frac{c_1^{(j)}}{c_2^{(j)}}\right)^2 + \frac{c_3^{(j)}}{c_2^{(j)}}} \right\}, \tag{5.67}$$

however when any set $\mathcal{K}_j^{+}$ is not a singleton a single-mode configuration may not uniquely be optimal.

Thus we conclude that the bounds $B(\boldsymbol{\kappa})$ are minimised by a case where only one element of $\boldsymbol{\kappa}$ is non-zero and this is a non-unique case only—but not necessarily—if Eq. (5.59) is satisfied for some j and k. We will consider—among other cases—equal squeezing input in each mode where Eq. (5.59) holds for all modes in Section 5.6.

5.6 Special cases

The full bounds given in Sections 5.3 and 5.4 represent the most general cases we consider. We were in Section 5.5 able to argue that in spite of the multi-mode coupling in such sensors the optimal configuration only involves the use of a single carrier. However these bulky expressions are less intuitive to handle, to which end we can consider the cases where each mode is identically squeezed (or indeed where no modes are squeezed) or that no loss is present in the sensor. In these cases we can specifically identify homodyne and squeezing angles which

maximise the precision of the sensor.

5.6.1 Identical squeezing

In the case that the external squeezing in each carrier is identical being $re^{i\phi}$ the fundamental quantum limit—Eq. (5.47)—becomes

$$(\Delta h)^2 \geq \frac{h_{\mathrm{SQL}}^2}{8}\left\{\frac{1+2\eta(1-\eta)(\cosh 2r-1-\kappa_{\mathrm{Tot}}\sinh 2r\sin 2\phi)}{\eta\kappa_{\mathrm{Tot}}\left[(1-\eta)+\eta\left(\cosh 2r+\sinh 2r\sin 2\phi\right)\right]} + \frac{(1-\eta)\kappa_{\mathrm{Tot}}\left(\cosh 2r+\sinh 2r\sin 2\phi\right)]}{\left[(1-\eta)+\eta\left(\cosh 2r+\sinh 2r\sin 2\phi\right)\right]}\right\}, \tag{5.68}$$

where $\kappa_{\mathrm{Tot}}=\sum_{i=1}^{d}\kappa_i$ is the only term which depends on the $\{\kappa_j\}$ variables.

In the same regime, where an identical homodyne angle $\theta_i=\theta$ is used the precision reduces to

$$(\Delta h)^2 \geq \frac{h_{\mathrm{SQL}}^2}{8}\left[\frac{\left(1+\eta\left\{\cosh 2r-\sinh 2r\cos[2(\phi+\theta)]-1\right\}\right)\sec^2\theta}{\eta\kappa_{\mathrm{Tot}}} - 2\left[\sinh 2r\sin 2\phi+\left(\cosh 2r+\sinh 2r\cos 2\phi\right)\tan\theta\right] + \kappa_{\mathrm{Tot}}\left(\cosh 2r+\sinh 2r\cos 2\phi\right)\right], \tag{5.69}$$

for which we can recognise the optimal homodyne angle to be

$$\theta=\arctan\left(\eta\frac{\kappa_{\mathrm{Tot}}\left(\cosh 2r+\sinh 2r\cosh 2\phi\right)-\sinh 2r\sin 2\phi}{1-\eta+\eta\left(\cosh 2r+\sinh 2r\cos 2\phi\right)}\right), \tag{5.70}$$

which gives the precision of the QCRB in Eq. (5.68). In the absence of squeezing this homodyne angle is simply $\theta=\arctan(\eta\kappa_{\mathrm{Tot}})$.

Measurement along the signal quadrature meanwhile is the $\theta=0$ case of Eq. (5.69)

$$(\Delta h)^2 \geq \frac{h_{\mathrm{SQL}}^2}{8}\left[\frac{\left(1+\eta\left\{\cosh 2r-\sinh 2r\cos 2\phi-1\right\}\right)}{\kappa_{\mathrm{Tot}}} - 2\sinh 2r\sin 2\phi+\kappa_{\mathrm{Tot}}\left(\cosh 2r+\sinh 2r\cos 2\phi\right)\right], \tag{5.71}$$

which can be optimised by a frequency-dependent squeezing angle $\phi=\arctan\kappa_{\mathrm{Tot}}$

$$(\Delta h)^2 \geq \frac{h_{\mathrm{SQL}}^2}{8}\left[\frac{1-\eta+\eta e^{-2r}}{\eta\kappa_{\mathrm{Tot}}}+e^{-2r}\kappa_{\mathrm{Tot}}\right]. \tag{5.72}$$

5.6.2 Lossless systems

On the other hand the lossless scenario $\eta = 1$ (reverting to external squeezings which are not necessarily identical across each carrier) is similarly interesting, representing the idealised behaviour. This substantially simplifies earlier expressions for the bounds. Moreover we recall that $\eta = 1$ enabled the equality $c_3^{(j)} = 0$ whose absence was required for the optimisation performed in Section 5.5.

The fundamental limit simplifies substantially when $\eta = 1$ to

$$(\Delta h)^2 \geq \frac{h_{\mathrm{SQL}}^2}{8} \frac{1}{K_{\mathrm{Tot}}}, \tag{5.73}$$

where K_{Tot} was defined in Eq. (5.35). We see now—in contrast to Section 5.6.1—that the $\{\kappa_i\}$ no longer appear as κ_{Tot} but is weighted according to the squeezing in each mode.

This bound now displays a shot-noise behaviour with precision improving constantly as $\kappa_i \to \infty$. Hence the optimal configuration is no longer seen for finite $\boldsymbol{\kappa}$ (in the context of Section 5.5 we now have $c_3^{(j)} = 0$). Instead we can consider a constraint on κ_{Tot} for which we can immediately see that $\kappa_j = \kappa_{\mathrm{Tot}}$ should be used where j is the mode with squeezing which achieves the largest $\cosh 2r_k + \sinh 2r_k \cos 2\phi_k$. The optimal squeezing angle is meanwhile simply $\phi = 0$ which gives

$$(\Delta h)^2 \geq \frac{h_{\mathrm{SQL}}^2}{8} \frac{1}{\sum_j \kappa_j e^{2r_j}}. \tag{5.74}$$

The CRB from homodyne similarly simplifies with $\eta = 1$ to

$$(\Delta h)^2 \geq \frac{h_{\mathrm{SQL}}^2}{8} \left\{ \frac{\left[1 - \left(\langle X^2 Z^{-1} S\rangle + \langle YXZ^{-1}Q\rangle\right)\right]^2}{\langle X^2 Z^{-1}\rangle} + \langle X^2 Z^{-1}\rangle \right\}, \tag{5.75}$$

where in this limit $Z = Y^2 Q + 2YXS + X^2 R$. The necessary homodyne angle to achieve Eq. (5.74) is

$$\theta = \arctan\left(\frac{K_{\mathrm{Tot}} - \sinh 2r_i \sin 2\phi_i}{\cosh 2r_i + \sinh 2r_i \cos 2\phi_i}\right). \tag{5.76}$$

For measurement along the signal quadrature meanwhile ($X = \mathbb{1}$ and $Y = \mathbb{0}$)

$$(\Delta h)^2 \geq \frac{h_{\mathrm{SQL}}^2}{8} \left\{ \frac{\left[1 - \langle R^{-1} S\rangle\right]^2}{\langle R^{-1}\rangle} + \langle R^{-1}\rangle \right\}. \tag{5.77}$$

5.6.3 LIGO

In the absence of external squeezing the fundamental limit (Eq. (5.68) with $r = 0$) is minimised by $\kappa_{\text{Tot}} = [(1-\eta)\eta]^{-\frac{1}{2}}$. Meanwhile optimising the precision of measurement along the signal quadrature (Eq. (5.72) with $r = 0$) requires $\kappa_{\text{Tot}} = \eta^{-\frac{1}{2}}$. The latter limit is already achieved by the current LIGO interferometer around $\Omega = 2\pi \times 90\,\text{s}^{-1}$, while the introduction of frequency-dependent homodyne detection would increase the required intensity by $1/\sqrt{1-\eta}$ which for $\eta \leq 0.99$ is no more than an order of magnitude increase in the circulating power.

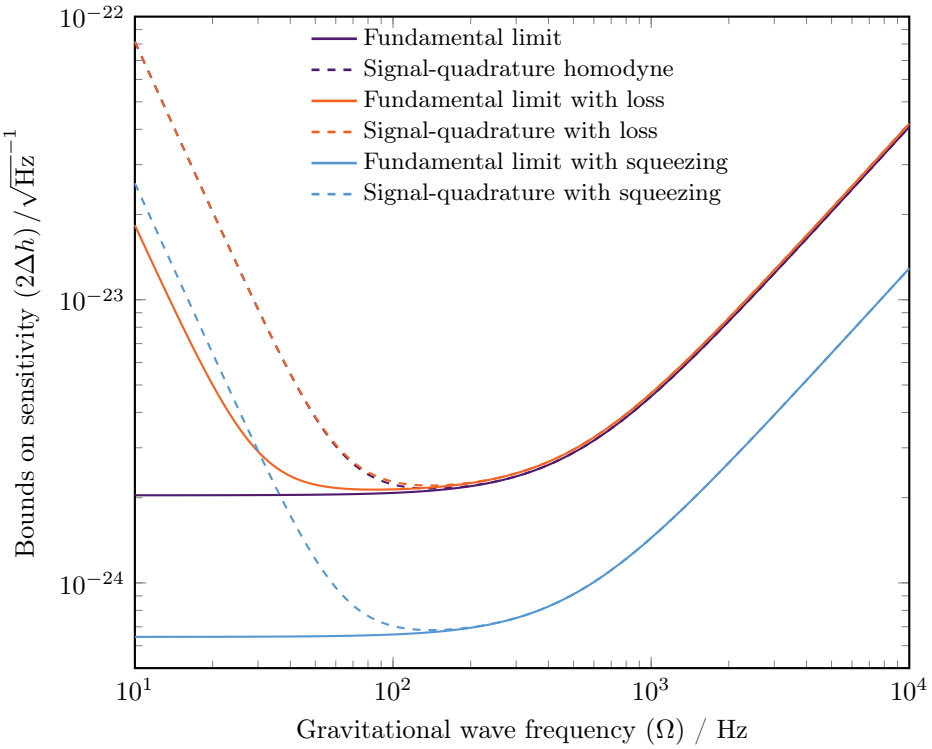

Figure 5.2: Plots of precision attainable unsqueezed and lossless, squeezed and lossless, and unsqueezed and lossy interferometers. Values based on LIGO setup in Table 5.1 in the $\kappa_{\text{Tot}} \approx gI_{\text{Tot}}$ regime, detector loss of 0.05 ($\eta = 0.95$) and an equal squeezing amplitude $e^{-2r} = 0.1$ in each mode is used. Bounds on $2\Delta h$ are plotted to give equivalent values to the spectral noise density.

For the tuned gravitational-wave detector these sensitivity plots are given for identical squeezing in Fig. 5.2, showing the case of no loss and no squeezing, no loss and 10 dB of external squeezing, and 0.05 loss and no squeezing.

5.7 Conclusions

We have studied the ability of multi-mode entangled states—generated as a natural result of radiation-pressure in the optomechanical coupling between light and a mechanical oscillator—to sense displacements and demonstrated that the simultaneous use of multiple carrier modes offers no avenue to improved sensitivity.

The optomechanical coupling responsible for this multi-mode squeezing has been proposed and witnessed itself as a squeezed light source [172–174] which can realise more precise estimation in interferometry [3, 6, 30]. Further understanding of these squeezed light sources and the role they actively play in interferometry may allow future methods to utilise this squeezing.

In our analysis we have seen a pertinent source of noise which does not simply restrict to shot-noise scaling as a result of loss [175] but which introduces a maximum precision rather than a maximum scaling. While more easily constrained in a problem such as Mach-Zehnder interferometry—where the parameter does not, generally, enter at the point of reflection—radiation-pressure will still be seen from the necessary reflection which recombines the light.

Further analysis could extend this to fully capture the detuned interferometer, which is required for the xylophone configuration to allow better shaping of the frequency sensitivity [161].

Chapter 6

Simultaneous estimation of multiple phases

Imaging and microscopy are inherently multi-parameter problems that limit the study of biological and medical systems. At the single parameter level significant enhancements from quantum systems have been seen to phase estimation through entanglement [4, 176] and squeezing [6, 176] including in GW interferometers [3, 121]; as well as—through non-classical measurements—in sub-diffraction imaging [177, 178] which has its own multi-parameter extensions [115, 179–181].

Further enhancements have been expected when extending these problems to multi-parameter estimation schemes [13, 182]. Yet quantum estimation problems involving multiple parameters add more intricate subtleties which the single-parameter cases avoid. While single-parameter estimation can—through Eq. (2.35)—always be mapped to a classical problem of sorts, no such guarantee exists for multiple parameters. In terms of Braunstein and Caves [28] this is due to non-commutativity of the SLDs. Even in the case of unitary parameters with commuting generators the SLD definition in Eq. (2.27) does not yield commuting SLDs. The QCRB itself becomes a matrix positive-definite inequality and optimisation of the bound is no longer a simple maximisation of the scalar QFI but varies according to the weighting assigned to the parameters of interest.

These multi-parameter problems have typically pursued two distinct routes: potential advantages from simultaneous estimation of multiple parameters [13, 182] and trade-offs in multiple parameters such as unitary and noise parameters [41, 114, 183].

Humphreys et al. [13] demonstrated that the precision of simultaneous phase estimation could be improved by the number of parameters to estimate. While other schemes were demonstrated to achieve the same scaling [182, 184–188] the

required optical states[1] are no more, if not less, practical than the generalised N00N states of Humphreys et al. [13] where overheads in probabilistic generation likely outweigh any potential improvement in precision [189].

Alongside the N00N state both squeezed vacuum [176] and Holland-Burnett [30, 176, 190] states attain the same Heisenberg scaling for a single-phase interferometer. Their generation requires, in combination with linear optics, optical squeezing or single-photon sources respectively. For optical systems these therefore presented the most promising approach to access this improved scaling in parameter number. Initial studies seem to undermine this optimism demonstrating no such scaling with parameter number [DB1, 191].

In this chapter results first published as Gagatsos et al. [DB1] are presented which demonstrate the (limited) potential advantage from using Gaussian states in multiple phase estimation. An alternative derivation of the QFI will be given here alongside a more in-depth discussion of the attainability and global phase formulation.

6.1 Pure Gaussian state estimation

In the case of pure states our estimation takes the form of states $|\psi_{\boldsymbol{\phi}}\rangle\langle\psi_{\boldsymbol{\phi}}| = U_{\boldsymbol{\phi}}|\psi\rangle\langle\psi|U_{\boldsymbol{\phi}}^{\dagger}$, where the parameter is encoded by a unitary transformation. For a Gaussian state where the parameter is encoded in the moments as

$$\boldsymbol{d}_{\boldsymbol{\phi}} = \mathcal{S}_{\boldsymbol{\phi}}\boldsymbol{d}_0, \quad \sigma_{\boldsymbol{\phi}} = \mathcal{S}_{\boldsymbol{\phi}}\sigma_0\mathcal{S}_{\boldsymbol{\phi}}^T, \tag{6.1}$$

the pure state QFI can be reduced further from Eq. (3.80) to

$$\begin{aligned} H_{jk} = {} & 2\boldsymbol{d}_0^T[\mathcal{S}_{\boldsymbol{\phi}}^{-1}(\partial_j\mathcal{S}_{\boldsymbol{\phi}})]^T\sigma_0^{-1}\mathcal{S}_{\boldsymbol{\phi}}^{-1}(\partial_k\mathcal{S}_{\boldsymbol{\phi}})\boldsymbol{d}_0 \\ & + \frac{1}{2}\operatorname{Tr}\left[\mathcal{S}_{\boldsymbol{\phi}}^{-1}(\partial_j\mathcal{S}_{\boldsymbol{\phi}})\mathcal{S}_{\boldsymbol{\phi}}^{-1}(\partial_k\mathcal{S}_{\boldsymbol{\phi}}) + [\mathcal{S}_{\boldsymbol{\phi}}^{-1}(\partial_j\mathcal{S}_{\boldsymbol{\phi}})]^T\sigma_0^{-1}\mathcal{S}_{\boldsymbol{\phi}}^{-1}(\partial_k\mathcal{S}_{\boldsymbol{\phi}})\sigma_0\right]. \end{aligned} \tag{6.2}$$

It should be noted that the only phase-dependent quantity in Eq. (6.2) is $\mathcal{S}_{\boldsymbol{\phi}}^{-1}\partial_j\mathcal{S}_{\boldsymbol{\phi}}$ while the other terms required are the initial moments. Furthermore we have $\sigma\Omega\sigma = \Omega$ for a pure state or $\sigma^{-1} = -\Omega\sigma\Omega$ as per Eq. (3.50) which gives us

$$\begin{aligned} H_{jk} = {} & 2\boldsymbol{d}_0^T[\Omega\mathcal{S}_{\boldsymbol{\phi}}^{-1}(\partial_j\mathcal{S}_{\boldsymbol{\phi}})]^T\sigma_0\Omega\mathcal{S}_{\boldsymbol{\phi}}^{-1}(\partial_k\mathcal{S}_{\boldsymbol{\phi}})\boldsymbol{d}_0 \\ & + \frac{1}{2}\operatorname{Tr}\left[\mathcal{S}_{\boldsymbol{\phi}}^{-1}(\partial_j\mathcal{S}_{\boldsymbol{\phi}})\mathcal{S}_{\boldsymbol{\phi}}^{-1}(\partial_k\mathcal{S}_{\boldsymbol{\phi}}) + [\Omega\mathcal{S}_{\boldsymbol{\phi}}^{-1}(\partial_j\mathcal{S}_{\boldsymbol{\phi}})]^T\sigma_0\Omega\mathcal{S}_{\boldsymbol{\phi}}^{-1}(\partial_k\mathcal{S}_{\boldsymbol{\phi}})\sigma_0\right]. \end{aligned} \tag{6.3}$$

[1] For non-optical systems, the proposed entangled qubit states of Baumgratz and Datta [182] are likely feasible to one day realise.

6.2 Mach-Zehnder interferometry

We begin by reviewing the two-mode single-phase Mach-Zehnder interferometer (MZI) with pure Gaussian states. The Mach-Zehnder interferometer involves two beam splitters either side of a relative phase shift between the two arms. This simple interferometer has been well-studied in terms of its sensitivity [30, 145, 176, 192–194]. We briefly review the precision given by N00N states and then by pure Gaussian states. The single phase interferometer considered here will represent one of the single phase shift standards to which we compare multiple phase schemes introduced in Section 6.3, the other being (for Gaussian states only) the single-mode with a reference phase scheme which is introduced in Section 6.3.2.

6.2.1 N00N state input

Inputting a N00N state directly before the phase shift—as shown in Fig. 6.1—the unitary evolution is simply

$$U\left(\frac{|N0\rangle + |0N\rangle}{\sqrt{2}}\right) = e^{iN(\phi_1+\phi_2)/2}\frac{e^{iN\varphi}|N0\rangle + e^{-iN\varphi}|0N\rangle}{\sqrt{2}}, \tag{6.4}$$

where $\varphi = (\phi_1 - \phi_2)/2$. Whence the QCRB can be calculated using Eq. (2.28) as

$$(\Delta\varphi)^2 \geq \frac{1}{N^2}, \tag{6.5}$$

which—scaling quadratically with the number of photons—displays the famous Heisenberg scaling, rather than the SNL which limits the repeated use of single photons.

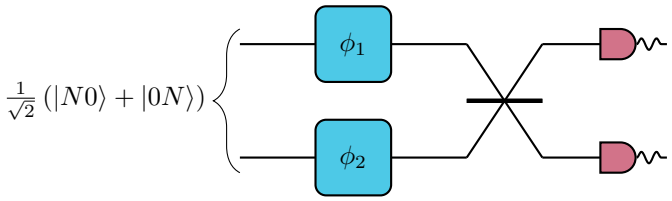

Figure 6.1: A single relative phase shift in a balanced Mach-Zehnder interferometer. N00N states are used to estimate the relative phase shift $\varphi = (\phi_1 - \phi_2)/2$.

6.2.2 Gaussian state input

Instead when inputting pure Gaussian states (before a beam splitter), as illustrated in Fig. 6.2 we have two single-mode Gaussian states each with a complex

displacement β_j and a complex squeezing ζ_j. These then go through a beam splitter

$$U_{\mathrm{BS}} = \frac{1}{\sqrt{2}} \begin{pmatrix} 1 & 1 \\ 1 & -1 \end{pmatrix}, \tag{6.6}$$

followed by a phase shift

$$U_{\boldsymbol{\phi}} = \begin{pmatrix} e^{i\phi_1} & 0 \\ 0 & e^{i\phi_2} \end{pmatrix}, \tag{6.7}$$

and another identical beam splitter U_{BS}. In many cases the standard photon detection scheme after the second beam splitter proves sufficient to attain the QCRB [145, 195].

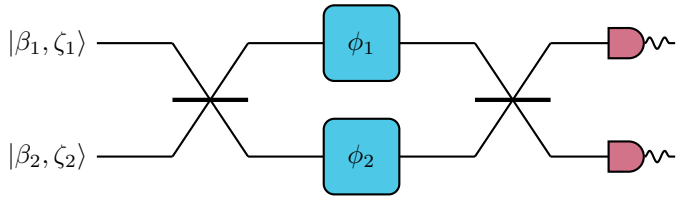

Figure 6.2: A single relative phase shift in a balanced Mach-Zehnder interferometer. Gaussian states are used to estimate the relative phase shift $\varphi = (\phi_1 - \phi_2)/2$.

The moments of the input covariance matrix are[2]

$$\begin{aligned} \boldsymbol{d} &= \sqrt{2} \begin{pmatrix} \Re\beta_1 \\ \Im\beta_1 \\ \Re\beta_2 \\ \Im\beta_2 \end{pmatrix}, \\ \sigma &= \bigoplus_{j=1}^{2} \begin{pmatrix} \cosh 2|\zeta_1| + \sinh 2|\zeta_1| \cos 2\theta_1 & \sinh 2|\zeta_1| \sin 2\theta_1 \\ \sinh 2|\zeta_1| \sin 2\theta_1 & \cosh 2|\zeta_1| - \sinh 2|\zeta_1| \cos 2\theta_1 \end{pmatrix}, \end{aligned} \tag{6.8}$$

where $\theta_j = \arg \zeta_j$. In order to calculate the QFI we need only consider the state before $U_{\boldsymbol{\phi}}$ as the QFI is invariant under parameter-independent unitary transformations (see Section 2.4.1). The necessary symplectic transformations are then

$$\mathcal{S}_{\mathrm{BS}} = \frac{1}{\sqrt{2}} \begin{pmatrix} \mathbb{1}_{2\times 2} & \mathbb{1}_{2\times 2} \\ \mathbb{1}_{2\times 2} & -\mathbb{1}_{2\times 2} \end{pmatrix}, \tag{6.9}$$

[2]Utilising the $\hat{\boldsymbol{Q}}$ quadrature ordering

and

$$\mathcal{S}_{\boldsymbol{\phi}} = \begin{pmatrix} \cos\phi_1 & -\sin\phi_1 & 0 & 0 \\ \sin\phi_1 & \cos\phi_1 & 0 & 0 \\ 0 & 0 & \cos\phi_2 & -\sin\phi_2 \\ 0 & 0 & \sin\phi_2 & \cos\phi_2 \end{pmatrix}. \tag{6.10}$$

In line with Eq. (6.3) we first calculate

$$\mathcal{S}_{\boldsymbol{\phi}}^{-1}\partial_\varphi \mathcal{S}_{\boldsymbol{\phi}} = \begin{pmatrix} 0 & -1 & 0 & 0 \\ 1 & 0 & 0 & 0 \\ 0 & 0 & 0 & 1 \\ 0 & 0 & -1 & 0 \end{pmatrix}, \tag{6.11}$$

where $\varphi = (\phi_1 - \phi_2)/2$ is the relative phase shift in the interferometer. With these expressions we can then explicitly calculate the QFI with respect to the phase φ from Eq. (6.2) as

$$\begin{aligned} H = {} & 2\left[\cosh 2|\zeta_1|\cosh 2|\zeta_2| - 1 + \sinh 2|\zeta_1|\sinh 2|\zeta_2|\cos 2(\theta_1-\theta_2)\right] \\ & + 4|\beta_1|^2\left[\cosh 2|\zeta_2| + \sinh 2|\zeta_2|\cos\left(2\theta_2 - 2\arg\beta_1\right)\right] \\ & + 4|\beta_2|^2\left[\cosh 2|\zeta_1| + \sinh 2|\zeta_1|\cos\left(2\theta_1 - 2\arg\beta_2\right)\right]. \end{aligned} \tag{6.12}$$

The energy constraint with which we wish to maximise Eq. (6.12) is $\sum_{j=1}^{2}|\beta_j|^2 + \sinh^2|\zeta_j|$. We can immediately maximise H with respect to $\{\arg\beta_j\}$ with $\arg\beta_1 = \theta_2$ and $\arg\beta_2 = \theta_1$ which gives us

$$\begin{aligned} H = {} & \left(\cosh 2|\zeta_1|\cosh 2|\zeta_2| - 1 + \sinh 2|\zeta_1|\sinh 2|\zeta_2|\cos 2(\theta_1-\theta_2)\right) \\ & + 4\left(|\beta_1|^2 e^{2|\zeta_2|} + |\beta_2|^2 e^{2|\zeta_1|}\right), \end{aligned} \tag{6.13}$$

from which we can then see that we require $\theta_1 = \theta_2$ giving

$$H = 4\left[\sinh^2(|\zeta_1| + |\zeta_2|) + \left(|\beta_1|^2 e^{2|\zeta_2|} + |\beta_2|^2 e^{2|\zeta_1|}\right)\right]. \tag{6.14}$$

This can be rewritten as

$$\begin{aligned} H &= e^{-2|\zeta_1|}e^{-2|\zeta_2|} - 2 + e^{2|\zeta_1|}\left(e^{2|\zeta_2|} + 4|\beta_2|^2\right) + e^{2|\zeta_2|}\left(e^{2|\zeta_1|} + 4|\beta_1|^2\right) \\ &\leq e^{-2|\zeta_1|}e^{-2|\zeta_2|} - 2 + e^{2|\zeta_1|}\left(\sqrt{N_2} + \sqrt{N_2+1}\right)^2 + e^{2|\zeta_2|}\left(\sqrt{N_1} + \sqrt{N_1+1}\right)^2, \end{aligned} \tag{6.15}$$

where the inequality comes from maximisation of

$$e^{2|\zeta_j|} + 4|\beta_j|^2 = \left(\sqrt{N_{|\zeta_j|}} + \sqrt{N_{|\zeta_j|}+1}\right)^2 + 4N_{|\beta_j|}, \tag{6.16}$$

subject to $N_{|\zeta_j|} + N_{|\beta_j|} = N_j$. The upper bound of Eq. (6.15) is then monotonically increasing in $|\zeta_j|$ allowing us to conclude $|\beta_j| = 0, \forall j$ maximises the upperbound and also saturates the equality of Eq. (6.15) to give

$$H = 4\sinh^2(|\zeta_1| + |\zeta_2|). \tag{6.17}$$

Subject to $\sinh^2|\zeta_1| + \sinh^2|\zeta_2| = N_{\mathrm{Tot}}$, Eq. (6.17) is straightforwardly maximised by $\zeta_1 = \zeta_2$ which gives

$$H = 4N_{\mathrm{Tot}}(N_{\mathrm{Tot}} + 2), \tag{6.18}$$

and so a CRB of

$$(\Delta\phi)^2 \geq \frac{1}{4N_{\mathrm{Tot}}(N_{\mathrm{Tot}} + 2)}, \tag{6.19}$$

displaying the same Heisenberg scaling of the N00N state in Eq. (6.5).

Before moving on, we first note that this is not necessarily the greatest precision attainable with an arbitrary Gaussian state. In fact a higher QFI can be attained by putting two mode squeezing into the beam splitter such that it results in the product state $|0\rangle|\zeta e^{i\phi_2}\rangle$ where $|\zeta| = \sinh^{-1}(\sqrt{N_{\mathrm{Tot}}})$ [196]. While this does indeed maximise the QFI the state is clearly insensitive to the relative phase shift $(\phi_1 - \phi_2)/2$ and only picks up a dependence of ϕ_2, however as the setup does not preclude knowledge of $(\phi_1 + \phi_2)/2$ an estimate of ϕ_2 with perfect knowledge of $(\phi_1 + \phi_2)/2$ allows for an estimate of $(\phi_1 - \phi_2)/2$ to be made. In general it is necessary to properly account for such uninteresting but nevertheless unknown or unknowable parameters by using an appropriate mixed state input [193, 197] or through a nuisance parameter analysis [198, 199].

6.3 Multiple phase estimation

We will generalise to the case where a number of phase shifts are to be estimated. While the general QFI matrices will be derived in order to perform any optimisation over input states our figure of merit will be $\sum_j (\Delta\varphi_j)^2$—where equal weighting is put on the value of measuring each phase shift—and so in terms of the QFI we will be comparing $\mathrm{Tr}\left(H^{-1}\right)$.

Two QFIs will be used, $H(\boldsymbol{\phi})$ and $\mathcal{H}(\boldsymbol{\varphi})$, which refer respectively to the single-mode phase shift parameters and the relative phase shifts and are therefore $(d+1)\times(d+1)$ and $d\times d$ respectively. In Section 6.3.3 where we review the generalised N00N states of Humphreys et al. [13]—as in Section 6.2—we jump directly to $\mathcal{H}$. Meanwhile in Section 6.4 we first identify H and can then transform—as Eq. (2.29)—to $\mathcal{H}$ when concerned with the relative phase parameters.

6.3.1 Reference phase formulation

In general quantum mechanics the global phase is an arbitrary phase $e^{i\phi_g}$ whose action on a pure state $|\psi\rangle$ is $e^{i\phi_g}|\psi\rangle$ is unresolvable through any experiment. The phase ϕ_g will not appear in any reconstructed probabilities as it commutes with any state as $\rho = e^{i\phi_g}\rho e^{-i\phi_g}$.

With linear optics we can consider a rather similar "global" phase shift $e^{i\phi\hat{n}_{\mathrm{Tot}}}$, where $\hat{n}_{\mathrm{Tot}} = \sum_j \hat{n}_j$, which does not exhibit the same fundamental issues as there exist POVMs which do depend on this phase ϕ. The nature of these POVMs however do not necessarily facilitate practical implementations. While a unitary can map $(|0\rangle+|1\rangle)/\sqrt{2}$ to $|1\rangle$ freely if $|0\rangle$ and $|1\rangle$ denote computational eigenstates (e.g. energy levels of an atom), when $|0\rangle$ and $|1\rangle$ are vacuum and photon states this is not possible with linear optics (which conserves average photon number in the whole system). More generally we can consider that a phase shift $e^{i\phi\hat{n}_{\mathrm{Tot}}}$ commutes with any linear optic unitary whose action is $\hat{a}'_j = \sum_k U_{jk}\hat{a}_k$ and the statistics of a photon number resolving detector (PNRD) is independent of any phase on the Fock states such as above.

In order to calculate appropriate bounds we can therefore consider that of the set of phases $\{\phi_j\}$ with a unitary generated by Hamiltonian $\sum_{j=0}^{d}\phi_j\hat{n}_j$ the phase proportional to $\hat{n}_{\mathrm{Tot}}$ cannot be detected. Such a Hamiltonian can be rewritten—to isolate the $\hat{n}_{\mathrm{Tot}}$ term—as

$$\sum_{j=0}^{d}\phi_j\hat{n}_j = \bar{\varphi}\hat{n}_{\mathrm{Tot}} + \sum_{j=1}^{d}\varphi_j\left(\hat{n}_j - \hat{n}_0\right), \tag{6.20}$$

where $\bar{\varphi} = \frac{1}{d+1}\sum_{j=0}^{d}\phi_j$ and $\varphi_j = \phi_j - \bar{\varphi}$. We can therefore consider that the phases $\{\varphi_j\}$ are the resolvable parameters of interest. This is closer in spirit to the use of $\hat{n}_1 - \hat{n}_0$ in the MZI which is necessary to see an attainable QFI [193]. Optimisation of the QFI over Gaussian states gives distinct results for the optimal states when using the single-mode $\hat{n}_1$ generator [200] as opposed to the two-mode $\hat{n}_1 - \hat{n}_0$ generator [176].

6.3.2 References in homodyne detection

The use of homodyne detection is an exception to the previous discussion. In homodyne detection (see Section 3.4.3) an LO is introduced in addition to the quantum state being measured. With the addition of an LO an arbitrary quadrature can be measured by tuning the phase of the LO (in practice the relative phase between the LO and the system). This enables the resolution of

a phase shift in a single-mode where the phase shift is relative to the LO itself rather than a second mode of the interferometer [193].

Therefore when an LO is used (or available) a single-mode Gaussian state can be considered[3]. We therefore briefly review the phase sensitivity of a single-mode Gaussian state $|\beta, \zeta\rangle$ to an unknown phase shift $e^{i\phi\hat{n}}$, as illustrated in Fig. 6.3; such a setup is considered in more depth in Monras [201].

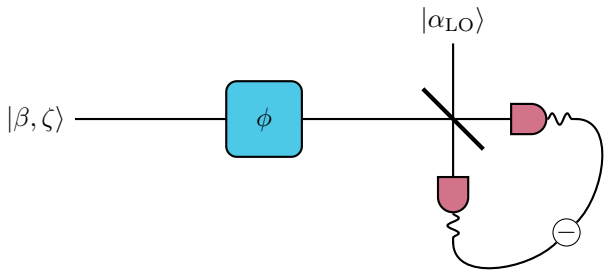

Figure 6.3: A single phase shift ϕ relative to a local oscillator resolved through homodyne detection.

The single-mode Gaussian state $|\beta, \zeta\rangle$ with $\arg\zeta = \theta$ has QFI with respect to the phase ϕ

$$H = 2\left\{\sinh^2 2|\zeta| + 2|\beta|^2\left[\cosh 2|\zeta| + \sinh 2|\zeta|\cos 2\left(\theta - \arg\beta\right)\right]\right\}, \tag{6.21}$$

as in Section 6.2.2 we immediately see $\arg\beta = \theta$ to maximise H. For a single-mode the average number of photons is $N_{\mathrm{Tot}} = |\beta|^2 + \sinh^2|\zeta|$ [201], substituting $|\beta|^2 = N_{|\beta|}$ and $\sinh^2|\zeta| = N_{\mathrm{Tot}} - N_{|\beta|}$ into Eq. (6.21) with $\arg\beta = \theta$ we have

$$H = 8N_{\mathrm{Tot}}(N_{\mathrm{Tot}}+1) - 8N_{|\beta|}\left[\frac{1}{2} + N_{\mathrm{Tot}} - \sqrt{\left(N_{\mathrm{Tot}} - N_{|\beta|}\right)\left(N_{\mathrm{Tot}} + 1 - N_{|\beta|}\right)}\right], \tag{6.22}$$

which (for $N_{\mathrm{Tot}} \geq N_{|\beta|} \geq 0$) is monotonically decreasing with $N_{|\beta|}$ and so maximised by $N_{|\beta|} = 0$ giving

$$H = 8N_{\mathrm{Tot}}(N_{\mathrm{Tot}}+1), \tag{6.23}$$

or a precision

$$(\Delta\phi)^2 \geq \frac{1}{8N_{\mathrm{Tot}}(N_{\mathrm{Tot}}+1)} \tag{6.24}$$

[3]No obvious equivalent single-mode N00N state exists as a linear phase shift applied to a Fock state is a global phase shift which cannot be detected through interference with an LO or otherwise.

6.3.3 Multi-mode N00N-like states

We first review the foundational simultaneous phase estimation analysis of Humphreys et al. [13] which showed a significant increase in the total precision for estimating d relative phase shifts using $(d+1)$-mode N00N-like states with the scheme illustrated in Fig. 6.4. This N00N-like state takes form

$$|\psi\rangle = \alpha\,|N,0,0,\cdots,0\rangle + \beta(|0,N,0,\cdots,0\rangle + \cdots + |0,0,\cdots,0,N\rangle), \tag{6.25}$$

where the $|N,0,0,\cdots,0\rangle$ state is allowed to have a different weighting to respect the treatment of the 0 mode as the reference. The normalisation dictates $\alpha^2 + d\beta^2 = 1$, with the phases of α and β not affecting the QFI and so taken to be real. As we are dealing with fixed photon number states the average phase $\tilde{\varphi}$ behaves for this state as an actual global phase which the introduction of an LO cannot assist in resolving.

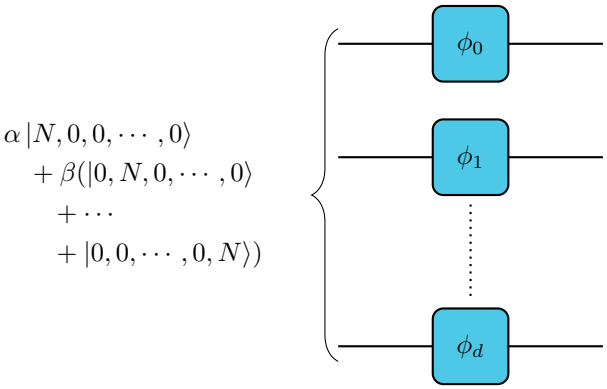

Figure 6.4: Multi-mode N00N state incident on multiple single phase shifts

The QFI can be calculated with Eq. (2.28) where $\partial_j\,|\psi\rangle = i(\hat{n}_j - \hat{n}_0)\,|\psi\rangle$ which gives us[4]

$$H_{jk}(\boldsymbol{\varphi}) = 4N^2\left[\beta^2\delta_{jk} + \alpha^2 - \left(\alpha^2 - \beta^2\right)^2\right], \tag{6.26}$$

or in matrix form

$$H(\boldsymbol{\varphi}) = 4N^2\left(\beta^2\mathbb{1} + \left\{\alpha^2 - \left[\beta^2 - \alpha^2\right]^2\right\}\boldsymbol{u}\boldsymbol{u}^T\right). \tag{6.27}$$

This analysis can be extended to arbitrary single-mode state instead of the Fock state $|N\rangle$ without significant additional complications [188].

[4]This QFI differs from that of Humphreys et al. [13] due to the use of a different set of phases as described in Section 6.3.1. Both the optimal state and precision we proceed to identify differ slightly, but crucially agree in scaling with both d and N.

The QFI can then be inverted by noting it has form $H = D + \boldsymbol{u}^T\boldsymbol{u}$ where D is diagonal and $u_j = 1, \forall j$ and so Eq. (1.9) can be applied, moreover as we directly want $\mathrm{Tr}\left(H^{-1}\right)$ we can further simplify Eq. (1.9) to

$$\mathrm{Tr}\left[\left(A + \boldsymbol{u}\boldsymbol{v}^T\right)^{-1}\right] = \mathrm{Tr}\left(A^{-1}\right) - \frac{\boldsymbol{v}^T A^{-2}\boldsymbol{u}}{1 + \boldsymbol{v}^T A^{-1}\boldsymbol{u}}. \tag{6.28}$$

Thus in general we have

$$\mathrm{Tr}\left(H^{-1}\right) = \frac{1}{4N^2}\left\{\frac{d}{\beta^2} - \frac{d\left[\alpha^2 - \left(\beta^2 - \alpha^2\right)^2\right]/\beta^4}{1 + d\left[\alpha^2 - \left(\beta^2 - \alpha^2\right)^2\right]/\beta^2}\right\}. \tag{6.29}$$

Optimising over $\alpha \in [0, 1]$ we find

$$\alpha = \frac{1}{\sqrt{1 + \sqrt{d^3 + d^2 - d}}} \tag{6.30}$$

and so the maximum precision is

$$\mathrm{Tr}\left(H^{-1}\right) = \frac{d}{4N^2}\left(\frac{\sqrt{d\left(d^2 + d - 1\right)} - 1}{d + 1}\right)^2. \tag{6.31}$$

From Eq. (6.31) we can see that for large $d \gg 1$ the best precision gives a scaling

$$\mathrm{Tr}\left(H^{-1}\right) \sim \frac{d^2}{N^2}, \tag{6.32}$$

demonstrating not just a Heisenberg scaling in the number of photons but also a superior scaling in the number of parameters d. By comparison if we divided N photons across d single-parameter experiments each, individually, attaining a Heisenberg scaling the total precision would behave as d^3/N^2.

While this scheme satisfies Eq. (2.36) [13] (see also Section 6.5.1) the measurement scheme method proposed in Humphreys et al. [13] requires a projection onto the final state. The final state has a parameter-dependence which necessitates the use of an adaptive measurement scheme, moreover the final state must be mapped to a feasible measurement. For states generated by single-photon inputs to a multi-mode beam splitter this is achievable with the same linear optics and PNRDs, however in general the final state projection scheme is not sufficient for all pure states [49]. The additional conditions of Pezzè et al. [49] are satisfied for the case of Humphreys et al. [13], however the state Eq. (6.25) requires either prohibitively extreme optical nonlinearities or probabilistic methods to generate [189] which do not lend themselves to implementing the necessary POVM.

6.4 Gaussian states

The general pure Gaussian state picture we shall consider here is an input product state of displaced, squeezed single-mode states which is incident on a general linear unitary U before being exposed to a phase $\{\phi_j\}$ (one in each arm) or the interferometer. This scheme is illustrated in Fig. 6.5. The QFI can then be calculated from this state[5] with the use of Eq. (6.3).

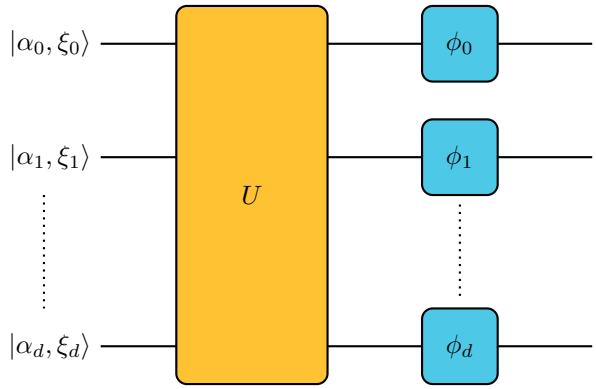

Figure 6.5: Generic multi-mode pure Gaussian state incident on multiple single phase shifts

In line with Eq. (6.3) we first calculate

$$\mathcal{S}_{\boldsymbol{\phi}}^{-1}\partial_j\mathcal{S}_{\boldsymbol{\phi}} = \bigoplus_{k=0}^{d}\delta_{jk}\begin{pmatrix}0 & -1\\ 1 & 0\end{pmatrix}, \tag{6.33}$$

further we recall Eq. (3.50) gives us $\sigma^{-1} = -\Omega\sigma\Omega$ from which we can resolve the inverses in Eq. (6.3) and instead evaluate $\Omega\mathcal{S}_{\boldsymbol{\phi}}\partial_j\mathcal{S}_{\boldsymbol{\phi}}$ which is

$$\Omega\mathcal{S}_{\boldsymbol{\phi}}\partial_j\mathcal{S}_{\boldsymbol{\phi}} = \bigoplus_{k=0}^{d} -\delta_{jk}\mathbb{1}_{2\times 2}. \tag{6.34}$$

The QFI matrix elements—for the phases $\{\phi_j\}$—are then

$$\begin{aligned} H_{jk} = -\delta_{jk} &+ 2\begin{pmatrix}d_{2j-1} & d_{2j}\end{pmatrix}\begin{pmatrix}\sigma_{2j-1,2k-1} & \sigma_{2j-1,2k}\\ \sigma_{2j,2k-1} & \sigma_{2j,2k}\end{pmatrix}\begin{pmatrix}d_{2k-1}\\ d_{2k}\end{pmatrix}\\ &+ \frac{1}{2}\begin{pmatrix}1 & 1\end{pmatrix}\begin{pmatrix}\sigma_{2j-1,2k-1} & \sigma_{2j-1,2k}\\ \sigma_{2j,2k-1} & \sigma_{2j,2k}\end{pmatrix}\circ\begin{pmatrix}\sigma_{2j-1,2k-1} & \sigma_{2j-1,2k}\\ \sigma_{2j,2k-1} & \sigma_{2j,2k}\end{pmatrix}\begin{pmatrix}1\\ 1\end{pmatrix}, \end{aligned} \tag{6.35}$$

where $\circ$ is the element-wise Hadamard product $(A\circ B)_{jk} = A_{jk}B_{jk}$, and we use

[5] Using specific results for unitary parameters in pure states the QFI calculation can in fact be performed on the state before the phase shifts [35, 182]

$\sigma = \sigma^T$ to identify the Hadamard product formulation. In matrix form this QFI can be written—as is necessary to identify the inverse—as

$$H = -\mathbb{1} + \begin{pmatrix} 1 & 1 \end{pmatrix} \otimes \mathbb{1} \left[\sigma \circ \left(2\boldsymbol{d}\boldsymbol{d}^T + \frac{1}{2}\sigma \right) \right] \begin{pmatrix} 1 \\ 1 \end{pmatrix} \otimes \mathbb{1}, \tag{6.36}$$

where we revert to the $\hat{\boldsymbol{R}}$ ordering of the quadrature vector.

Now we have $\boldsymbol{\alpha}$, $\boldsymbol{\xi}$, and U to optimise over. In order to produce any multi-mode Gaussian state it is sufficient to take product squeezed vacuum states followed by a general linear unitary [62]. Moreover that squeezing need not be arbitrary and so we can fix $\xi_j = \xi_j^{*}$[6] by noting that a single mode phase shift $e^{iv\hat{n}}$ on $|0, \xi\rangle$ yields a rotated squeezed vacuum state $|0, \xi e^{iv}\rangle$ and furthermore that single-mode phase shift can be absorbed into the arbitrary unitary U.

We therefore have that σ is

$$\begin{aligned} \sigma &= \begin{pmatrix} \Re U & -\Im U \\ \Im U & \Re U \end{pmatrix} \begin{pmatrix} D_{\boldsymbol{\xi}} & \mathbb{0} \\ \mathbb{0} & D_{\boldsymbol{\xi}}^{-1} \end{pmatrix} \begin{pmatrix} \Re U^T & \Im U^T \\ -\Im U^T & \Re U^T \end{pmatrix} \\ &= \begin{pmatrix} \Re U D_{\boldsymbol{\xi}} \Re U^T + \Im U D_{\boldsymbol{\xi}}^{-1} \Im U^T & \Re U D_{\boldsymbol{\xi}} \Im U^T - \Im U D_{\boldsymbol{\xi}}^{-1} \Re U^T \\ -\Re U D_{\boldsymbol{\xi}}^{-1} \Im U^T + \Im U D_{\boldsymbol{\xi}} \Re U^T & \Im U D_{\boldsymbol{\xi}} \Im U^T + \Re U D_{\boldsymbol{\xi}}^{-1} \Re U^T \end{pmatrix}, \end{aligned} \tag{6.37}$$

with $D_{\boldsymbol{\xi}} = \operatorname{diag}\left(e^{2\xi_0}, \cdots, e^{2\xi_d}\right)$. While $\boldsymbol{d}$ is

$$\boldsymbol{d} = \sqrt{2} \begin{pmatrix} \Re U \Re \boldsymbol{\alpha} - \Im U \Im \boldsymbol{\alpha} \\ \Re U \Im \boldsymbol{\alpha} + \Im U \Re \boldsymbol{\alpha} \end{pmatrix}. \tag{6.38}$$

For simplicity we can work with the final displacement vector

$$\boldsymbol{d} = \sqrt{2} \begin{pmatrix} \Re \boldsymbol{\gamma} \\ \Im \boldsymbol{\gamma} \end{pmatrix} \tag{6.39}$$

where $\boldsymbol{\gamma} = U\boldsymbol{\alpha}$. This is a simple rotation of the displacement vector and so any constraint on the total displacement energy constrains $|\boldsymbol{\alpha}|$ and $|\boldsymbol{\gamma}|$ equivalently.

Having identified a formula for the QFI of the phases $\{\phi_j\}$ for the Gaussian state input setup illustrated by Fig. 6.5 we now turn to explicit optimisation of this general Gaussian input state. We will first take the general form of the QFI $H(\boldsymbol{\phi})$ from Eq. (6.36) and apply Eqs. (6.37) and (6.38) before considering the two reference mode formulations $\operatorname{Tr}(H^{-1}(\boldsymbol{\phi}))$ and $\operatorname{Tr}(\mathcal{H}^{-1}(\boldsymbol{\varphi}))$ and exploring the performance of these states with respect to the single-phase results presented in Section 6.2.2.

[6] Instead of enforcing $\xi_j = \xi_j^{*}$ one could chose $\alpha_j = \alpha_j^{*}$, although these choices are not simultaneously possible.

6.4.1 Quantum Fisher information

Substituting Eq. (6.37) into Eq. (6.36) we find the QFI to be

$$\begin{aligned}H = \frac{1}{2}\Big[&\left(\Re U D_{\boldsymbol{\xi}} \Re U^T + \Im U D_{\boldsymbol{\xi}}^{-1} \Im U^T\right)^{\circ 2} + \left(\Re U D_{\boldsymbol{\xi}} \Im U^T - \Im U D_{\boldsymbol{\xi}}^{-1} \Re U^T\right)^{\circ 2} \\ &+ \left(-\Re U D_{\boldsymbol{\xi}}^{-1} \Im U^T + \Im U D_{\boldsymbol{\xi}} \Re U^T\right)^{\circ 2} + \left(\Im U D_{\boldsymbol{\xi}} \Im U^T + \Re U D_{\boldsymbol{\xi}}^{-1} \Re U^T\right)^{\circ 2}\Big] \\ &+ 2\begin{pmatrix}\mathbb{1} & \mathbb{1}\end{pmatrix}\Bigg[\\ &\begin{pmatrix} \Re U D_{\boldsymbol{\xi}} \Re U^T + \Im U D_{\boldsymbol{\xi}}^{-1} \Im U^T & \Re U D_{\boldsymbol{\xi}} \Im U^T - \Im U D_{\boldsymbol{\xi}}^{-1} \Re U^T \\ -\Re U D_{\boldsymbol{\xi}}^{-1} \Im U^T + \Im U D_{\boldsymbol{\xi}} \Re U^T & \Im U D_{\boldsymbol{\xi}} \Im U^T + \Re U D_{\boldsymbol{\xi}}^{-1} \Re U^T \end{pmatrix} \circ \boldsymbol{d}\boldsymbol{d}^T \\ &\Bigg]\begin{pmatrix}\mathbb{1} \\ \mathbb{1}\end{pmatrix} - \mathbb{1}, \end{aligned} \tag{6.40}$$

The displacement term from Eq. (6.38) can then be substituted and simplified by noting $A \circ \boldsymbol{u}\boldsymbol{v}^T = D_{\boldsymbol{u}} A D_{\boldsymbol{v}}$ where $(D_{\boldsymbol{v}})_{jk} = \delta_{jk} v_k$ to

$$\begin{aligned}H = \frac{1}{2}\Big[&\left(\Re U D_{\boldsymbol{\xi}} \Re U^T + \Im U D_{\boldsymbol{\xi}}^{-1} \Im U^T\right)^{\circ 2} + \left(\Re U D_{\boldsymbol{\xi}} \Im U^T - \Im U D_{\boldsymbol{\xi}}^{-1} \Re U^T\right)^{\circ 2} \\ &+ \left(-\Re U D_{\boldsymbol{\xi}}^{-1} \Im U^T + \Im U D_{\boldsymbol{\xi}} \Re U^T\right)^{\circ 2} + \left(\Im U D_{\boldsymbol{\xi}} \Im U^T + \Re U D_{\boldsymbol{\xi}}^{-1} \Re U^T\right)^{\circ 2}\Big] \\ &+ 4\big[\left(D_{\Re\boldsymbol{\gamma}} \Re U + D_{\Im\boldsymbol{\gamma}} \Im U\right) D_{\boldsymbol{\xi}} \left(\Re U^T D_{\Re\boldsymbol{\gamma}} + \Im U^T D_{\Im\boldsymbol{\gamma}}\right) \\ &\quad + \left(D_{\Re\boldsymbol{\gamma}} \Im U - D_{\Im\boldsymbol{\gamma}} \Re U\right) D_{\boldsymbol{\xi}}^{-1} \left(\Im U^T D_{\Re\boldsymbol{\gamma}} - \Re U^T D_{\Im\boldsymbol{\gamma}}\right)\big] - \mathbb{1}. \end{aligned} \tag{6.41}$$

6.4.2 Balanced squeezing

We can consider further simplifying assumptions, such as taking $\xi_j = \xi, \forall j$ to simplify Eq. (6.41). This is seen to be true for optimising the single-parameter QFI from Lang and Caves [176] and as we saw in Section 6.2.2. In this case H becomes

$$\begin{aligned}H = \frac{1}{2}\Big[&\left(e^{2\xi} \Re U \Re U^T + e^{-2\xi} \Im U \Im U^T\right)^{\circ 2} + \left(e^{2\xi} \Re U \Im U^T - e^{-2\xi} \Im U \Re U^T\right)^{\circ 2} \\ &+ \left(-e^{-2\xi} \Re U \Im U^T + e^{2\xi} \Im U \Re U^T\right)^{\circ 2} + \left(e^{2\xi} \Im U \Im U^T + e^{-2\xi} \Re U \Re U^T\right)^{\circ 2}\Big] \\ &+ 4\big[e^{2\xi} \left(D_{\Re\boldsymbol{\gamma}} \Re U + D_{\Im\boldsymbol{\gamma}} \Im U\right) \left(\Re U^T D_{\Re\boldsymbol{\gamma}} + \Im U^T D_{\Im\boldsymbol{\gamma}}\right) \\ &\quad + e^{-2\xi} \left(D_{\Re\boldsymbol{\gamma}} \Im U - D_{\Im\boldsymbol{\gamma}} \Re U\right) \left(\Im U^T D_{\Re\boldsymbol{\gamma}} - \Re U^T D_{\Im\boldsymbol{\gamma}}\right)\big] - \mathbb{1}. \end{aligned} \tag{6.42}$$

We can immediately note that imposing $U = U^*$ will substantially simplify Eq. (6.42) to

$$H = \left(\cosh 4\xi - 1\right)\mathbb{1} + 4\left[e^{2\xi} D_{\Re\boldsymbol{\gamma}}^2 + e^{-2\xi} D_{\Im\boldsymbol{\gamma}}^2\right], \tag{6.43}$$

while this is not without loss of generality this does still include balanced multi-mode beam splitters through the likes of U being a Hadamard matrix.

Equation (6.43) is now—being diagonal—trivially invertible. First we consider the limit on attainability in the homodyne regime for which our figure of merit is $\mathrm{Tr}\left(H^{-1}\right)$ before turning to the photon-counting regime.

6.4.3 Phase estimation with an external reference

The quantity $\mathrm{Tr}\left(H^{-1}\right)$ for Eq. (6.43) is straightforwardly

$$\mathrm{Tr}\left(H^{-1}\right) = \sum_{j=0}^{d} \frac{1}{\cosh 4\xi - 1 + 4\left[e^{2\xi}\left(\Re\gamma_j\right)^2 + e^{-2\xi}\left(\Im\gamma_j\right)^2\right]}. \tag{6.44}$$

Our average photon number constraint under assumptions made thus far is

$$N_{\mathrm{Tot}} = (d+1)\sinh^2\xi + \sum_j \left(\Re\gamma_j\right)^2 + \left(\Im\gamma_j\right)^2; \tag{6.45}$$

with $\xi > 0$ we see immediately that Eq. (6.44) requires $\Re\gamma = |\gamma|$. We can now minimise $\mathrm{Tr}\left(H^{-1}\right)$ subject to $\sum_j |\gamma_j|^2 = N_{\mathrm{Tot}}$ which can be solved through a Lagrange multiplier method [202]

$$L = \sum_{j=1}^{d} \frac{1}{a + c_j} + \lambda\left(C - \sum_{j=1}^{d} c_j\right), \tag{6.46}$$

which has solutions

$$c_j = -a \pm \sqrt{-\frac{1}{\lambda}}, \tag{6.47}$$

where only the positive solution gives $c_j > 0$ with $a > 0$. Solving for the constraint we then find $c_j = C/d$.

This then reduces the problem to

$$\mathrm{Tr}\left(H^{-1}\right) = \sum_{j=0}^{d} \frac{1}{\cosh 4\xi - 1 + 4e^{2\xi}|\gamma|^2}, \tag{6.48}$$

subject to $(d+1)(\sinh^2\xi + |\gamma|^2) = N_{\mathrm{Tot}}$ with product identical squeezed states as input. The remaining minimisation (modulo factors of $d+1$ is identical to the minimisation of the single-mode QCRB (or equivalent to the maximisation of the QFI) which can be solved in the same manner as the single-mode state considered in Section 6.3.2. Performing this minimisation we find the optimal state to be $|0, |\xi|\rangle^{\otimes(d+1)}$ where $|\xi| = \sinh^{-1}\left(\sqrt{\frac{N_{\mathrm{Tot}}}{d+1}}\right)$. Rewriting in terms of

N_{Tot} we get

$$\text{Tr}\left(H^{-1}\right) = \frac{(d+1)^3}{8N_{\text{Tot}}(N_{\text{Tot}}+d+1)}, \tag{6.49}$$

which, for $N_{\text{Tot}} \gg d+1$, gives us the same d^3/N^2 scaling we saw from the parallel interferometers.

Indeed comparison of Eq. (6.49) with Eq. (6.24) (over $d+1$ phases with each individual experiment using $N_{\text{Tot}}/(d+1)$ photons) yields the ratio

$$\mathcal{R}_{\text{Homodyne}} = \frac{\text{Tr}\left(H_{\text{sim}}^{-1}\right)}{\text{Tr}\left(H_{\text{ind}}^{-1}\right)} = 1, \tag{6.50}$$

showing no difference between the variance of the two schemes. This is precisely as expected as the input state is identical in each case and as the multi-phase system does not involve any interaction between the modes it is identical to parallel repetitions with the distinct phases.

6.4.4 Phase estimation without an external reference

When we move to the MZI equivalent we wish to—or indeed only allow for the possibility to—measure relative phases. This requires evaluation of $\text{Tr}\left(\mathcal{H}^{-1}\right)$ where $\varphi_j = \phi_j - \frac{1}{d+1}\sum_{k=0}^{d}\phi_k$ which we can calculate from H using Eq. (2.29). The necessary Jacobian matrix B to transform from $\{\phi_0, \phi_1, \cdots, \phi_d\}$ to $\{\bar{\varphi}, \varphi_1, \cdots, \varphi_d\}$ then requires

$$\begin{aligned} \phi_0 &= \bar{\varphi} - \sum_{j=1}^{d}\varphi_j, \\ \phi_j &= \bar{\varphi} + \varphi_j, \end{aligned} \tag{6.51}$$

where the second equation holds for $j \in \{1, \cdots, d\}$. From Eq. (6.51) we then get

$$B = \begin{pmatrix} 1 & \boldsymbol{u}^T \\ -\boldsymbol{u} & \mathbb{1}_{d\times d} \end{pmatrix}, \tag{6.52}$$

where $u_j = 1$. Whence we have

$$\mathcal{H}_{jk} = (BHB^T)_{jk} = H_{jk} - H_{j0} - H_{0k} + H_{00}, \tag{6.53}$$

where $j, k \in \{1, \cdots, d\}$ gives us the QFI matrix of $\{\varphi_1, \cdots, \varphi_d\}$ or in matrix form

$$\mathcal{H} = \breve{H} - \boldsymbol{h}\boldsymbol{u}^T - \boldsymbol{u}\boldsymbol{h}^T + H_{00}\boldsymbol{u}\boldsymbol{u}^T, \tag{6.54}$$

where $h_j = H_{0j}$ and $\breve{H}$ is the QFI matrix for $\{\phi_1, \cdots, \phi_d\}$ only. This expression allows us to find an expression for $\text{Tr}\left(\mathcal{H}^{-1}\right)$ in terms of elements of H with the

Woodbury matrix identity introduced in Eq. (1.8) such that

$$\begin{aligned}\mathrm{Tr}\left(\mathcal{H}^{-1}\right) = \mathrm{Tr}\left(\breve{H}^{-1}\right) \\ - \mathrm{Tr}\left\{\begin{pmatrix}\boldsymbol{h}^T\\ \boldsymbol{u}^T\end{pmatrix}\breve{H}^{-2}\begin{pmatrix}\boldsymbol{h} & \boldsymbol{u}\end{pmatrix}\left[\begin{pmatrix}\boldsymbol{h}^T\\ \boldsymbol{u}^T\end{pmatrix}\breve{H}^{-1}\begin{pmatrix}\boldsymbol{h} & \boldsymbol{u}\end{pmatrix} - \begin{pmatrix}H_{00} & 1\\ 1 & 0\end{pmatrix}\right]^{-1}\right\}.\end{aligned} \tag{6.55}$$

For the QFI H given by Eq. (6.43)—for an equal squeezing magnitude and real U—we have that $\boldsymbol{h} = 0$, substantially simplifying Eq. (6.55) to

$$\mathrm{Tr}\left(\mathcal{H}^{-1}\right) = \mathrm{Tr}\left(\breve{H}^{-1}\right) - \frac{H_{00}\boldsymbol{u}^T\breve{H}^{-2}\boldsymbol{u}}{1 - H_{00}\boldsymbol{u}^T\breve{H}^{-1}\boldsymbol{u}}, \tag{6.56}$$

With diagonal $\breve{H}$—as in Eq. (6.43)—this becomes

$$\begin{aligned}\mathrm{Tr}\left(\mathcal{H}^{-1}\right) &= \sum_{j=1}^{d}\frac{1}{H_{jj}} - \frac{H_{00}}{1 + H_{00}\sum\limits_{j=1}^{d}\frac{1}{H_{jj}}}\sum_{j=1}^{d}\frac{1}{H_{jj}^2} \\ &= \sum_{j=1}^{d}\frac{1}{H_{jj}} - \left(\sum_{j=0}^{d}\frac{1}{H_{jj}}\right)^{-1}\sum_{j=1}^{d}\frac{1}{H_{jj}^2},\end{aligned} \tag{6.57}$$

with $H_{jj} = \cosh 4\xi - 1 + 4\left[e^{2\xi}(\Re\gamma_j)^2 + e^{-2\xi}(\Im\gamma_j)^2\right]$, while our average particle number constraint is still given by Eq. (6.45). The second term no longer obviously decreases in size with increasing H_{jj}, we first consider $H_{jj} = H_{jj}(x_j)$ and evaluate

$$\frac{\partial}{\partial x_j}\mathrm{Tr}\left(\mathcal{H}^{-1}\right) = \frac{1}{H_{jj}^2}\frac{\partial H_{jj}}{\partial x_j}\left[-1 + \frac{2}{H_{jj}}\left(\sum_{k=0}^{d}\frac{1}{H_{kk}}\right)^{-1} - \left(\sum_{k=0}^{d}\frac{1}{H_{kk}}\right)^{-2}\sum_{k=1}^{d}\frac{1}{H_{kk}^2}\right], \tag{6.58}$$

for $j \in \{1, \cdots, d\}$ and

$$\frac{\partial}{\partial x_0}\mathrm{Tr}\left(\mathcal{H}^{-1}\right) = -\frac{1}{H_{00}^2}\frac{\partial H_{00}}{\partial x_0}\left(\sum_{k=0}^{d}\frac{1}{H_{kk}}\right)^{-2}\sum_{k=1}^{d}\frac{1}{H_{kk}^2}, \tag{6.59}$$

Equation (6.59) gives us that $\mathrm{Tr}\left(\mathcal{H}^{-1}\right)$ is minimised by maximising H_{00} as the coefficient of $\partial H_{00}/\partial x_0$ is necessarily positive. Equation (6.58) is less obvious,

we can rewrite it as

$$\frac{\partial}{\partial x_j}\operatorname{Tr}\left(\mathcal{H}^{-1}\right) = -\frac{1}{H_{jj}^2}\frac{\partial H_{jj}}{\partial x_j}\left\{\left[1-\frac{1}{H_{jj}}\left(\sum_{k=0}^{d}\frac{1}{H_{kk}}\right)^{-1}\right]^2 + \left(\sum_{k=0}^{d}\frac{1}{H_{kk}}\right)^{-2}\sum_{k=1,k\neq j}^{d}\frac{1}{H_{kk}^2}\right\}, \tag{6.60}$$

from which we can then identify that $\operatorname{Tr}\left(\mathcal{H}^{-1}\right)$ is monotonically decreasing with H_{jj}. Hence $\gamma_j = |\gamma_j|$ maximises H_{jj} with respect to $\arg\gamma_j$ and therefore minimises $\operatorname{Tr}\left(\mathcal{H}^{-1}\right)$. Then we rewrite H_{jj} in terms of $N_j = \sinh^2|\xi_j| + |\gamma_j|^2$ and $N_{\gamma_j} = |\gamma_j|^2$—in the same manner as Eq. (6.22)—as

$$H_{jj} = 8N_j(N_j+1) - 8N_{|\gamma_j|}\left[\frac{1}{2} + N_j - \sqrt{\left(N_j - N_{|\gamma_j|}\right)\left(N_j+1-N_{|\gamma_j|}\right)}\right], \tag{6.61}$$

which—again in the same manner as Eq. (6.22) and in minimising $\operatorname{Tr}\left(H^{-1}\right)$—is monotonically increasing with decreasing $N_{|\gamma_j|}$, which leads us to the state $|\xi\rangle^{\otimes(d+1)}$ with $\xi = \sinh^{-1}[\sqrt{N_{\mathrm{Tot}}/(d+1)}]$ as optimal within our earlier assumptions of $|\xi_j| = |\xi|$ and $U^* = U$. The resultant bound is then

$$\operatorname{Tr}\left(\mathcal{H}^{-1}\right) = \frac{d^2(d+1)}{8N_{\mathrm{Tot}}(N_{\mathrm{Tot}}+d+1)}, \tag{6.62}$$

displaying the same d^3/N^2 scaling as Eq. (6.49), and the $d = 1$ case gives Eq. (6.19).

If we compare Eq. (6.62) ($\mathcal{H}_{\mathrm{sim}}$) and Eq. (6.19) using $N_{\mathrm{Tot}}/(d+1)$ particles in each instance of the single phase MZI ($\mathcal{H}_{\mathrm{ind}}$) we find

$$\mathcal{R}_{\mathrm{PNRD}} = \frac{\operatorname{Tr}\left(\mathcal{H}_{\mathrm{sim}}^{-1}\right)}{\operatorname{Tr}\left(\mathcal{H}_{\mathrm{ind}}\right)} = \frac{2d(N_{\mathrm{Tot}}+d+1)}{(d+1)(N_{\mathrm{Tot}}+2d)} \geq \frac{d+1}{2d}, \tag{6.63}$$

showing a potential improvement in precision but bounded by a factor of 2, again falling short of the order d scaling of the multi-mode N00N states of Humphreys et al. [13].

6.5 Attainability

6.5.1 Existence of saturating measurement

In Section 2.5.2 we identified Eq. (2.36) as a necessary condition for the existence of a POVM which saturates the QCRB [39], moreover for pure states there exists a POVM which attains the bound through identifying SLD operators which

commute [37].

For a state

$$|\psi_{\boldsymbol{\phi}}\rangle\langle\psi_{\boldsymbol{\phi}}| = e^{i\sum_j \phi_j \hat{g}_j}|\psi_0\rangle\langle\psi_0| e^{-i\sum_j \phi_j \hat{g}_j}, \tag{6.64}$$

where the generators $\{\hat{g}_j\}$ all commute as $[\hat{g}_j, \hat{g}_k] = 0$, we find from Eq. (2.27) that the SLD operator is

$$\mathcal{L}_j = 2i(\hat{g}_j |\psi_{\boldsymbol{\phi}}\rangle\langle\psi_{\boldsymbol{\phi}}| - |\psi_{\boldsymbol{\phi}}\rangle\langle\psi_{\boldsymbol{\phi}}| \hat{g}_j), \tag{6.65}$$

where we use the commutativity of the generators to simplify the derivatives. For non-commuting generators the form of this weak commutativity is more complicated [182]. The weak commutativity condition is then

$$\mathrm{Tr}\left(|\psi_{\boldsymbol{\phi}}\rangle\langle\psi_{\boldsymbol{\phi}}|\left[\mathcal{L}_j, \mathcal{L}_k\right]\right) = -4\langle\psi_{\boldsymbol{\phi}}|[[\hat{g}_j, |\psi_{\boldsymbol{\phi}}\rangle\langle\psi_{\boldsymbol{\phi}}|], [\hat{g}_k, |\psi_{\boldsymbol{\phi}}\rangle\langle\psi_{\boldsymbol{\phi}}|]]|\psi_{\boldsymbol{\phi}}\rangle, \tag{6.66}$$

which we can simplify by noting

$$[\hat{g}_j, |\psi_{\boldsymbol{\phi}}\rangle\langle\psi_{\boldsymbol{\phi}}|]|\psi_{\boldsymbol{\phi}}\rangle = (\hat{g}_j - \langle\psi_{\boldsymbol{\phi}}|\hat{g}_j|\psi_{\boldsymbol{\phi}}\rangle)|\psi_{\boldsymbol{\phi}}\rangle, \tag{6.67}$$

which effectively uses $\rho^2 = \rho$. Then we arrive at

$$\begin{aligned}\mathrm{Tr}\left(|\psi_{\boldsymbol{\phi}}\rangle\langle\psi_{\boldsymbol{\phi}}|\left[\mathcal{L}_j, \mathcal{L}_k\right]\right) &= -4\langle\psi_{\boldsymbol{\phi}}|[\hat{g}_j - \langle\psi_{\boldsymbol{\phi}}|\hat{g}_j|\psi_{\boldsymbol{\phi}}\rangle, \hat{g}_k - \langle\psi_{\boldsymbol{\phi}}|\hat{g}_j|\psi_{\boldsymbol{\phi}}\rangle]|\psi_{\boldsymbol{\phi}}\rangle \\ &= 0.\end{aligned} \tag{6.68}$$

We then proceed to discuss whether these POVMs include experimentally feasible strategies such as homodyne-based detection in Section 6.5.2, and photon counting in Section 6.5.3 or may require additional resources.

6.5.2 Homodyne detection

For the state $|0,\xi\rangle^{\otimes(d+1)}$ we identifed in Sections 6.4.3 and 6.4.4 we now demonstrate the attainability of the QCRB with homodyne detection, which was introduced in Section 3.4.3. As this involves product states with each mode having a different parameter encoding the proof for single phase estimation with a single-mode Gaussian state in Monras [201] is technically sufficient. For completeness we explicitly demonstrate the multi-parameter QCRB can be attained with the $|0,\xi\rangle^{\otimes(d+1)}$ squeezed vacuum state through a homodyne scheme illustrated in Fig. 6.6.

We first demonstrate that homodyne measurements can be used to estimate the parameters $\{\phi_j\}$ encoded in the state $|\xi_0, \xi_1, \cdots, \xi_d\rangle$ by the unitary $e^{i\sum_{j=0}^{d}\phi_j\hat{n}_j}$. The $(d+1)\times(d+1)$ QFI matrix in this case is $H_{jk} = 2\sinh^2 2|\xi_j|$. The covariance

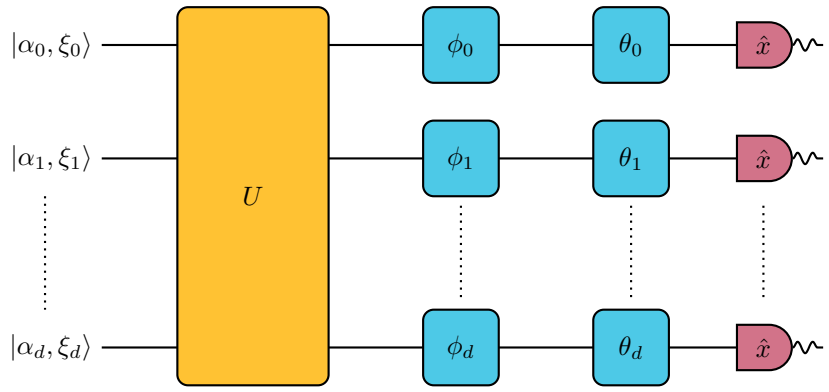

Figure 6.6: Multi-mode pure Gaussian state incident on multiple single phase shifts followed by a homodyne detection scheme measuring each $\hat{x}_j$ quadrature.

matrix is then

$$\sigma = \bigoplus_{j=0}^{d} \begin{pmatrix} \cosh 2|\xi_j| + \sinh 2|\xi_j| \cos 2\phi_j & \sinh 2|\xi_j| \sin 2\phi_j \\ \sinh 2|\xi_j| \sin 2\phi_j & \cosh 2|\xi_j| - \sinh 2|\xi_j| \cos 2\phi_j \end{pmatrix}, \tag{6.69}$$

we then apply a rotation θ_j in each mode and perform homodyne on the $\hat{x}_j$ quadrature (measuring the $\hat{x}_j(\theta_j) = \hat{x}_j \cos\theta_j + \hat{p}_j \sin\theta_j$ quadrature) to give the measured covariance matrix

$$\Sigma = \bigoplus_{j=0}^{d} \Big(\cosh 2|\xi_j| + \sinh 2|\xi_j| \cos 2(\phi_j + \theta_j) \Big), \tag{6.70}$$

from which we can calculate—with means being zero due to the use of squeezed vacuum—the FI matrix with Eq. (2.18). As Σ is diagonal and $\partial_j \Sigma_k = 0, \forall j \neq k$ we have immediately that $\Sigma^{-1}\partial_{\phi_j}\Sigma\Sigma^{-1}\partial_{\phi_k}\Sigma = 0, \forall j \neq k$ giving us a diagonal FI matrix. The remaining diagonal terms require

$$(\Sigma^{-1}\partial_{\phi_j}\Sigma\Sigma^{-1}\partial_{\phi_j}\Sigma)_{kl} = \delta_{jk}\delta_{jl} \frac{4\sin^2[2(\phi_j + \theta_j)]\sinh^2 2|\xi_j|}{\left(\cosh 2|\xi_j| + \sinh 2|\xi_j| \cos 2(\phi_j + \theta_j)\right)^2}, \tag{6.71}$$

whence we have

$$\mathrm{Tr}\left(F^{-1}_{\text{Homodyne}}\right) = \sum_j \frac{\cosh 2|\xi_j| + \sinh 2|\xi_j| \cos 2(\phi_j + \theta_j)}{2\sin^2[2(\phi_j + \theta_j)]\sinh^2 2|\xi_j|}. \tag{6.72}$$

Equation (6.72) is minimised by

$$\theta_j = -\phi_j - \pi/2 + \tan^{-1}\left(\frac{1}{\sinh 2|\xi_j|}\right), \tag{6.73}$$

to give

$$\mathrm{Tr}\left(F^{-1}_{\mathrm{Homodyne}}\right) = \sum_j \frac{1}{2\sinh^2 2|\xi_j|}, \tag{6.74}$$

or in terms of FI matrix elements

$$(F_{\mathrm{Homodyne}})_{jk} = 2\delta_{jk}\sinh^2 2|\xi_j|, \tag{6.75}$$

therefore attaining the multi-parameter QCRB (although, as highlighted earlier, in a trivial extension of the single-mode/single-phase proof given the states are separable and each parameter is local to a different uncorrelated mode).

This argument demonstrates, technically, that the relative phase shift bound $\mathrm{Tr}\left(\mathcal{H}^{-1}\right)$ can also be obtained with homodyne. However if homodyne were to be used in this scenario a slightly higher precision would obtained by removing the reference mode and estimating d phases shifts relative to the homodyne reference, rather than d phase shifts relative to the reference mode. For the $\{\varphi_j\}$ parameter set one anticipates instead a photon counting strategy which does not involve the introduction of additional resources.

6.5.3 Photon counting

While we argued that the QFI $H(\boldsymbol{\phi})$ was attainable with homodyne detection this requires the introduction of an external LO. Not only is this a potential extra resource but this reference must be much more powerful than the state upon which the measurement is performed [74]. Instead this extra resource could be avoided with a scheme using only linear optics and PNRDs such as that illustrated in Fig. 6.7, however such a scheme may not reach the QCRB.

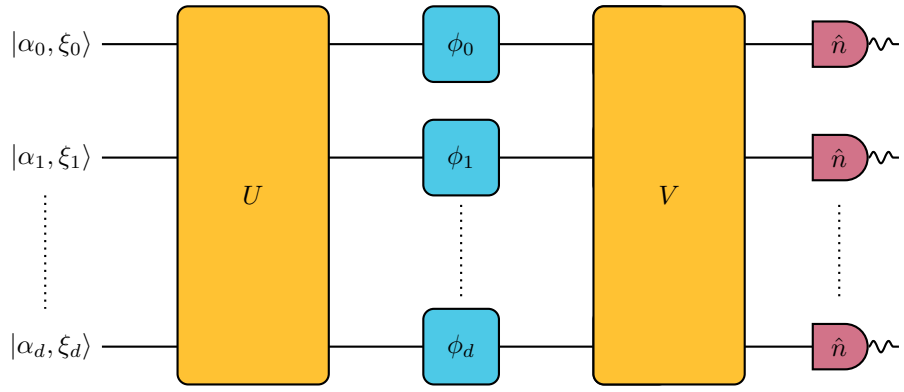

Figure 6.7: Generic multi-mode pure Gaussian state incident on multiple single phase shifts followed by a second multi-mode beam splitter and photon number resolving detectors.

In general calculation of the probability of photon counting events is not particularly easy to handle—this is the premise of the quantum supremacy candidate Gaussian Boson sampling [203, 204]—although thermal states or coherent states can be handled, the multi-mode squeezed light[7] we are interested in is not so simple [205].

The potential of photon-counting methods to attain the QFI $\mathcal{H}$ remains an outstanding problem with limited—given Eq. (6.63)—value in exploring for the pure state case alone in comparison to MZIs.

6.6 Conclusions

By calculation of the multi-parameter QCRB for a system with an arbitrary number of phases we saw that likely generalisations of MZIs with Gaussian states do not achieve any superior scaling from simultaneous estimation of multiple phases and that in absolute terms no more than a factor of 2 improvement is gained. With the addition of an external phase reference in the form of an LO that advantage vanished entirely, and the simultaneous and parallel phase estimation schemes are identical.

Obvious extensions to this work include the evaluation of the same QCRBs for thermally squeezed coherent states—the most general input states which remain Gaussian—and to include loss (or thermal loss) occurring after the phase shifts which would also capture the effect of detectors without unit efficiency. While the pure state case is limited to a factor of 2 improvement the potentially increased resilience of Gaussian states to noise may merit further investigation with highly noisy environments. However whether any photon counting strategy attains the QFI $\mathcal{H}$ remains open and necessary both for the factor of 2 improvement and for any extension to non-unitary dynamics.

For the sake of completeness it would be desirable to extend our analysis for pure states to eliminate the assumptions i. $|\xi_j| = |\xi|, \forall j$ and ii. $U = U^*$. While numerical evidence suggested no significant potential for improvement and these assumptions are clearly compatible with the obvious extensions of the MZI results, a definitive argument remains desirable.

The results in this chapter—along with You et al. [191] which look at one obvious multi-mode extension of the Holland-Burnett states—seem to show a

[7] While the state after the phases may be a product squeezed state $\bigotimes_{j=0}^{d} ||\xi|e^{i\phi_j}\rangle$ photon counting at this point gives us statistics dependent only on $|\xi|$ as the phase shift $e^{i\sum_{j=0}^{d}\phi_j\hat{n}_j}$ leaves eigenstates of $\hat{n}_{\text{Tot}}$ invariant. Instead it is necessary to have a non-trivial second multi-mode beam splitter to interfere the modes such that the phase shifts will affect the photon number distributions.

substantial divergence between the Holland-Burnett, squeezed vacuum, and N00N states which all—at the single parameter level—achieve the Heisenberg scaling [176]. While Humphreys et al. [13] generalise the N00N state to achieve an improved scaling in parameter number when employed for simultaneous phase estimation, this improvement is not realised by multi-mode generalisations of Gaussian and Holland-Burnett states [DB1, 191]. This demonstrates the greater subtleties of multi-parameter estimation and raises the question of what property of the multi-mode N00N state gives it this superior precision. Moreover this identifies a limitation of Gaussian states in metrology—alongside results in computation [206, 207], communication [208–210], and wider resource theories [211]—though only appearing when multi-parameter estimation is considered.

One implication is that non-Gaussian states still have promise for simultaneous phase estimation which may resurrect the Humphreys et al. [13] scaling. It is possible that close to Gaussian states, such as photon-added/photon-subtracted Gaussian states [212], indeed post-selective measurements on two-mode Gaussian states can produce single-mode states with superior QFI for single phase estimation [213].

Finally, while we sought to consider only the physically measurable phase parameters $\{\varphi_j\}$ for measurements without an external phase reference, this does not guarantee that we avoid all problems of unknown and unmeasurable quantities—in particular the "global"[8] phase $\bar{\varphi}$—further analysis with input states or nuisance parameter treatments to capture this would be prudent.

[8]This is not a global phase in the true sense, hence homodyne detection is able to circumvent this, but cannot be detected through photon counting without the use of additional modes.

Chapter 7

Conclusions

This thesis has explored a range of quantum sensing applications of mechanical, optical, and optomechanical systems.

In Chapter 4 we looked at the limit at which diffusion could be estimated, with particular focus on the space-based proposal MAQRO [108, 109]. We identified potential measurements which would enable superior resolution of such a diffusion rate, potentially by many orders of magnitude (see Fig. 4.8 for example) over simply observing the final position of the particle. We further found that squeezing could improve the smallest discernable diffusion rates across the considered measurements. This squeezing could compensate for a reduced free-fall time t which is one of the most significant limiting factors in the experimental proposal of MAQRO [110].

In Chapter 5 we looked at the necessary framework to calculate the fundamental quantum limits of multi-mode optomechanical sensors such as laser-interferometric GW detectors. We analytically calculated fundamental bounds, as well as bounds for homodyne detection (which encompasses frequency-dependent and signal quadrature homodyne), for systems with an arbitrary number of carriers including radiation-pressure effects, external squeezing, and optical loss. We argued generally that the optimal configuration was always a single-mode interferometer. From these bounds we were able to calculate optimal squeezing and homodyne angles. The optical loss model demonstrates—in contrast to conventional wisdom [175, 214]—a noise source which does not simply reduce to the SNL in energy but reaches a maximum at a given value, through a revival of the radiation-pressure term at high optical powers when loss is non-zero.

In Chapter 6 we looked at simultaneous phase estimation. We calculated multi-parameter bounds for a general pure Gaussian input state. Exploring the possibility of optimising over Gaussian states we found squeezed vacuum—the same squeezed vacuum which was optimal for single-phase estimation [176,

201]—to be favourable. However this system has no substantial advantage over separate individual phase estimation schemes with no more than a factor of 2 improvement in precision being accessible for a fixed total energy constraint.

Noise typically impedes quantum sensing [175, 214, 215]; including the effects of noise processes in models provides more realistic bounds and can affect the optimal state [216]. Already Chapter 5 captures noise entering due to radiation-pressure effects which are missed by a simpler model of the interferometer [144]; further advances could consider thermal loss channels—which may be seen in interferometers operating at lower optical frequencies—or accounting more accurately for loss in the different elements of the sensor in the manner of Kimble et al. [121]. Capturing optical (thermal) loss or non-unit detector efficiencies would enhance the analysis of Chapter 6, possibly leading to different input states minimising the CRB or improved scaling for simultaneous estimation under noise. Accounting for environmental decoherence effects in addition to the intrinsic decoherence posited by collapse theories—such as environmental processes which induce momentum diffusion [111]—would enhance the analysis of Chapter 4. Throughout this thesis we have assumed the ability to perfectly perform squeezing; in practise there may be some uncertainty in the exact quadrature angle squeezed which would limit precision, however modelling such noise would require a non-Gaussian analysis.

Furthermore unknown parameters such as noise strengths or reference phases can affect the estimation strategy without being desirable to estimate themselves. The impact of such 'nuisance' parameters—being unknown or unidentifiable—can be captured through statistical analyses [31] which can be applied to quantum lower bounds [198, 199] where they may have appreciable effects [193, 197, 217].

The CRB relies on the existence of an efficient estimator, in general the search for an efficient estimator demands the asymptotic limit in the number of repetitions of the ML estimator [31–33]. In practise many repetitions are required to achieve the CRB through the ML estimator [218], in certain experiments—such as those using the states of Rivas and Luis [219]—approaching the CRB through the ML estimator may require a prohibitive number of repetitions to reach the asymptotic limit [220, 221]. To properly handle this, Bayesian analyses—which take account of a prior knowledge—are called for [222, 223]; these are accompanied by Bayesian alternatives to the QCRB [220, 224, 225] which unfortunately lack the tightness guarantees of the QCRB. While—in contrast to the states of Rivas and Luis [219]—there may be no reason to anticipate that Gaussian states display any significantly delayed convergence to the asymptotic limit, the convergence rate may be significant for problems like imaging delicate samples [226]. In the event that only a certain number of repetitions can be carried out, what was the optimal state in the asymptotic

limit may not remain so.

It is important to note that while Gaussian states are known to achieve Heisenberg scaling for phase estimation [176], this is not to say they are best for all metrological endeavours. Many of the proposals which would build on the likes of the MAQRO experiment we dealt with in Chapter 4 similarly utilise non-Gaussian phenomena [104, 105, 109, 227]. Chapter 6 in particular demonstrates a limitation of Gaussian states in multi-parameter estimation which non-Gaussian states do not suffer from [13]. A similar limitation is observed in quantum computing with Gaussian systems [206, 207] yet with the addition to the gate set of the cubic phase gate, universal quantum computing can be achieved. While states which exist in a finite subspace of the Fock space can be handled (such states are only technically CV systems as they can also be cast as qudit systems), and similarly general expressions can be found for some certain pure state problems [145, 176, 212], efforts to derive analytic results for general (mixed) non-Gaussian CV states have (understandably) thus far been limited. Furthermore reasonable noise models, such as dephasing, drive Gaussian states to non-Gaussian states whose precision can no longer be captured with the tools of Gaussian quantum metrology.

Bibliography

[DB1] C. N. Gagatsos, D. Branford, and A. Datta, "Gaussian systems for quantum-enhanced multiple phase estimation", Physical Review A **94**, 042342 (2016) (cit. on pp. 78, 98).

[DB2] D. Branford, O. C. O. Dahlsten, and A. J. P. Garner, "On defining the Hamiltonian beyond quantum theory", Foundations of Physics **48**, 982–1006 (2018).

[DB3] D. Branford, H. Miao, and A. Datta, "Fundamental quantum limits of multicarrier optomechanical sensors", Physical Review Letters **121**, 110505 (2018) (cit. on pp. 54, 55, 63).

[DB4] D. Branford, C. N. Gagatsos, J. Grover, A. J. Hickey, and A. Datta, "Quantum enhanced estimation of diffusion", Physical Review A **100**, 022129 (2019) (cit. on p. 33).

[1] L. Essen and J. V. L. Parry, "An Atomic Standard of Frequency and Time Interval: A Cæsium Resonator", Nature **176**, 280 (1955) (cit. on p. 1).

[2] A. A. Michelson and E. W. Morley, "On the relative motion of the Earth and the luminiferous ether", American Journal of Science **s3-34**, 333–345 (1887) (cit. on p. 1).

[3] C. M. Caves, "Quantum-mechanical noise in an interferometer", Physical Review D **23**, 1693–1708 (1981) (cit. on pp. 1, 54, 61, 76, 77).

[4] J. J. Bollinger, W. M. Itano, D. J. Wineland, and D. J. Heinzen, "Optimal frequency measurements with maximally correlated states", Physical Review A **54**, R4649–R4652 (1996) (cit. on pp. 1, 5, 77).

[5] R. Schnabel, J. Harms, K. A. Strain, and K. Danzmann, "Squeezed light for the interferometric detection of high-frequency gravitational waves", Classical and Quantum Gravity **21**, S1045 (2004) (cit. on p. 1).

[6] R. Schnabel, "Squeezed states of light and their applications in laser interferometers", Physics Reports **684**, 1–51 (2017) (cit. on pp. 1, 54, 76, 77).

[7] M. Malnou, D. A. Palken, B. M. Brubaker, L. R. Vale, G. C. Hilton, and K. W. Lehnert, "Squeezed Vacuum Used to Accelerate the Search for a Weak Classical Signal", Physical Review X **9**, 021023 (2019) (cit. on p. 1).

[8] G. Brida, M. Genovese, and I. R. Berchera, "Experimental realization of sub-shot-noise quantum imaging", Nature Photonics **4**, 227–230 (2010) (cit. on p. 1).

[9] M. A. Taylor, J. Janousek, V. Daria, J. Knittel, B. Hage, H.-A. Bachor, and W. P. Bowen, "Subdiffraction-Limited Quantum Imaging within a Living Cell", Physical Review X **4**, 011017 (2014) (cit. on pp. 1, 54).

[10] A. Bassi and G. Ghirardi, "Dynamical reduction models", Physics Reports **379**, 257–426 (2003) (cit. on pp. 1, 32).

[11] A. Bassi, K. Lochan, S. Satin, T. P. Singh, and H. Ulbricht, "Models of wave-function collapse, underlying theories, and experimental tests", Reviews of Modern Physics **85**, 471–527 (2013) (cit. on pp. 1, 32, 50).

[12] C. M. Caves, "Quantum-Mechanical Radiation-Pressure Fluctuations in an Interferometer", Physical Review Letters **45**, 75–79 (1980) (cit. on pp. 1, 55).

[13] P. C. Humphreys, M. Barbieri, A. Datta, and I. A. Walmsley, "Quantum Enhanced Multiple Phase Estimation", Physical Review Letters **111**, 070403 (2013) (cit. on pp. 2, 77, 78, 82, 85, 86, 93, 98, 101).

[14] M. A. Nielsen and I. L. Chuang, *Quantum Computation and Quantum Information: 10th Anniversary Edition* (Cambridge University Press, Dec. 9, 2010), 709 pp. (cit. on pp. 2, 3, 60).

[15] C. Gardiner and P. Zoller, *Quantum Noise - A Handbook of Markovian and Non-Markovian*, Springer Series in Synergetics (Springer, 2004) (cit. on p. 2).

[16] H.-P. Breuer and F. Petruccione, *The Theory of Open Quantum Systems* (Oxford University Press, 2002) (cit. on p. 3).

[17] W. W. Hager, "Updating the Inverse of a Matrix", SIAM Review **31**, 221–239 (1989) (cit. on p. 3).

[18] R. A. Fisher, "Theory of Statistical Estimation", Mathematical Proceedings of the Cambridge Philosophical Society **22**, 700–725 (1925) (cit. on p. 5).

[19] U. Dorner, "Quantum frequency estimation with trapped ions and atoms", New Journal of Physics **14**, 043011 (2012) (cit. on p. 5).

[20] J. M. Taylor, P. Cappellaro, L. Childress, L. Jiang, D. Budker, P. R. Hemmer, A. Yacoby, R. Walsworth, and M. D. Lukin, "High-sensitivity diamond magnetometer with nanoscale resolution", Nature Physics **4**, 810–816 (2008) (cit. on p. 5).

[21] LIGO Scientific Collaboration, "Advanced LIGO", Classical and Quantum Gravity **32**, 074001 (2015) (cit. on pp. 5, 54, 55, 61).

[22] D. V. Martynov et al., "Sensitivity of the Advanced LIGO detectors at the beginning of gravitational wave astronomy", Physical Review D **93**, 112004 (2016) (cit. on pp. 5, 54).

[23] Q. Li, C. Xue, J.-P. Liu, J.-F. Wu, S.-Q. Yang, C.-G. Shao, L.-D. Quan, W.-H. Tan, L.-C. Tu, Q. Liu, H. Xu, L.-X. Liu, Q.-L. Wang, Z.-K. Hu, Z.-B. Zhou, P.-S. Luo, S.-C. Wu, V. Milyukov, and J. Luo, "Measurements of the gravitational constant using two independent methods", Nature **560**, 582 (2018) (cit. on p. 5).

[24] M. Paris and J. Řeháček, eds., *Quantum State Estimation*, Vol. 649, Lecture Notes in Physics (Springer Berlin Heidelberg, Berlin, Heidelberg, 2004) (cit. on p. 5).

[25] C. W. Helstrom, *Quantum Detection and Estimation Theory* (Academic Press, New York, 1976), 330 pp. (cit. on pp. 5, 10).

[26] A. Holevo, *Probabilistic and Statistical Aspects of Quantum Theory* (Edizioni della Normale, Pisa, 2011) (cit. on pp. 5, 10, 13).

[27] C. W. Helstrom, "Minimum mean-squared error of estimates in quantum statistics", Phys. Lett. A **25**, 101–102 (1967) (cit. on p. 5).

[28] S. L. Braunstein and C. M. Caves, "Statistical distance and the geometry of quantum states", Phys. Rev. Lett. **72**, 3439–3443 (1994) (cit. on pp. 5, 13, 14, 77).

[29] G. Tóth and I. Apellaniz, "Quantum metrology from a quantum information science perspective", Journal of Physics A: Mathematical and Theoretical **47**, 424006 (2014) (cit. on pp. 6, 11, 12, 14, 16).

[30] R. Demkowicz-Dobrzański, M. Jarzyna, and J. Kołodyński, "Quantum Limits in Optical Interferometry", in *Progress in Optics*, Vol. 60, edited by E. Wolf (Elsevier, 2015), pp. 345–435 (cit. on pp. 6, 55, 76, 78, 79).

[31] E. L. Lehmann and G. Casella, *Theory of Point Estimation*, Springer Texts in Statistics (Springer-Verlag, New York, 1998) (cit. on pp. 7, 8, 10, 100).

[32] D. J. Olive, *Statistical Theory and Inference* (Springer International Publishing, Cham, 2014) (cit. on pp. 7, 8, 10, 100).

[33] S. M. Kay, *Fundamentals of Statistical Signal Processing: Estimation theory* (Prentice-Hall PTR, 1998), 595 pp. (cit. on pp. 8, 10, 12, 27, 65, 100).

[34] B. Porat and B. Friedlander, "Computation of the exact information matrix of Gaussian time series with stationary random components", IEEE Transactions on Acoustics, Speech and Signal Processing **34**, 118–130 (1986) (cit. on pp. 10, 27).

[35] M. G. A. Paris, "Quantum estimation for quantum technology", International Journal of Quantum Information **07**, 125–137 (2009) (cit. on pp. 11–14, 16, 87).

[36] M. Szczykulska, T. Baumgratz, and A. Datta, "Multi-parameter quantum metrology", Advances in Physics: X **1**, 621–639 (2016) (cit. on p. 11).

[37] K. Matsumoto, "A new approach to the Cramér-Rao-type bound of the pure-state model", Journal of Physics A: Mathematical and General **35**, 3111 (2002) (cit. on pp. 13, 14, 94).

[38] M. Hayashi, *Asymptotic Theory of Quantum Statistical Inference: Selected Papers* (World Scientific, Singapore, Feb. 2005), 560 pp. (cit. on pp. 13, 14).

[39] S. Ragy, M. Jarzyna, and R. Demkowicz-Dobrzański, "Compatibility in multiparameter quantum metrology", Physical Review A **94**, 052108 (2016) (cit. on pp. 13, 14, 93).

[40] J. Suzuki, "Information Geometrical Characterization of Quantum Statistical Models in Quantum Estimation Theory", Entropy **21**, 703 (2019) (cit. on pp. 13, 14).

[41] M. D. Vidrighin, G. Donati, M. G. Genoni, X.-M. Jin, W. S. Kolthammer, M. S. Kim, A. Datta, M. Barbieri, and I. A. Walmsley, "Joint estimation of phase and phase diffusion for quantum metrology", Nature Communications **5**, 3532 (2014) (cit. on pp. 13, 33, 77).

[42] E. Roccia, I. Gianani, L. Mancino, M. Sbroscia, F. Somma, M. G. Genoni, and Marco Barbieri, "Entangling measurements for multiparameter estimation with two qubits", Quantum Science and Technology **3**, 01LT01 (2018) (cit. on p. 13).

[43] M. Parniak, S. Borówka, K. Boroszko, W. Wasilewski, K. Banaszek, and R. Demkowicz-Dobrzański, "Beating the Rayleigh Limit Using Two-Photon Interference", Physical Review Letters **121**, 250503 (2018) (cit. on p. 13).

[44] O. E. Barndorff-Nielsen and R. D. Gill, "Fisher information in quantum statistics", Journal of Physics A: Mathematical and General **33**, 4481 (2000) (cit. on p. 14).

[45] A. Fujiwara, "Strong consistency and asymptotic efficiency for adaptive quantum estimation problems", Journal of Physics A: Mathematical and General **39**, 12489 (2006) (cit. on p. 14).

[46] J. Kahn and M. Guţă, "Local Asymptotic Normality for Finite Dimensional Quantum Systems", Communications in Mathematical Physics **289**, 597–652 (2009) (cit. on p. 14).

[47] R. D. Gill and M. I. Guţă, "On asymptotic quantum statistical inference", in *Institute of Mathematical Statistics Collections* (Institute of Mathematical Statistics, Beachwood, Ohio, USA, 2013), pp. 105–127 (cit. on p. 14).

[48] K. Yamagata, A. Fujiwara, and R. D. Gill, "Quantum local asymptotic normality based on a new quantum likelihood ratio", The Annals of Statistics **41**, 2197–2217 (2013) (cit. on p. 14).

[49] L. Pezzè, M. A. Ciampini, N. Spagnolo, P. C. Humphreys, A. Datta, I. A. Walmsley, M. Barbieri, F. Sciarrino, and A. Smerzi, "Optimal Measurements for Simultaneous Quantum Estimation of Multiple Phases", Physical Review Letters **119**, 130504 (2017) (cit. on pp. 14, 86).

[50] W. Gorecki, S. Zhou, L. Jiang, and R. Demkowicz-Dobrzanski, "Quantum error correction in multi-parameter quantum metrology", (2019), arXiv:1901.00896 [quant-ph] (cit. on p. 14).

[51] M. G. Genoni, L. Lami, and A. Serafini, "Conditional and unconditional Gaussian quantum dynamics", Contemporary Physics **57**, 331–349 (2016) (cit. on p. 16).

[52] A. Serafini, *Quantum Continuous Variables : A Primer of Theoretical Methods* (CRC Press, Boca Raton, July 20, 2017) (cit. on pp. 16–24, 26–30, 46, 60).

[53] G. Adesso, S. Ragy, and A. R. Lee, "Continuous Variable Quantum Information: Gaussian States and Beyond", Open Systems & Information Dynamics **21**, 1440001 (2014) (cit. on pp. 16, 18–21, 23, 24, 30, 60).

[54] A. Monras, "Phase space formalism for quantum estimation of Gaussian states", (2013), arXiv:1303.3682 [quant-ph] (cit. on pp. 16, 20, 27, 28, 30, 46, 62).

[55] Y. Gao and H. Lee, "Bounds on Quantum Multiple-Parameter Estimation with Gaussian State", The European Physical Journal D **68**, 347 (2014) (cit. on pp. 16, 27).

[56] D. Šafránek, A. R. Lee, and I. Fuentes, "Quantum parameter estimation using multi-mode Gaussian states", New Journal of Physics **17**, 073016 (2015) (cit. on pp. 16, 27, 62).

[57] S. M. Barnett and P. M. Radmore, *Methods in Theoretical Quantum Optics* (OUP Oxford, Nov. 14, 2002), 292 pp. (cit. on pp. 17, 20, 21).

[58] A. Ferraro, S. Olivares, and M. G. A. Paris, "Gaussian states in continuous variable quantum information", (2005), arXiv:`quant-ph/0503237` (cit. on pp. 18, 20, 21, 24, 30, 31, 57).

[59] F. Nicacio, R. N. P. Maia, F. Toscano, and R. O. Vallejos, "Phase space structure of generalized Gaussian cat states", Physics Letters A **374**, 4385–4392 (2010) (cit. on pp. 20, 26).

[60] M. Reck, A. Zeilinger, H. J. Bernstein, and P. Bertani, "Experimental realization of any discrete unitary operator", Physical Review Letters **73**, 58–61 (1994) (cit. on p. 22).

[61] W. R. Clements, P. C. Humphreys, B. J. Metcalf, W. S. Kolthammer, and I. A. Walmsley, "Optimal design for universal multiport interferometers", Optica **3**, 1460–1465 (2016) (cit. on p. 22).

[62] S. L. Braunstein, "Squeezing as an irreducible resource", Physical Review A **71**, 055801 (2005) (cit. on pp. 23, 25, 88).

[63] H. J. Carmichael, *Statistical Methods in Quantum Optics 1: Master Equations and Fokker-Planck Equations*, Theoretical and Mathematical Physics (Springer-Verlag, Berlin Heidelberg, 1999) (cit. on p. 26).

[64] O. Pinel, J. Fade, D. Braun, P. Jian, N. Treps, and C. Fabre, "Ultimate sensitivity of precision measurements with intense Gaussian quantum light: A multimodal approach", Physical Review A **85**, 010101 (2012) (cit. on pp. 27, 30, 62).

[65] O. Pinel, P. Jian, N. Treps, C. Fabre, and D. Braun, "Quantum parameter estimation using general single-mode Gaussian states", Physical Review A **88**, 040102 (2013) (cit. on p. 27).

[66] Z. Jiang, "Quantum Fisher information for states in exponential form", Physical Review A **89**, 032128 (2014) (cit. on p. 27).

[67] R. Nichols, P. Liuzzo-Scorpo, P. A. Knott, and G. Adesso, "Multiparameter Gaussian quantum metrology", Physical Review A **98** (2018) (cit. on p. 27).

[68] T. Matsubara, P. Facchi, V. Giovannetti, and K. Yuasa, "Optimal Gaussian metrology for generic multimode interferometric circuit", New Journal of Physics **21**, 033014 (2019) (cit. on pp. 27, 30).

[69] H. Scutaru, "Fidelity for displaced squeezed thermal states and the oscillator semigroup", Journal of Physics A: Mathematical and General **31**, 3659 (1998) (cit. on p. 27).

[70] P. Marian and T. A. Marian, "Uhlmann fidelity between two-mode Gaussian states", Physical Review A **86**, 022340 (2012) (cit. on p. 27).

[71] L. Banchi, S. L. Braunstein, and S. Pirandola, "Quantum fidelity for arbitrary Gaussian states", Physical Review Letters **115**, 260501 (2015) (cit. on p. 27).

[72] D. Šafránek, "Estimation of Gaussian quantum states", Journal of Physics A: Mathematical and Theoretical **52**, 035304 (2018) (cit. on p. 30).

[73] A. Monras and M. G. A. Paris, "Optimal Quantum Estimation of Loss in Bosonic Channels", Physical Review Letters **98**, 160401 (2007) (cit. on pp. 30, 33).

[74] U. Leonhardt and H. Paul, "Measuring the quantum state of light", Progress in Quantum Electronics **19**, 89–130 (1995) (cit. on pp. 30, 31, 96).

[75] U. Leonhardt, *Essential Quantum Optics* (Cambridge University Press, 2010) (cit. on pp. 30, 31).

[76] V. M. Schäfer, C. J. Ballance, K. Thirumalai, L. J. Stephenson, T. G. Ballance, A. M. Steane, and D. M. Lucas, "Fast quantum logic gates with trapped-ion qubits", Nature **555**, 75–78 (2018) (cit. on p. 32).

[77] T. Kovachy, P. Asenbaum, C. Overstreet, C. A. Donnelly, S. M. Dickerson, A. Sugarbaker, J. M. Hogan, and M. A. Kasevich, "Quantum superposition at the half-metre scale", Nature **528**, 530–533 (2015) (cit. on p. 32).

[78] S. Eibenberger, S. Gerlich, M. Arndt, M. Mayor, and J. Tüxen, "Matter–wave interference of particles selected from a molecular library with masses exceeding 10 000 amu", Physical Chemistry Chemical Physics **15**, 14696–14700 (2013) (cit. on p. 32).

[79] M. Toroš, G. Gasbarri, and A. Bassi, "Colored and dissipative continuous spontaneous localization model and bounds from matter-wave interferometry", Physics Letters A **381**, 3921–3927 (2017) (cit. on pp. 32, 50–52).

[80] F. Karolyhazy, "Gravitation and quantum mechanics of macroscopic objects", Il Nuovo Cimento A (1965-1970) **42**, 390–402 (1966) (cit. on p. 32).

[81] G. C. Ghirardi, A. Rimini, and T. Weber, "Unified dynamics for microscopic and macroscopic systems", Physical Review D **34**, 470–491 (1986) (cit. on pp. 32, 51, 52).

[82] P. Pearle, "Combining stochastic dynamical state-vector reduction with spontaneous localization", Physical Review A **39**, 2277–2289 (1989) (cit. on p. 32).

[83] G. C. Ghirardi, P. Pearle, and A. Rimini, "Markov processes in Hilbert space and continuous spontaneous localization of systems of identical particles", Physical Review A **42**, 78–89 (1990) (cit. on p. 32).

[84] L. Diósi, "A universal master equation for the gravitational violation of quantum mechanics", Physics Letters A **120**, 377–381 (1987) (cit. on p. 32).

[85] L. Diósi, "Models for universal reduction of macroscopic quantum fluctuations", Physical Review A **40**, 1165–1174 (1989) (cit. on p. 32).

[86] R. Penrose, "On Gravity's role in Quantum State Reduction", General Relativity and Gravitation **28**, 581–600 (1996) (cit. on p. 32).

[87] M. Bahrami, A. Smirne, and A. Bassi, "Role of gravity in the collapse of a wave function: A probe into the Diósi-Penrose model", Physical Review A **90**, 062105 (2014) (cit. on p. 32).

[88] A. Bassi, A. Großardt, and H. Ulbricht, "Gravitational decoherence", Classical and Quantum Gravity **34**, 193002 (2017) (cit. on p. 32).

[89] C. J. Riedel, "Direct detection of classically undetectable dark matter through quantum decoherence", Physical Review D **88**, 116005 (2013) (cit. on p. 32).

[90] J. Bateman, I. McHardy, A. Merle, T. R. Morris, and H. Ulbricht, "On the Existence of Low-Mass Dark Matter and its Direct Detection", Scientific Reports **5**, 8058 (2015) (cit. on p. 32).

[91] C. J. Riedel, "Decoherence from classically undetectable sources: Standard quantum limit for diffusion", Physical Review A **92**, 010101 (2015) (cit. on p. 32).

[92] C. J. Riedel and I. Yavin, "Decoherence as a way to measure extremely soft collisions with dark matter", Physical Review D **96**, 023007 (2017) (cit. on p. 32).

[93] A. Vinante, M. Bahrami, A. Bassi, O. Usenko, G. Wijts, and T. H. Oosterkamp, "Upper Bounds on Spontaneous Wave-Function Collapse Models Using Millikelvin-Cooled Nanocantilevers", Physical Review Letters **116**, 090402 (2016) (cit. on pp. 32, 50).

[94] A. Vinante, R. Mezzena, P. Falferi, M. Carlesso, and A. Bassi, "Improved Noninterferometric Test of Collapse Models Using Ultracold Cantilevers", Physical Review Letters **119**, 110401 (2017) (cit. on pp. 32, 50).

[95] M. Carlesso, A. Bassi, P. Falferi, and A. Vinante, "Experimental bounds on collapse models from gravitational wave detectors", Physical Review D **94**, 124036 (2016) (cit. on pp. 32, 50, 51).

[96] B. Helou, B. J. J. Slagmolen, D. E. McClelland, and Y. Chen, "LISA pathfinder appreciably constrains collapse models", Physical Review D **95**, 084054 (2017) (cit. on pp. 32, 50).

[97] M. Carlesso, M. Paternostro, H. Ulbricht, A. Vinante, and A. Bassi, "Non-interferometric test of the continuous spontaneous localization model based on rotational optomechanics", New Journal of Physics **20**, 083022 (2018) (cit. on pp. 32, 50, 51, 53).

[98] K. Piscicchia, A. Bassi, C. Curceanu, R. D. Grande, S. Donadi, B. C. Hiesmayr, and A. Pichler, "CSL Collapse Model Mapped with the Spontaneous Radiation", Entropy **19**, 319 (2017) (cit. on pp. 32, 50, 51).

[99] J. Li, S. Zippilli, J. Zhang, and D. Vitali, "Discriminating the effects of collapse models from environmental diffusion with levitated nanospheres", Physical Review A **93**, 050102 (2016) (cit. on pp. 32, 50).

[100] A. Tilloy and T. M. Stace, "Neutron Star Heating Constraints on Wave-Function Collapse Models", Physical Review Letters **123**, 080402 (2019) (cit. on pp. 32, 50).

[101] S. L. Adler, A. Bassi, M. Carlesso, and A. Vinante, "Testing continuous spontaneous localization with Fermi liquids", Physical Review D **99**, 103001 (2019) (cit. on pp. 32, 50).

[102] O. Romero-Isart, A. C. Pflanzer, F. Blaser, R. Kaltenbaek, N. Kiesel, M. Aspelmeyer, and J. I. Cirac, "Large Quantum Superpositions and Interference of Massive Nanometer-Sized Objects", Physical Review Letters **107**, 020405 (2011) (cit. on p. 32).

[103] O. Romero-Isart, "Quantum superposition of massive objects and collapse models", Physical Review A **84**, 052121 (2011) (cit. on p. 32).

[104] M. Scala, M. S. Kim, G. W. Morley, P. F. Barker, and S. Bose, "Matter-Wave Interferometry of a Levitated Thermal Nano-Oscillator Induced and Probed by a Spin", Physical Review Letters **111**, 180403 (2013) (cit. on pp. 32, 101).

[105] C. Wan, M. Scala, G. W. Morley, A. T. M. A. Rahman, H. Ulbricht, J. Bateman, P. F. Barker, S. Bose, and M. S. Kim, "Free Nano-Object Ramsey Interferometry for Large Quantum Superpositions", Physical Review Letters **117**, 143003 (2016) (cit. on pp. 32, 101).

[106] S. Bose, A. Mazumdar, G. W. Morley, H. Ulbricht, M. Toroš, M. Paternostro, A. A. Geraci, P. F. Barker, M. S. Kim, and G. Milburn, "Spin Entanglement Witness for Quantum Gravity", Physical Review Letters **119**, 240401 (2017) (cit. on p. 32).

[107] M. J. Weaver, D. Newsom, F. Luna, W. Löffler, and D. Bouwmeester, "Phonon interferometry for measuring quantum decoherence", Physical Review A **97**, 063832 (2018) (cit. on p. 32).

[108] R. Kaltenbaek, G. Hechenblaikner, N. Kiesel, O. Romero-Isart, K. C. Schwab, U. Johann, and M. Aspelmeyer, "Macroscopic quantum resonators (MAQRO)", Experimental Astronomy **34**, 123–164 (2012) (cit. on pp. 32, 34, 99).

[109] R. Kaltenbaek et al., "Macroscopic Quantum Resonators (MAQRO): 2015 update", EPJ Quantum Technology **3**, 5 (2016) (cit. on pp. 32, 34, 50, 53, 99, 101).

[110] European Space Agency, *CDF Study Report: QPPF - Assessment of a Quantum Physics Payload Platform*, CDF-183(C) (European Space Agency, July 2018) (cit. on pp. 32, 53, 99).

[111] M. G. Genoni, O. S. Duarte, and A. Serafini, "Unravelling the noise: the discrimination of wave function collapse models under time-continuous measurements", New Journal of Physics **18**, 103040 (2016) (cit. on pp. 32, 100).

[112] S. McMillen, M. Brunelli, M. Carlesso, A. Bassi, H. Ulbricht, M. G. A. Paris, and M. Paternostro, "Quantum-limited estimation of continuous spontaneous localization", Physical Review A **95**, 012132 (2017) (cit. on p. 32).

[113] G. Adesso, F. Dell'Anno, S. De Siena, F. Illuminati, and L. A. M. Souza, "Optimal estimation of losses at the ultimate quantum limit with non-Gaussian states", Physical Review A **79**, 040305 (2009) (cit. on p. 33).

[114] S. I. Knysh and G. A. Durkin, "Estimation of Phase and Diffusion: Combining Quantum Statistics and Classical Noise", (2013), arXiv:1307.0470 [physics, physics:quant-ph, stat] (cit. on pp. 33, 77).

[115] M. Tsang, "Quantum limit to subdiffraction incoherent optical imaging", Physical Review A **99**, 012305 (2019) (cit. on pp. 33, 77).

[116] S. Ng, S. Z. Ang, T. A. Wheatley, H. Yonezawa, A. Furusawa, E. H. Huntington, and M. Tsang, "Spectrum analysis with quantum dynamical systems", Physical Review A **93**, 042121 (2016) (cit. on pp. 33, 64).

[117] J. Millen, P. Z. G. Fonseca, T. Mavrogordatos, T. S. Monteiro, and P. F. Barker, "Cavity Cooling a Single Charged Levitated Nanosphere", Physical Review Letters **114** (2015) (cit. on p. 33).

[118] M. Rashid, T. Tufarelli, J. Bateman, J. Vovrosh, D. Hempston, M. S. Kim, and H. Ulbricht, "Experimental Realization of a Thermal Squeezed State of Levitated Optomechanics", Physical Review Letters **117**, 273601 (2016) (cit. on pp. 33, 50).

[119] D. Rugar and P. Grütter, "Mechanical parametric amplification and thermomechanical noise squeezing", Physical Review Letters **67**, 699–702 (1991) (cit. on pp. 33, 50).

[120] A. Pontin, M. Bonaldi, A. Borrielli, F. S. Cataliotti, F. Marino, G. A. Prodi, E. Serra, and F. Marin, "Squeezing a Thermal Mechanical Oscillator by Stabilized Parametric Effect on the Optical Spring", Physical Review Letters **112**, 023601 (2014) (cit. on pp. 33, 50).

[121] H. J. Kimble, Y. Levin, A. B. Matsko, K. S. Thorne, and S. P. Vyatchanin, "Conversion of conventional gravitational-wave interferometers into quantum nondemolition interferometers by modifying their input and/or output optics", Physical Review D **65**, 022002 (2001) (cit. on pp. 43, 54, 55, 57, 61, 64, 68, 77, 100).

[122] H. Miao, R. X. Adhikari, Y. Ma, B. Pang, and Y. Chen, "Towards the Fundamental Quantum Limit of Linear Measurements of Classical Signals", Physical Review Letters **119**, 050801 (2017) (cit. on pp. 43, 55).

[123] J. D. Cohen, S. M. Meenehan, G. S. MacCabe, S. Gröblacher, A. H. Safavi-Naeini, F. Marsili, M. D. Shaw, and O. Painter, "Phonon counting and intensity interferometry of a nanomechanical resonator", Nature **520**, 522–525 (2015) (cit. on p. 46).

[124] S. Hong, R. Riedinger, I. Marinković, A. Wallucks, S. G. Hofer, R. A. Norte, M. Aspelmeyer, and S. Gröblacher, "Hanbury Brown and Twiss interferometry of single phonons from an optomechanical resonator", Science **358**, 203–206 (2017) (cit. on p. 46).

[125] B. Collett and P. Pearle, "Wavefunction Collapse and Random Walk", Foundations of Physics **33**, 1495–1541 (2003) (cit. on p. 50).

[126] B. Schrinski, B. A. Stickler, and K. Hornberger, "Collapse-induced orientational localization of rigid rotors", Journal of the Optical Society of America B **34**, C1–C7 (2017) (cit. on pp. 51, 53).

[127] W. Feldmann and R. Tumulka, "Parameter diagrams of the GRW and CSL theories of wavefunction collapse", Journal of Physics A: Mathematical and Theoretical **45**, 065304 (2012) (cit. on p. 51).

[128] M. Carlesso, L. Ferialdi, and A. Bassi, "Colored collapse models from the non-interferometric perspective", The European Physical Journal D **72**, 159 (2018) (cit. on p. 51).

[129] D. Windey, C. Gonzalez-Ballestero, P. Maurer, L. Novotny, O. Romero-Isart, and R. Reimann, "Cavity-Based 3D Cooling of a Levitated Nanoparticle via Coherent Scattering", Physical Review Letters **122**, 123601 (2019) (cit. on p. 53).

[130] U. Delić, M. Reisenbauer, D. Grass, N. Kiesel, V. Vuletić, and M. Aspelmeyer, "Cavity Cooling of a Levitated Nanosphere by Coherent Scattering", Physical Review Letters **122** (2019) (cit. on p. 53).

[131] O. Romero-Isart, L. Clemente, C. Navau, A. Sanchez, and J. I. Cirac, "Quantum Magnetomechanics with Levitating Superconducting Microspheres", Physical Review Letters **109** (2012) (cit. on p. 53).

[132] C. Gonzalez-Ballestero, P. Maurer, D. Windey, L. Novotny, R. Reimann, and O. Romero-Isart, "Theory for cavity cooling of levitated nanoparticles via coherent scattering: Master equation approach", Physical Review A **100**, 013805 (2019) (cit. on p. 53).

[133] E. Hebestreit, M. Frimmer, R. Reimann, and L. Novotny, "Sensing Static Forces with Free-Falling Nanoparticles", Physical Review Letters **121**, 063602 (2018) (cit. on p. 53).

[134] B. R. Slezak and B. D'Urso, "A microsphere molecule: The interaction of two charged microspheres in a magneto-gravitational trap", Applied Physics Letters **114**, 244102 (2019) (cit. on p. 53).

[135] A. Lyons, G. C. Knee, E. Bolduc, T. Roger, J. Leach, E. M. Gauger, and D. Faccio, "Attosecond-resolution Hong-Ou-Mandel interferometry", Science Advances **4**, eaap9416 (2018) (cit. on p. 54).

[136] LIGO Scientific Collaboration and Virgo Collaboration, "Observation of Gravitational Waves from a Binary Black Hole Merger", Physical Review Letters **116**, 061102 (2016) (cit. on p. 54).

[137] F. Acernese et al., "Advanced Virgo: a second-generation interferometric gravitational wave detector", Classical and Quantum Gravity **32**, 024001 (2015) (cit. on p. 54).

[138] LIGO Scientific Collaboration and Virgo Collaboration, "GW170817: Observation of Gravitational Waves from a Binary Neutron Star Inspiral", Physical Review Letters **119**, 161101 (2017) (cit. on p. 54).

[139] LIGO Scientific Collaboration and Virgo Collaboration, Fermi Gamma-ray Burst Monitor, and INTEGRAL, "Gravitational Waves and Gamma-Rays from a Binary Neutron Star Merger: GW170817 and GRB 170817A", The Astrophysical Journal Letters **848**, L13 (2017) (cit. on p. 54).

[140] H. Miao, H. Yang, R. X. Adhikari, and Y. Chen, "Quantum limits of interferometer topologies for gravitational radiation detection", Classical and Quantum Gravity **31**, 165010 (2014) (cit. on pp. 54, 55, 57, 59, 64, 68).

[141] T. P. Purdy, R. W. Peterson, and C. A. Regal, "Observation of Radiation Pressure Shot Noise on a Macroscopic Object", Science **339**, 801–804 (2013) (cit. on p. 54).

[142] J. D. Teufel, F. Lecocq, and R. W. Simmonds, "Overwhelming Thermomechanical Motion with Microwave Radiation Pressure Shot Noise", Physical Review Letters **116**, 013602 (2016) (cit. on p. 54).

[143] J. Cripe, N. Aggarwal, R. Lanza, A. Libson, R. Singh, P. Heu, D. Follman, G. D. Cole, N. Mavalvala, and T. Corbitt, "Measurement of quantum back action in the audio band at room temperature", Nature (2019) (cit. on p. 54).

[144] R. Demkowicz-Dobrzański, K. Banaszek, and R. Schnabel, "Fundamental quantum interferometry bound for the squeezed-light-enhanced gravitational wave detector GEO 600", Physical Review A **88**, 041802 (2013) (cit. on pp. 54–56, 100).

[145] M. D. Lang and C. M. Caves, "Optimal Quantum-Enhanced Interferometry Using a Laser Power Source", Physical Review Letters **111**, 173601 (2013) (cit. on pp. 54, 79, 80, 101).

[146] LIGO Scientific Collaboration, "A gravitational wave observatory operating beyond the quantum shot-noise limit", Nature Physics **7**, 962–965 (2011) (cit. on pp. 54, 61).

[147] H. Grote, K. Danzmann, K. L. Dooley, R. Schnabel, J. Slutsky, and H. Vahlbruch, "First Long-Term Application of Squeezed States of Light in a Gravitational-Wave Observatory", Physical Review Letters **110**, 181101 (2013) (cit. on pp. 54, 61).

[148] LIGO Scientific Collaboration, "Enhanced sensitivity of the LIGO gravitational wave detector by using squeezed states of light", Nature Photonics **7**, 613–619 (2013) (cit. on pp. 54, 61).

[149] S. L. Danilishin and F. Y. Khalili, "Quantum Measurement Theory in Gravitational-Wave Detectors", Living Reviews in Relativity **15**, 5 (2012) (cit. on pp. 54–57, 59, 68).

[150] M. Tsang and C. M. Caves, "Coherent Quantum-Noise Cancellation for Optomechanical Sensors", Physical Review Letters **105**, 123601 (2010) (cit. on p. 54).

[151] C. F. Ockeloen-Korppi, E. Damskägg, J.-M. Pirkkalainen, A. A. Clerk, M. J. Woolley, and M. A. Sillanpää, "Quantum Backaction Evading Measurement of Collective Mechanical Modes", Physical Review Letters **117**, 140401 (2016) (cit. on p. 54).

[152] C. B. Møller, R. A. Thomas, G. Vasilakis, E. Zeuthen, Y. Tsaturyan, M. Balabas, K. Jensen, A. Schliesser, K. Hammerer, and E. S. Polzik, "Quantum back-action-evading measurement of motion in a negative mass reference frame", Nature **547**, 191–195 (2017) (cit. on p. 54).

[153] C. Wipf, T. Corbitt, Y. Chen, and N. Mavalvala, "Route to ponderomotive entanglement of light via optically trapped mirrors", New Journal of Physics **10**, 095017 (2008) (cit. on p. 55).

[154] K. Izumi, K. Arai, B. Barr, J. Betzwieser, A. Brooks, K. Dahl, S. Doravari, J. C. Driggers, W. Z. Korth, H. Miao, J. Rollins, S. Vass, D. Yeaton-Massey, and R. X. Adhikari, "Multicolor cavity metrology", Journal of the Optical Society of America A **29**, 2092–2103 (2012) (cit. on p. 55).

[155] A. Staley, D. Martynov, R. Abbott, R. X. Adhikari, K. Arai, S. Ballmer, L. Barsotti, A. F. Brooks, R. T. DeRosa, S. Dwyer, A. Effler, M. Evans, P. Fritschel, V. V. Frolov, C. Gray, C. J. Guido, R. Gustafson, M. Heintze, D. Hoak, K. Izumi, K. Kawabe, E. J. King, J. S. Kissel, K. Kokeyama, M. Landry, D. E. McClelland, J. Miller, A. Mullavey, B. O'Reilly, J. G. Rollins, J. R. Sanders, R. M. S. Schofield, D. Sigg, B. J. J. Slagmolen, N. D. Smith-Lefebvre, G. Vajente, R. L. Ward, and C. Wipf, "Achieving resonance in the Advanced LIGO gravitational-wave interferometer", Classical and Quantum Gravity **31**, 245010 (2014) (cit. on p. 55).

[156] H. Rehbein, H. Müller-Ebhardt, K. Somiya, C. Li, R. Schnabel, K. Danzmann, and Y. Chen, "Local readout enhancement for detuned signal-recycling interferometers", Physical Review D **76**, 062002 (2007) (cit. on p. 55).

[157] A. Buonanno and Y. Chen, "Quantum noise in second generation, signal-recycled laser interferometric gravitational-wave detectors", Physical Review D **64**, 042006 (2001) (cit. on pp. 55, 57, 59).

[158] A. Buonanno and Y. Chen, "Signal recycled laser-interferometer gravitational-wave detectors as optical springs", Physical Review D **65**, 042001 (2002) (cit. on pp. 55, 57, 59).

[159] A. Buonanno and Y. Chen, "Scaling law in signal recycled laser-interferometer gravitational-wave detectors", Physical Review D **67**, 062002 (2003) (cit. on pp. 55, 57, 59).

[160] H. Rehbein, H. Müller-Ebhardt, K. Somiya, S. L. Danilishin, R. Schnabel, K. Danzmann, and Y. Chen, "Double optical spring enhancement for gravitational-wave detectors", Physical Review D **78**, 062003 (2008) (cit. on pp. 55, 57).

[161] M. Korobko, N. Voronchev, H. Miao, and F. Y. Khalili, "Paired carriers as a way to reduce quantum noise of multicarrier gravitational-wave detectors", Physical Review D **91**, 042004 (2015) (cit. on pp. 55, 76).

[162] C. M. Caves and B. L. Schumaker, "New formalism for two-photon quantum optics. I. Quadrature phases and squeezed states", Physical Review A **31**, 3068–3092 (1985) (cit. on pp. 56, 57).

[163] B. L. Schumaker and C. M. Caves, "New formalism for two-photon quantum optics. II. Mathematical foundation and compact notation", Physical Review A **31**, 3093–3111 (1985) (cit. on pp. 56, 57).

[164] T. Corbitt, Y. Chen, and N. Mavalvala, "Mathematical framework for simulation of quantum fields in complex interferometers using the two-photon formalism", Physical Review A **72**, 013818 (2005) (cit. on p. 57).

[165] H. Miao and Y. Chen, "Quantum theory of laser interferometer gravitational wave detectors", in *Advanced Gravitational Wave Detectors*, edited by D. G. Blair, E. J. Howell, L. Ju, and C. Zhao (Cambridge University Press, 2012), pp. 277–297 (cit. on pp. 58, 61).

[166] P. Purdue and Y. Chen, "Practical speed meter designs for quantum nondemolition gravitational-wave interferometers", Physical Review D **66**, 122004 (2002) (cit. on p. 59).

[167] T. Corbitt, Y. Chen, F. Khalili, D. Ottaway, S. Vyatchanin, S. Whitcomb, and N. Mavalvala, "Squeezed-state source using radiation-pressure-induced rigidity", Physical Review A **73**, 023801 (2006) (cit. on p. 59).

[168] V. B. Braginsky and F. Y. Khalili, *Quantum Measurement*, edited by K. S. Thorne (Cambridge University Press, 1992) (cit. on p. 64).

[169] K. S. Thorne and R. D. Blandford, *Modern Classical Physics* (Princeton University Press, 2017), 1552 pp. (cit. on p. 64).

[170] S. Hild, H. Grote, J. Degallaix, S. Chelkowski, K. Danzmann, A. Freise, M. Hewitson, J. Hough, H. Lück, M. Prijatelj, K. A. Strain, J. R. Smith, and B. Willke, "DC-readout of a signal-recycled gravitational wave detector", Classical and Quantum Gravity **26**, 055012 (2009) (cit. on p. 68).

[171] T. T. Fricke, N. D. Smith-Lefebvre, R. Abbott, R. Adhikari, K. L. Dooley, Matthew Evans, P. Fritschel, V. V. Frolov, K. Kawabe, J. S. Kissel, B. J. J. Slagmolen, and S. J. Waldman, "DC readout experiment in Enhanced LIGO", Classical and Quantum Gravity **29**, 065005 (2012) (cit. on p. 68).

[172] D. W. C. Brooks, T. Botter, S. Schreppler, T. P. Purdy, N. Brahms, and D. M. Stamper-Kurn, "Non-classical light generated by quantum-noise-driven cavity optomechanics", Nature **488**, 476–480 (2012) (cit. on p. 76).

[173] A. H. Safavi-Naeini, S. Gröblacher, J. T. Hill, J. Chan, M. Aspelmeyer, and O. Painter, "Squeezed light from a silicon micromechanical resonator", Nature **500**, 185–189 (2013) (cit. on p. 76).

[174] T. P. Purdy, P.-L. Yu, R. W. Peterson, N. S. Kampel, and C. A. Regal, "Strong Optomechanical Squeezing of Light", Physical Review X **3**, 031012 (2013) (cit. on p. 76).

[175] R. Demkowicz-Dobrzański, J. Kołodyński, and M. Guţă, "The elusive Heisenberg limit in quantum-enhanced metrology", Nature Communications **3**, 1063 (2012) (cit. on pp. 76, 99, 100).

[176] M. D. Lang and C. M. Caves, "Optimal quantum-enhanced interferometry", Physical Review A **90**, 025802 (2014) (cit. on pp. 77–79, 83, 89, 98, 99, 101).

[177] M. Tsang, R. Nair, and X.-M. Lu, "Quantum Theory of Superresolution for Two Incoherent Optical Point Sources", Physical Review X **6**, 031033 (2016) (cit. on p. 77).

[178] C. Lupo and S. Pirandola, "Ultimate Precision Bound of Quantum and Subwavelength Imaging", Physical Review Letters **117**, 190802 (2016) (cit. on p. 77).

[179] Z. Yu and S. Prasad, "Quantum Limited Superresolution of an Incoherent Source Pair in Three Dimensions", Physical Review Letters **121**, 180504 (2018) (cit. on p. 77).

[180] S. Zhou and L. Jiang, "Modern description of Rayleigh's criterion", Physical Review A **99**, 013808 (2019) (cit. on p. 77).

[181] C. Napoli, S. Piano, R. Leach, G. Adesso, and T. Tufarelli, "Towards Superresolution Surface Metrology: Quantum Estimation of Angular and Axial Separations", Physical Review Letters **122**, 140505 (2019) (cit. on p. 77).

[182] T. Baumgratz and A. Datta, "Quantum Enhanced Estimation of a Multidimensional Field", Phys. Rev. Lett. **116**, 030801 (2016) (cit. on pp. 77, 78, 87, 94).

[183] P. J. D. Crowley, A. Datta, M. Barbieri, and I. A. Walmsley, "Tradeoff in simultaneous quantum-limited phase and loss estimation in interferometry", Physical Review A **89**, 023845 (2014) (cit. on p. 77).

[184] Y. Yao, L. Ge, X. Xiao, X.-g. Wang, and C.-p. Sun, "Multiple phase estimation in quantum cloning machines", Physical Review A **90**, 022327 (2014) (cit. on p. 77).

[185] J.-D. Yue, Y.-R. Zhang, and H. Fan, "Quantum-enhanced metrology for multiple phase estimation with noise", Scientific Reports **4** (2014) (cit. on p. 77).

[186] Y. Yao, L. Ge, X. Xiao, X. Wang, and C. P. Sun, "Multiple phase estimation for arbitrary pure states under white noise", Physical Review A **90**, 062113 (2014) (cit. on p. 77).

[187] P. A. Knott, T. J. Proctor, A. J. Hayes, J. F. Ralph, P. Kok, and J. A. Dunningham, "Local versus global strategies in multiparameter estimation", Physical Review A **94**, 062312 (2016) (cit. on p. 77).

[188] L. Zhang and K. W. C. Chan, "Quantum multiparameter estimation with generalized balanced multimode NOON-like states", Physical Review A **95**, 032321 (2017) (cit. on pp. 77, 85).

[189] L. Zhang and K. W. C. Chan, "Scalable Generation of Multi-mode NOON States for Quantum Multiple-phase Estimation", Scientific Reports **8**, 11440 (2018) (cit. on pp. 78, 86).

[190] M. J. Holland and K. Burnett, "Interferometric detection of optical phase shifts at the Heisenberg limit", Physical Review Letters **71**, 1355–1358 (1993) (cit. on p. 78).

[191] C. You, S. Adhikari, Y. Chi, M. L. LaBorde, C. T. Matyas, C. Zhang, Z. Su, T. Byrnes, C. Lu, J. P. Dowling, and J. P. Olson, "Multiparameter estimation with single photons—linearly-optically generated quantum entanglement beats the shotnoise limit", Journal of Optics **19**, 124002 (2017) (cit. on pp. 78, 97, 98).

[192] B. Yurke, S. L. McCall, and J. R. Klauder, "SU(2) and SU(1,1) interferometers", Physical Review A **33**, 4033–4054 (1986) (cit. on p. 79).

[193] M. Jarzyna and R. Demkowicz-Dobrzański, "Quantum interferometry with and without an external phase reference", Physical Review A **85**, 011801 (2012) (cit. on pp. 79, 82–84, 100).

[194] J. Sahota, N. Quesada, and D. F. V. James, "Physical resources for optical phase estimation", Physical Review A **94**, 033817 (2016) (cit. on p. 79).

[195] H. F. Hofmann, "All path-symmetric pure states achieve their maximal phase sensitivity in conventional two-path interferometry", Physical Review A **79**, 033822 (2009) (cit. on p. 80).

[196] A. De Pasquale, P. Facchi, G. Florio, V. Giovannetti, K. Matsuoka, and K. Yuasa, "Two-Mode Bosonic Quantum Metrology with Number Fluctuations", Physical Review A **92**, 042115 (2015) (cit. on p. 82).

[197] M. Takeoka, K. P. Seshadreesan, C. You, S. Izumi, and J. P. Dowling, "Fundamental precision limit of a Mach-Zehnder interferometric sensor when one of the inputs is the vacuum", Physical Review A **96**, 052118 (2017) (cit. on pp. 82, 100).

[198] J. Suzuki, "Parameter estimation of qubit states with unknown phase parameter", International Journal of Quantum Information **13**, 1450044 (2015) (cit. on pp. 82, 100).

[199] Y. Yang, G. Chiribella, and M. Hayashi, "Attaining the Ultimate Precision Limit in Quantum State Estimation", Communications in Mathematical Physics **368**, 223–293 (2019) (cit. on pp. 82, 100).

[200] C. Sparaciari, S. Olivares, and M. G. A. Paris, "Bounds to precision for quantum interferometry with Gaussian states and operations", Journal of the Optical Society of America B **32**, 1354 (2015) (cit. on p. 83).

[201] A. Monras, "Optimal phase measurements with pure Gaussian states", Physical Review A **73**, 033821 (2006) (cit. on pp. 84, 94, 99).

[202] K. F. Riley, M. P. Hobson, and S. J. Bence, *Mathematical Methods for Physics and Engineering*, 3rd ed. (Cambridge University Press, Cambridge, 2006) (cit. on p. 90).

[203] C. S. Hamilton, R. Kruse, L. Sansoni, S. Barkhofen, C. Silberhorn, and I. Jex, "Gaussian Boson Sampling", Physical Review Letters **119**, 170501 (2017) (cit. on p. 97).

[204] R. Kruse, C. S. Hamilton, L. Sansoni, S. Barkhofen, C. Silberhorn, and I. Jex, "Detailed study of Gaussian boson sampling", Physical Review A **100**, 032326 (2019) (cit. on p. 97).

[205] G. Cariolaro and G. Pierobon, "Fock expansion of multimode pure Gaussian states", Journal of Mathematical Physics **56**, 122109 (2015) (cit. on p. 97).

[206] S. D. Bartlett, B. C. Sanders, S. L. Braunstein, and K. Nemoto, "Efficient Classical Simulation of Continuous Variable Quantum Information Processes", Physical Review Letters **88**, 097904 (2002) (cit. on pp. 98, 101).

[207] A. Furusawa and P. van Loock, *Quantum Teleportation and Entanglement: A Hybrid Approach to Optical Quantum Information Processing* (John Wiley & Sons, Ltd, Apr. 4, 2011) (cit. on pp. 98, 101).

[208] J. Eisert, S. Scheel, and M. B. Plenio, "Distilling Gaussian States with Gaussian Operations is Impossible", Physical Review Letters **89**, 137903 (2002) (cit. on p. 98).

[209] J. Fiurášek, "Gaussian Transformations and Distillation of Entangled Gaussian States", Physical Review Letters **89**, 137904 (2002) (cit. on p. 98).

[210] G. Giedke and J. Ignacio Cirac, "Characterization of Gaussian operations and distillation of Gaussian states", Physical Review A **66**, 032316 (2002) (cit. on p. 98).

[211] L. Lami, B. Regula, X. Wang, R. Nichols, A. Winter, and G. Adesso, "Gaussian quantum resource theories", Physical Review A **98**, 022335 (2018) (cit. on p. 98).

[212] S. M. Barnett, G. Ferenczi, C. R. Gilson, and F. C. Speirits, "Statistics of photon-subtracted and photon-added states", Physical Review A **98**, 013809 (2018) (cit. on pp. 98, 101).

[213] P. A. Knott, "A search algorithm for quantum state engineering and metrology", New Journal of Physics **18**, 073033 (2016) (cit. on p. 98).

[214] B. M. Escher, R. L. de Matos Filho, and L. Davidovich, "General framework for estimating the ultimate precision limit in noisy quantum-enhanced metrology", Nature Physics **7**, 406–411 (2011) (cit. on pp. 99, 100).

[215] R. Demkowicz-Dobrzański, J. Czajkowski, and P. Sekatski, "Adaptive Quantum Metrology under General Markovian Noise", Physical Review X **7**, 041009 (2017) (cit. on p. 100).

[216] R. Demkowicz-Dobrzański, U. Dorner, B. J. Smith, J. S. Lundeen, W. Wasilewski, K. Banaszek, and I. A. Walmsley, "Quantum phase estimation with lossy interferometers", Physical Review A **80**, 013825 (2009) (cit. on p. 100).

[217] J. Řehaček, Z. Hradil, B. Stoklasa, M. Paúr, J. Grover, A. Krzic, and L. L. Sánchez-Soto, "Multiparameter quantum metrology of incoherent point sources: Towards realistic superresolution", Physical Review A **96**, 062107 (2017) (cit. on p. 100).

[218] S. L. Braunstein, "How large a sample is needed for the maximum likelihood estimator to be approximately Gaussian?", Journal of Physics A: Mathematical and General **25**, 3813 (1992) (cit. on p. 100).

[219] Á. Rivas and A. Luis, "Sub-Heisenberg estimation of non-random phase shifts", New Journal of Physics **14**, 093052 (2012) (cit. on p. 100).

[220] M. Tsang, "Ziv-Zakai Error Bounds for Quantum Parameter Estimation", Physical Review Letters **108**, 230401 (2012) (cit. on p. 100).

[221] V. Giovannetti and L. Maccone, "Sub-Heisenberg Estimation Strategies Are Ineffective", Physical Review Letters **108**, 210404 (2012) (cit. on p. 100).

[222] M. Jarzyna and R. Demkowicz-Dobrzański, "True precision limits in quantum metrology", New Journal of Physics **17**, 013010 (2015) (cit. on p. 100).

[223] J. Rubio and J. Dunningham, "Quantum metrology in the presence of limited data", New Journal of Physics **21**, 043037 (2019) (cit. on p. 100).

[224] X.-M. Lu and M. Tsang, "Quantum Weiss-Weinstein bounds for quantum metrology", Quantum Science and Technology **1**, 015002 (2016) (cit. on p. 100).

[225] J. Rubio, P. Knott, and J. Dunningham, "Non-asymptotic analysis of quantum metrology protocols beyond the Cramér–Rao bound", Journal of Physics Communications **2**, 015027 (2018) (cit. on p. 100).

[226] M. A. Taylor, J. Janousek, V. Daria, J. Knittel, B. Hage, H.-A. Bachor, and W. P. Bowen, "Biological measurement beyond the quantum limit", Nature Photonics **7**, 229–233 (2013) (cit. on p. 100).

[227] J. Bateman, S. Nimmrichter, K. Hornberger, and H. Ulbricht, "Near-field interferometry of a free-falling nanoparticle from a point-like source", Nature Communications **5**, 4788 (2014) (cit. on p. 101).